3-1-2018

Excited Argon 1s5 Production in Microhollow Cathode Discharges

Richard D. Peterson

Excited Argon $1s_5$ Production in Microhollow Cathode Discharges

THESIS

Richard D. Peterson, 2d Lt, USAF

AFIT-ENP-MS-18-M-095

DEPARTMENT OF THE AIR FORCE
AIR UNIVERSITY

AIR FORCE INSTITUTE OF TECHNOLOGY

Wright-Patterson Air Force Base, Ohio

AFIT-ENP-MS-18-M-095

EXCITED ARGON $1s_5$ PRODUCTION IN MICROHOLLOW CATHODE DISCHARGES

THESIS

Presented to the Faculty

Department of Engineering Physics

Graduate School of Engineering and Management

Air Force Institute of Technology

Air University

Air Education and Training Command

in Partial Fulfillment of the Requirements for the

Degree of Master of Science in Applied Physics

Richard D. Peterson, B.S. Physics

2d Lt, USAF

February 20, 2018

AFIT-ENP-MS-18-M-095

EXCITED ARGON $1s_5$ PRODUCTION IN MICROHOLLOW CATHODE DISCHARGES

THESIS

Richard D. Peterson, B.S. Physics
2d Lt, USAF

Committee Membership:

Dr. Glen P. Perram
Chair

Dr. Christopher A. Rice
Member

Dr. David E. Weeks
Member

Abstract

Diode-pumped rare gas lasers (DPRGL) have been in development for their potential to become high energy lasers with excellent beam quality that is typical of gas lasers. DPRGL require metastable densities on the order of 10^{13} cm^{-3} at pressures around one atmosphere for efficient operation. Argon $1s_5$ number densities have been measured in microhollow cathode discharges (MHCD) using tunable diode laser absorption spectroscopy. The MHCD had copper electrodes with gaps of 127 and 254 μm and hole diameters from 100-400 μm. Absorbance was measured at pressures of 37 Torr up to 400 Torr, where absorbance could no longer be detected. Fluorescence images were taken both perpendicular to the plate and viewing the hole end on to observe plasma uniformity and determine the absorbance path length. The images revealed the plasma formation was inconsistent and often not in line with the hole, making path length determinations difficult. Assuming a path length equal to the total plate thickness of either 198 or 325 μm resulted in the maximum possible Ar $1s_5$ number densities, ranging from 5.5×10^{12} to 4.0×10^{13} cm^{-3}. The actual number densities could be three times lower depending on the actual path length. There were no consistent trends with hole diameter, pressure, or gap distance.

Relative 2p state populations were measured by optical emission spectroscopy and used in a five-level laser model to estimate the electron density, electron temperature and the predicted gain. The relative populations indicate that the plasma was not in local thermodynamic equilibrium. The average electron density and temperature predicted by the model was 1.7×10^{14} cm^{-3} and 1.2 eV respectively. Despite number densities typically used in DPRGL the model predicted that gain would not be achieved due to the high laser threshold that is a result of the short gain length.

Acknowledgements

I would like to thank Dr. Glen Perram for continual guidance throughout the past year. Early on he patiently answered my often repeated questions to ensure I had the foundational knowledge to build upon. His insight and direction have helped me in this work and prepared me for future endeavors.

I would also like to thank Dr. Christopher Rice for his assistance in ensuring I had the lab equipment needed and that it was functioning correctly. He also often gave me words of encouragement as he passed by my desk that I greatly appreciated.

Finally, I would like to thank Dr. Ben Eshel for his constant support and mentor ship. Being able to pull from his knowledge and experience on the topic has been vital to me understanding of the work. He taught me how to run the lab equipment and answered countless questions to help me understand the theory behind the experiments.

Richard D. Peterson

Table of Contents

Page

List of Figures

List of Tables

EXCITED ARGON $1s_5$ PRODUCTION IN
MICROHOLLOW CATHODE DISCHARGES

I. Introduction

The Department of Defense (DoD) has been interested in the use of high energy laser weapons for many decades. In the past 15 years diode-pumped alkali vapor lasers (DPAL) have been developed and are capable of single-aperture, high-power operation with excellent beam quality [23, 31, 30]. However, the alkali vapors are chemically aggressive, causing damage to the cell windows, and producing hydrides ("laser snow") due to reactions with hydrocarbons which are sometimes used as the spin orbit relaxation agent for atmospheric pressure operation. Due to these challenges there has been work to develop comparable lasers using other elements, such as rare gas atoms (Rg), as the gain medium. The Rg atoms are first excited out of the closed-shell ground-state, predominantly into the first metastable $1s_5$ state, by electron impact. This excitation is commonly done using direct-current (DC), radio-frequency (RF) or microwave excitation. The laser energy is provided by the use of volume-bragg-grating narrowed diodes. The rare gases have lasing schemes analogous to DPAL systems with the benefit that they are chemically inert. A trade-off arises from the required large-volume, atmospheric pressure operational conditions for the Rg laser, which are difficult to achieve. The $1s_5$ state has the longest theoretical lifetime (~60 s) [28] of the first excited states of argon and has been used as the lower lasing state in laser demonstrations. The measured lifetime in plasma operation is in the microsecond regime [18] due to quenching, and radiation trapping of the $1s_4$ sate increases its lifetime to be comparable to the $1s_5$ [28]. The most common argon

lasing scheme consists of optical pumping from $1s_5 \rightarrow 2p_9$, at 811.7542 nm, followed by collisional relaxation to $2p_{10}$, a transition of 1360.7 cm^{-1}, and then lasing back to $1s_5$, at 912.5741 nm. The first demonstration of an optically pumped rare gas laser (OPRGL) was in 2012 by Han and Heaven [16]. Argon (Ar), krypton (Kr) and xenon (Xe) were used as the working gas, with helium or argon as the collisional partner. Pulsed lasing was observed from all gas mixtures using an 18 kV pulsed discharge [16]. Continuous wave (cw) lasing was later achieved by Rawlins et al. in 2014 using a microwave resonator strip array to create the plasma [34]. Images showed the beam profile as Gaussian, indicating excellent beam quality in the TEM_{00} mode, as expected of gas laser systems [33]. The highest Rg laser output achieved so far was 4.1 W in 2017 [14]. The lasing demonstrations show potential for OPRGL to become high energy lasers with excellent beam quality. To achieve this potential it is vital to have a discharge that produces a high concentration ($\sim 10^{13}$ cm^{-3}) of metastable rare gas atoms (Rg*) at near atmospheric pressure, with the ability to scale to large volumes (> 10 cm^3). Various discharge types have been tested [16, 15, 33, 9, 25, 19], but a suitable discharge design has not yet been developed.

Recently it was proposed to use a microcathode structured discharge array (MCSDA) [7]. The MCSDA consists of a microhollow cathode discharge array (MHCDA) and another anode separated by 1 cm or less. The plasma generated by the MHCDA becomes an electron source in the MCSDA. The electrons are then accelerated toward the additional anode creating a larger volume plasma. Studies of a single MHCD with and without the extra anode have been done and show stable operation at high pressures [28, 36, 35]. Using tunable diode laser absorption spectroscopy (TDLAS) Penache et al. reported Ar $1s_5$ number densities as high as 6.3×10^{14} cm^{-3} using a single 300 μm hole in a MHCD composed of 130 μm thick copper electrodes separated by 50 μm thick Kapton.

In the present work multiple MHCD are tested with different dielectric material thicknesses and hole sizes to determine if the high number densities can be replicated, and to determine the most advantageous discharge specifications. The details of the plate specifications will be presented as well as the method in determining number densities. Experimental results will also be applied to a five-level laser model to predict the electron density, electron temperature, and the gain.

II. Backrground

2.1 Energy Level Notation

Notations for the energy levels of rare gases are often given in either Racah or Paschen because neither L-S (Russell-Saunders) or j-j coupling sufficiently describe the energy levels of the excited Rg states. Racah notation has the form $nl(^{2S+1}L_j)[K]_J$, where n and l are the principal and orbital quantum numbers of the exited atom. S, L, and j are the total spin, total orbital and total angular momentum quantum numbers of the core. $K = j + l$ and $J = K + s_e$, where s_e is the spin of the excited electron ($\pm 1/2$) [7]. Racah notation is sometimes abbreviated by removing the term in parenthesis, which is the Russell-Saunders coupling term. The benefit of Racah notation is that it provides actual information about the state of the atom. However, it is not convenient to write or talk about energy levels in this way so Paschen notation is often used. Paschen notation has a much simpler form of $n'l_i$, where l is the orbital quantum number of the excited electron, and $n' = n - n_c + l$, where n is the principal quantum number of the excited electron and n_c is the principal quantum number of the core atom (e.g., $n_c = 3$ for Ar). The subscript i just numbers the levels of the same $n'l$ from highest energy (i.e., lowest number) to lowest energy (i.e., highest number). The exception to this is the 1s manifold where $1s_2$ is the highest energy state and $1s_1$ is used to denote the ground state. Figure 1 shows both Paschen and Racah notation for the 1s and 2p manifolds. The Paschen notation is abbreviated to just the l_i term.

2.2 Lasing Scheme

The rare gas atoms cannot be optically pumped from the ground state to a metastable state due to angular momentum selection rules, so they must first be

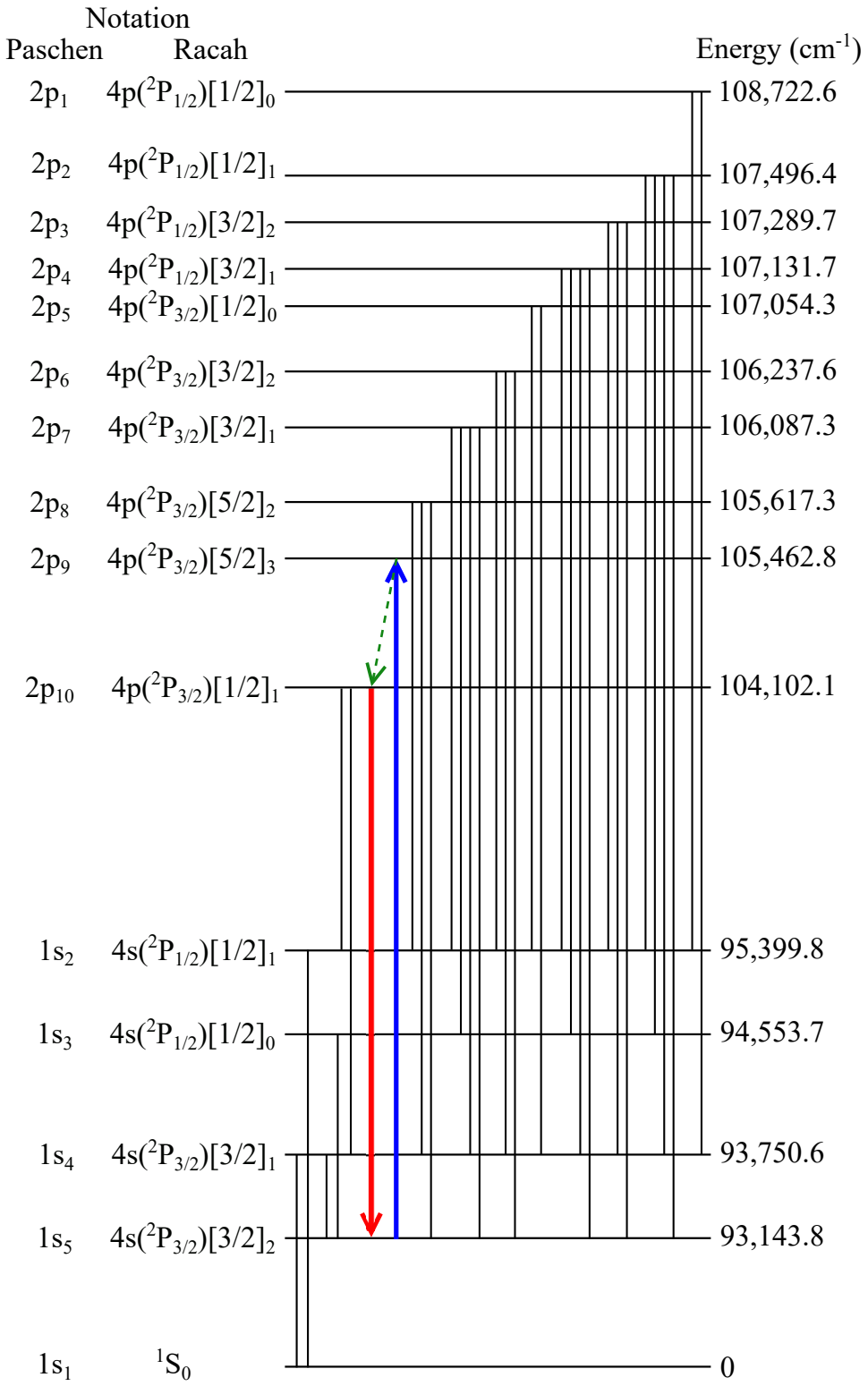

Figure 1. Grotrian diagram for the argon 1s and 2p manifolds. The solid lines between states represent optically allowed transitions. The lasing scheme is shown with pumping (blue) from $1s_5 \rightarrow 2p_9$ (811.7542 nm), collisional transfer (dashed green) from $2p_9 \rightarrow 2p_{10}$ (1360.7 cm^{-1}), and lasing (red) from $2p_{10} \rightarrow 1s_5$ (912.5471 nm). Adapted from [7].

excited by an electric discharge to one of the four 1s states. Experimental results [28] have shown that the $1s_5$ state has a higher population than the other 1s states and as a result it has been used in lasing demonstrations. Once in an excited state the general lasing scheme is a three level scheme shown in Figure 1 for argon. The metastable rare gas atoms (Rg*) are pumped from the $1s_5$ to $2p_9$ energy level. Collisions with another rare gas (typically helium) relax the atoms to the $2p_{10}$ level, from which it lases back down to $1s_5$.

2.3 Plasmas

The plasmas used in rare gas lasers are generated by applying an electrical potential to the rare gas. There is a small amount of ionization occurring in the gas which supplies a few electrons. When a sufficiently high potential is applied to the gas, the electrons are accelerated and collide with other atoms causing further ionization. The applied electric field continues to accelerate the electrons and ions creating a cascading effect leading to the formation of a plasma. Electron and atomic collisions are two of the processes involved in the kinetics of the plasma. Other process include Penning ionization, recombination, dissociation, radiative transition, radiation trapping and quenching [43, 37].

Plasmas can be considered 'hot' (in local thermodynamic equilibrium) or 'cold' (non-local thermodynamic equilibrium). A local thermodynamic equilibrium (LTE) plasma is one in which the electrons, ions, and neutral particles are all in thermodynamic equilibrium. They are described by a single temperature which can be anywhere from a few thousand Kelvin to over a million Kelvin [10]. Although all particles are described by a single temperature, the temperature can slowly evolve in both time and space. A non-LTE plasma has an electron temperature that is much higher than the ion or neutral particle temperature. The electron temperature typically ranges

from 10,000 K to over 100,000 K while the ion and neutral gas temperature is usually around 300 K to 2500 K [3, 10]. It is important to note that the electron energy distribution of a non-LTE plasma is generally non-Maxwellian. Although the idea of a thermodynamic temperature requires a Maxwell-Boltzmann distribution, electron temperature is still used in the non-LTE plasma case. LTE and non-LTE plasmas are typically generated at high and low gas pressures respectively [2]. A higher gas pressure for a given temperature means a higher gas density, which results in more frequent collisions. A high collision frequency means that particles are more likely to reach equilibrium. Electron densities are typically higher in LTE plasmas ($10^{15} - 10^{20}$ cm^{-3}) than in non-LTE plasmas ($< 10^{13}$ cm^{-3}) [39].

The type of plasma desired for rare gas laser operation is a glow discharge, which is a non-LTE plasma [39]. The challenge is being able to generate a stable non-LTE plasma at high pressures and large volumes [10]. A common property discussed with gas discharges the correlation of the breakdown voltage, V_B, and the product of the gas pressure, p, and electrode separation distance, d. The breakdown voltage is the voltage required to initially ignite the plasma. The relationship between V_B and pd is given by a Paschen curve, which in typical macroscopic gas discharges has the functional form of

$$V_B = \frac{B(pd)}{\ln(Apd) - \ln(\ln(1/\gamma_{se} + 1))}. \tag{1}$$

The constants A and B are dependent on the gas and γ_{se} is the secondary emission coefficient, which is dependent on the electrode and dielectric material, as well as the gas [1, 32]. Figure 2 shows a Paschen curve for argon using parameters $A = 12$ cm^{-1} Torr^{-1}, $B = 180$ V/(cm Torr), and $\gamma_{se} = 7 \times 10^{-3}$ from the literature [1, 32]. For a fixed electrode separation there is an optimal pressure that produces a minimum breakdown voltage. At lower pressures the density of the gas is so low that there are not enough atoms for free electrons to collide with. At higher pressures the density

of atoms increase resulting in a corresponding increase of the collision frequency. In this case the electrons are not able to gain enough energy between collisions to ionize the gas, unless a stronger electric field is applied. The typical operating range of pd values is around 1-10 Torr cm [11]. To operate near atmospheric pressure the distance between electrodes would need to be around 100 μm in order to achieve lower breakdown voltages. All of this assumes the Paschen curve is still applicable in micro-discharges (small separation distances), which may not be true.

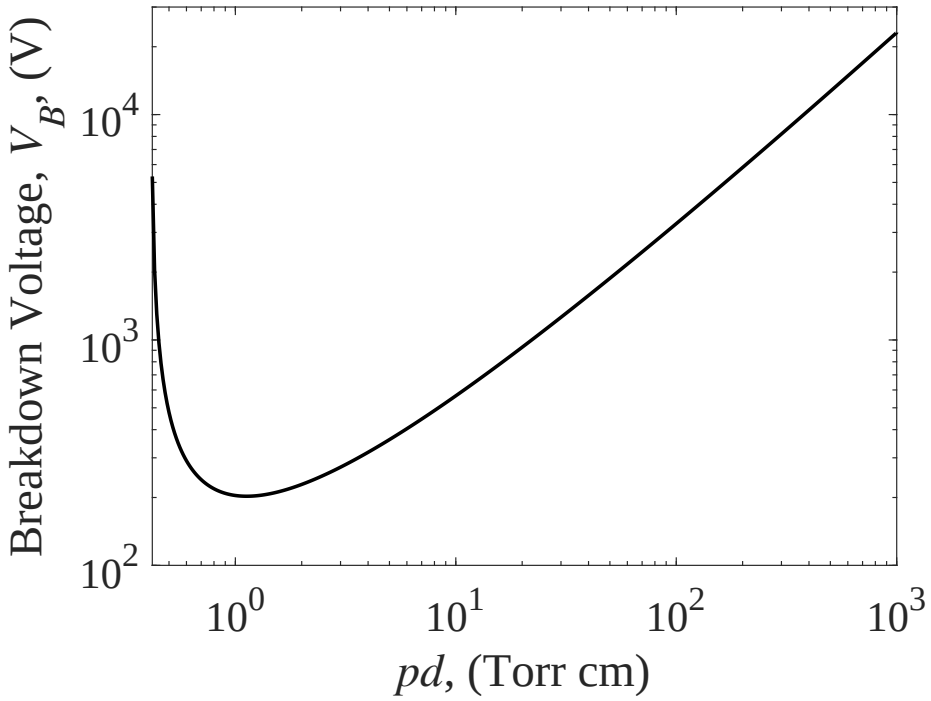

Figure 2. A typical Paschen curve depicting relationship between the plasma breakdown voltage and the product of the gas pressure and electrode separation distance, *pd*. The exact shape is dependent on the gas type and discharge materials. The curve shown uses gas constants for argon and the secondary emission coefficient for copper found in the literature [32, 1].

2.4 Previous Work

The first demonstration of optically pumped rare gas lasers (OPRGL) used the discharge cavity of a commercial excimer laser [16]. It was a pulsed discharge operated

at 18 kV. A schematic of the discharge cavity is shown in Figure 3(a). The discharge cavity was 80 cm long and the electrodes were 2.5 cm apart. Static gas mixtures were made by placing approximately 30 mbar (22.5 Torr) of either Ar, Kr, or Xe in the cavity and then filling it with He to total pressures of 200-2000 mbar (150-1500 Torr). Assuming that the temperature of the gas was around 300 K the reduced electric field was approximately 150 Td at 150 Torr and 15 Td at 1500 Torr. The metastable states were populated by 10 ns discharge pulses at a frequency of 10 Hz. The metastable argon (Ar*) number density was reported to be greater than 4×10^{13} cm^{-3} [16]. A tunable optical parametric oscillator was used to pump the $1s_5 \rightarrow 2p_9$ transition with 10 ns pulses and energies around 0.25 mJ. Pulsed lasing was observed for all mixtures, including a pure argon mixture, on the $2p_{10} \rightarrow 1s_5$ transition.

The first DPRGL demonstration was in 2013, when a continuous wave (cw) diode laser was used as the pump for lasing demonstrations [15]. A pulsed discharge was used consisting of 2.5 × 2.5 cm parallel stainless steel electrodes separated by 0.5 cm. The electrodes were contained in a cylindrical glass cell with a diameter of 5 cm and a length of 15 cm, shown schematically in Figure 3(b). The gas flowed through the cell and the plasma was stable at pressures up to 130 mbar (97.5 Torr) for pure Ar and 460 mbar (345 Torr) for Ar/He mixtures with freshly cleaned electrodes. The discharge pulses were 1 μs long at a frequency of 1 kHz. With -1,000 V to -2,000 V pulses the reduced electric field in the discharge at 150 Torr was 41 to 83 Td respectively. At the highest operated pressure (345 Torr) the reduced electric field was 18 Td to 36 Td. Pulsed lasing was observed for pure Ar at 68 Torr and Ar/He mixtures at total pressures of 296 Torr and 345 Torr.

A cw rare gas laser was first observed in 2014 [33]. The gas consisted of 2% Ar in He at a total pressure of 1 atm (760 Torr). In these experiments the argon metastable state ($1s_5$) was populated using a linear microwave powered micro-discharge array,

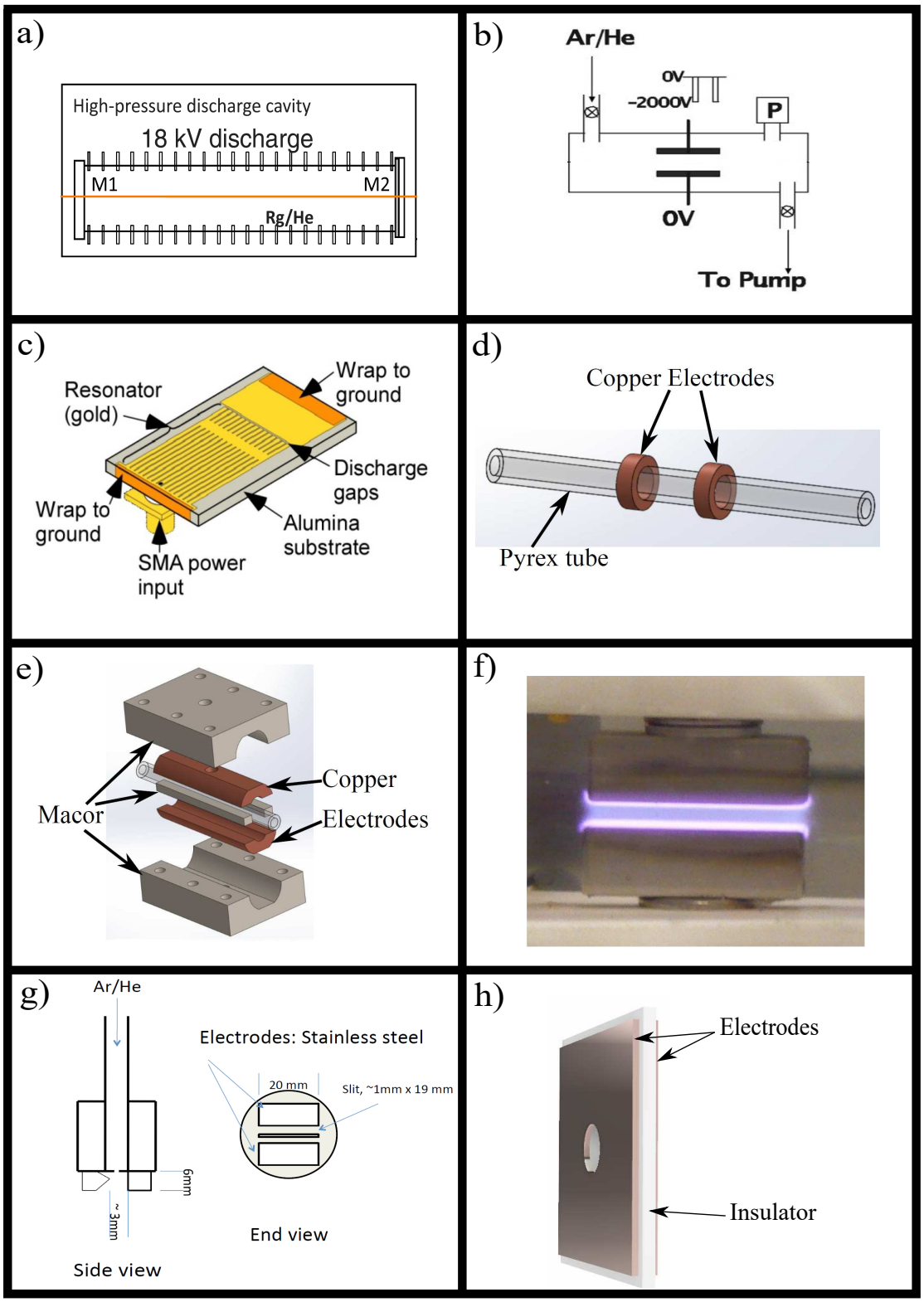

Figure 3. Dishcarges that have been used in the development of DPRGL: a) a 10 Hz pulsed discharge [16], b) a 1 kHz pulsed discharge [15], c) microwave resonator [34], d) RF longitudinal DBD [7], e) RF transverse DBD [7], f) 20 kHz pulsed DBD [25], g) 200 kHz pulsed discharge[19], h) a MHCD.

shown in Fig. 3(c). The array used 15 gold resonator strips each 1 mm wide and separated by 0.25 mm on an alumina substrate board. A net power of 9 W produced a microplasma in a 25 μm gap between the ends of the resonator strips and a ground plate. The gas flow was along the length of the resonator strips toward the ground plate at a flow rate of 3.7 mmole/s. The spatial extent of the plasma was 300 μm vertically above the surface, 900 μm across the gap and 19 mm across all the resonators. The reduced electric field cannot be calculated because neither the potential nor current were measured. The Ar* concentration produced by the discharge was approximately 3×10^{12} cm^{-3}. Lasing experiments were preformed and the output power measured at 912 nm was 22 mW for an absorbed pump power of ~44 mW. This corresponds to an optical-to-optical efficiency of ~55%. The gain for just a single pass through the cavity was 1.1 cm^{-1}. The output beam was imaged and was observed to be Gaussian without any signs of distortion from the flow field or microplasma [34].

Studies have also been done using two similar radio frequency (RF) dielectric barrier discharges (DBD) [9, 7]. One is referred to as longitudinal and the other transverse due to the respective successive ring and clamshell type geometries. Both consisted of a 0.635 cm outer diameter, 0.381 cm inner diameter, alumina or pyrex tube with copper electrodes outside of the tube. The longitudinal configuration used two ring shaped electrodes around the tube spaced 1.27 cm apart, as shown in Figure 3(d). The clamshell configuration consisted of 6.35 cm long electrodes cut by electrical discharge machining to fit around tube. As shown in Figure 3(e), Macor was used to clamp the electrodes to the tube and fill the gap between the electrodes to prevent shorting. The RF power was constant at 10 W and 13.56 MHz. At 150 Torr the reduced electric field was 8 Td for the ring DBD and 27 Td for the clamshell DBD. The gas consisted of pure Ar and 2.5% - 25% Ar in He at pressures of 1.3-50

Torr and 10-200 Torr and flow rates of 72-1,000 sccm and 25-50 sccm, respectively. At 5% Ar in He the peak $1s_5$ concentration was approximately 1.3×10^{12} cm^{-3} at 10 Torr. The concentration steadily decreased to approximately 0.6×10^{12} cm^{-3} at a pressure of 160 Torr. Lasing was not possible due to the low metastable concentration. Pressure broadening and shift rates for various transition were measured, which will aid in matching the pump line width to the atomic line width for laser operation.

Another discharge studied for OPRGL was a 20 kHz pulsed DBD [25]. It consisted of 18 mm long, 6.35 mm wide anodized aluminum electrodes mounted in a glass cell. Figure 3(f) shows the plasma formed in the 2-3 mm gap between the electrodes. The gas was 2-5% Ar in He at total pressures between 200-700 Torr, flowing at 1,500-2,000 sccm. The voltage was kept below 300 V and the current below 50 mA. The reduced electric field at 150 Torr would be 31 Td and 21 Td for the 2 mm and 3 mm gap respectively. The number density of the Ar($1s_5$) state was measured using tunable diode laser absorption spectroscopy. It was around 0.5×10^{12} cm^{-3} for the 3 mm gap and mostly constant with pressure. The number density for the 2 mm gap increased with pressure to around 1.5×10^{12} cm^{-3}. In a 10% Ar/He mixture and 2200 sccm flow rate the number density increased from around 0.5×10^{12} cm^{-3} at 250 Torr to around 1.0×10^{12} cm^{-3} at 750 Torr [19]. Lasing experiments were not performed using this discharge.

Continuous wave lasing was achieved using a similar discharge to the one above [19]. Stainless steel electrodes were used that were 20 mm long and 6 mm wide. Instead of both electrodes having square cross sections, one of the electrodes had one side formed into a pointed edge as shown in Figure 3(g). The distance between the pointed edge of one electrode and the flat side of the other was 2.5-3 mm. The discharge was pulsed at 200 kHz with 1,000 V pulses having a width of 80 ns. The reduced electric field at 150 Torr would then be 83 Td and 69 Td for gaps of 2.5 mm

and 3 mm respectively. The time averaged Ar($1s_5$) number density was measured to be 1.4×10^{13} cm^{-3} for a 5% Ar/He mixture at 400 Torr. Lasing experiments were performed and an output power of around 2.6 W was achieved when pumping with a diode pump power of 14 W [19].

Recently DPRGL output power was scaled to 4.1 W using a 1500 V pulsed parallel plate discharge as the production mechanism [14]. The discharge electrodes were 0.63×0.63 cm stainless steel bars that were 3.0 cm long and separated by 0.26 cm. Discharge pulses were 80 ns long with a repetition frequency of 200 kHz. The gas was a 5.3% Ar/He mixture at 720 Torr. A 41 W tunable diode laser, with approximately 21 W of output power overlapping the $1s_5 \rightarrow 2p_9$ transition, was used to create the population inversion. The cavity mirrors consisted of a >99% reflective high reflector and a 40% reflective output coupler.

2.5 Microhollow Cathode Discharges

Another discharge that has been studied for other uses is the microhollow cathode (MHCD). A MHCD is composed of an anode and cathode separated by an insulator, with a hole through the center, as shown in Figure 3(h). The holes are typically 100-300 μm in diameter and the thickness of the electrodes and insulator may vary between 30-300 μm. The development of the discharge has a few stages, based on the discharge current [36]. Initially at low currents the discharge forms in the center of the hole along the axis, referred to as the pre-discharge. As the pre-discharge forms, it becomes an anode that changes the electric field. Initially the electric field is axial, or close to axial, from the anode to the cathode. Because the pre-discharge acts as an anode the electric field changes from axial to radial. This causes electrons from the cathode to accelerate radially. The electrons then oscillate about the axis, collide with atoms and transfer their energy. During this stage of the discharge there is a large

drop in voltage as the current is increased. This is the stage that is generally referred to as the hollow cathode discharge. A common parameter used to characterize MHCD is the pressure times hole diameter, or pD. Schoenbach et al. did several experiments with various hole diameters and pressures and reported that when pD values were higher than around 5 Torr cm that the predischarge no longer formed along the axis and as a result the hollow cathode discharge never formed [36]. Despite this, the term MHCD is still commonly used to describe the discharge geometry, rather than represent the hollow cathode mode. More general terms such as "microplasma", "microcavity plasma", or "microdischarge" have been used to avoid confusion with the discharge geometry and operating characteristics [3]. In the present work the term MHCD will be continue to be used to describe the discharge geometry.

Penache et al. characterized a single DC MHCD in pure argon with a flow rate of 100 ml min^{-1} [28]. The MHCD was made of copper electrodes 130 μm thick with a 50 μm insulator (Kapton) between them. The hole diameter was 300 μm and the pressure range was 50-400 mbar (37.5-300 Torr). Using diode laser absorption spectroscopy, population densities were measured on both metastable ($1s_5$ and $1s_3$) and resonance ($1s_4$ and $1s_2$) levels. The lowest level ($1s_5$) had the highest density and was in the range of 1.9 $\times 10^{14}$ to 6.3×10^{14} cm^{-3}. Figure 4 shows the densities as a function of pressure. One of the lasers broke during the experiment so the data for $1s_3$ is incomplete. The other three levels all showed an increase in number density as the pressure increased and were in the range of approximately $2 \times 10^{12} - 2 \times 10^{13}$ cm^{-3}. The electron number density was calculated from the Stark broadening and shift and it ranged from 9×10^{14} to 5×10^{15} cm^{-3}. The spatial distribution of the plasma above the cathode surface was nearly hemispherical, but extended slightly more vertically. At 50 mbar (37.5 Torr) the vertical extent was ~1.8 mm, and as pressure increased the height decreased to ~1.5 mm at 300 mbar (225 Torr) [28].

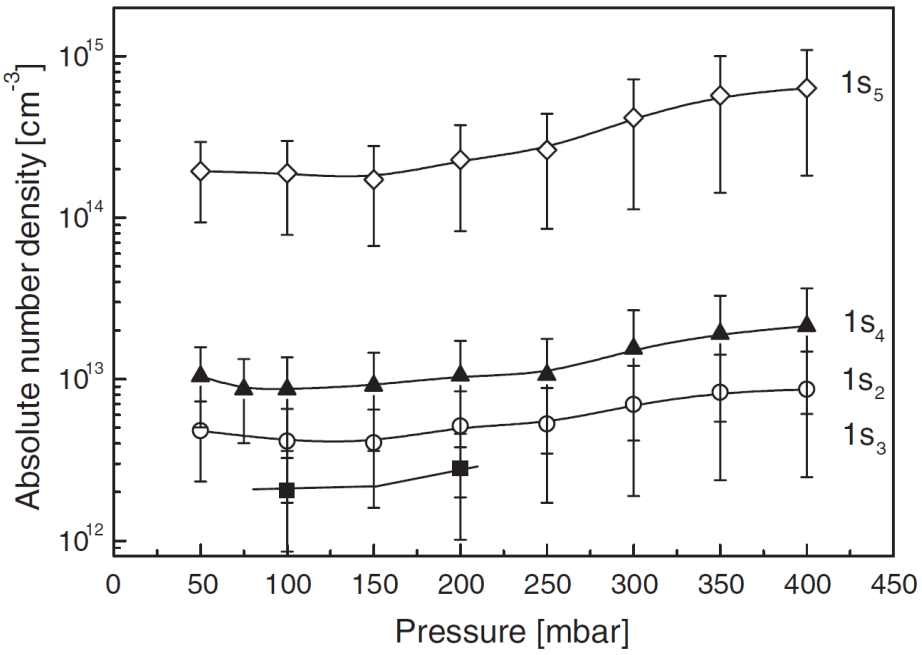

Figure 4. Argon 1s number densities from a discharge with a 300 μm diameter hole and 50 μm thick dielectric determined by Penache et al [28].

A single DC microhollow cathode with a third electrode has also been used to produced a stable discharge in atomspheric pressure (760 Torr) [38]. The electrodes were made of 100 μm thick molybdenum foil and separated by 200 μm of mica with a hole diameter of 100 μm. The third electrode had a positive potential and was placed less than 1 cm away, and parallel to the MHCD. Figure 5 shows the results from a single DC microhollow cathode at both 160 Torr (a) and 760 Torr (b) in pure Ar. At 160 Torr the cathode potential was 259 V and the bias plate was 0.5 cm away with a potential of 77 V. At 760 Torr the cathode potential was 169 V and the bias plate was 0.2 cm away with a potential of 213 V. The Ar* density was not measured during these studies. The electron density at 760 Torr was estimated to be 7×10^{11} cm^{-3} [38].

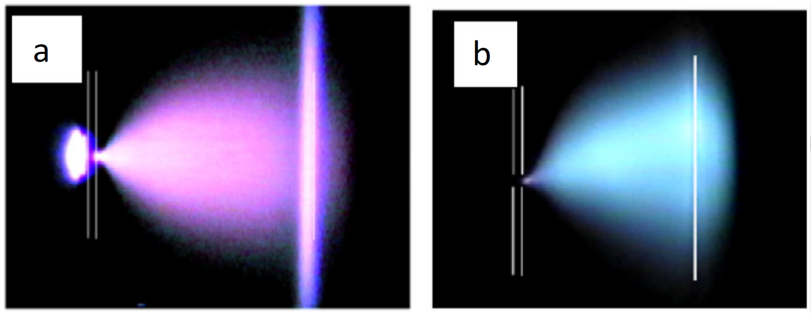

Figure 5. Microcathode structured discharges from a single 100 μm diameter hole at pressures of (a) 160 Torr and (b) 760 Torr in pure argon. The lines show the locations of the MHCD and the extra anode. The distance between the extra anode and cathode is (a) 0.5 cm and (b) 0.2 cm [35].

2.6 Laser Absorption Spectroscopy

Laser absorption spectroscopy (LAS) can be used to characterize the discharge and determine the concentrations of atoms in the 1s manifold. LAS is done by comparing the intensity of the laser incident on a medium, I_0, to the intensity of the laser after propagating through the medium, I, as the laser frequency is scanned over the transition of interest. For a collimated laser beam with intensity below the saturation intensity of the medium, the propagation through the medium is described by the differential equation

$$\frac{dI}{dz} = -\alpha(\nu)I. \tag{2}$$

The saturation intensity is given by

$$I_s = \frac{h\nu}{\sigma_{stim}\tau}, \tag{3}$$

where h is Plank's constant, σ_{stim} is the stimulated emission cross section, and τ is the lifetime of the state. In Equation (2), α is the absorption coefficient

$$\alpha(\nu) = \sigma_{abs}(\nu)n, \tag{4}$$

where σ_{abs} is the absorption cross section and n is the concentration of absorbers.

The solution to Equation (2), with variable substitutions made, can be put in the form of the Beer-Lambert law where the absorbance over a path length l_g is defined as

$$A(\nu) = -\ln\left(\frac{I(\nu)}{I_0(\nu)}\right) = \sigma_{abs}(\nu) n l_g. \tag{5}$$

The absorption cross section is related to the stimulated emission cross section by

$$\sigma_{abs}(\nu) = \frac{g_2}{g_1}\sigma_{stim}(\nu), \tag{6}$$

where g_2 and g_1 are the degeneracies of the upper and lower states respectively. The stimulated emission cross section is given by

$$\sigma_{stim}(\nu) = \frac{A_{21}\lambda_0^2}{8\pi} g(\nu), \tag{7}$$

where A_{21} is the spontaneous emission Einstein coefficient from the upper to lower lasing states, λ_0 is the central wavelength, and $g(\nu)$ is the line shape function. Putting this all together gives the absorbance for a specific frequency as

$$A(\nu) = -\ln\left(\frac{I(\nu)}{I_0(\nu)}\right) = \sigma_{abs}(\nu) n l_g = \frac{g_2}{g_1}\frac{A_{21}\lambda_0^2}{8\pi} n l_g g(\nu). \tag{8}$$

The line shape function $g(\nu)$ is normalized so

$$\int_0^\infty g(\nu)\,\mathrm{d}\nu = 1. \tag{9}$$

The number density can be found by integrating Equation (8) over all frequencies and solving for n,

$$n = \frac{g_1}{g_2}\frac{8\pi}{A_{21}\lambda_0^2\, l_g}\int_0^\infty A(\nu)\,\mathrm{d}\nu. \tag{10}$$

For a given atomic transition everything in front of the integral is constant except for the absorption path length. The path length and absorbance are dependent on the discharge geometry and operation.

III. Experiment

3.1 Microhollow Cathode Discharge Specifications

In this work the microhollow cathode discharges consisted of 2.54 cm × 5.08 cm copper foils 35.5 μm thick separated by a dielectric material (Arlon 85N fiber-glass reinforced polyimide) that was either 127 μm or 254 μm thick. Hole diameters of 100, 200, 300, and 400 μm were made by laser drilling using a pulsed Oxford laser system operating at 532 nm with a 3 kHz repetition rate of 15 ns wide pulses, resulting in an average power of 2.5 W. In early tests, the plasma breakdown occurred on the edges of the plate rather than in the hole, especially at pressures below 300 Torr. To prevent this, a small portion of the copper was stripped off the dielectric around three edges. The edge where the power supply electrode contacted the plate on each side was left unchanged. Figure 6 shows a 400 μm hole and 127 μm thick dielectric plate with the copper trimmed off the edges. The plate was held in place using a custom

Figure 6. Microhollow cathode discharge used in the present work. The copper on each side of the plate was trimmed back to ensure plasma breakdown would not occur around the edges of the plate.

Macor mount shown in Figures 7 and 8. The mount was designed to clamp the plate between the electrodes to make an electrical connection without permanently affixing them. For the plates with a 127 μm dielectric, thin pieces of Teflon were used between the mount and electrodes to ensure an electrically tight clamp. Cutouts in the mount

allowed for laser propagation through the hole, viewing the perpendicular florescence, and gas flow across the substrate.

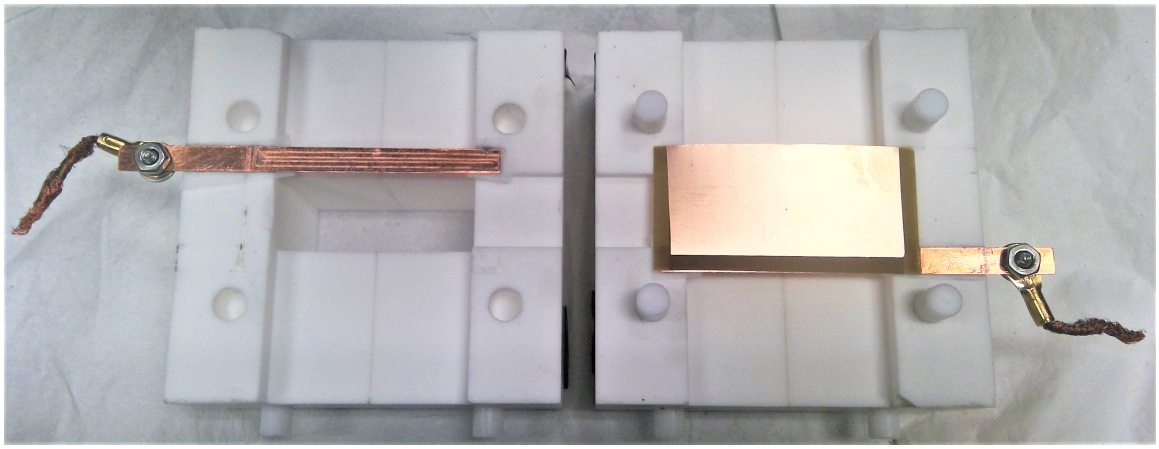

Figure 7. View of the mount open showing how the plates were installed. On the left small thin pieces of Teflon can be seen between the electrode and mount to provide a tight fit. The rectangular hole in the center was for the laser propagation and there is a similar hole on the right half under the plate. The channel cut out from the top to bottom was for gas flow across the plate. The smaller channel shown on each half near the image center was for viewing the florescence.

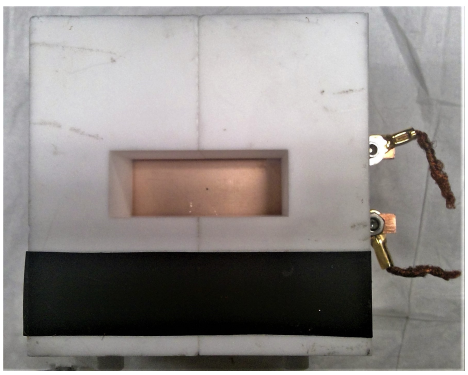

Figure 8. End on view of the assembled plate and mount. The black strip is electrical tape used to help hold the mount together while it was placed in the vacuum chamber.

The MHCD was connected to a high voltage power supply with a ballast resistor (50-100 kΩ) to limit current. Two Fluke 87V digital multimeters were used to measure the plasma breakdown and sustaining voltages as well as the current. Voltages were measured across the electrodes connected to each side of the discharge. The current

was measured between the ballast resistor and the electrode.

Pure argon was used for all experiments and fixed at a flow rate of 500 sccm using a Sierra Instruments SmartTrak 50 Series mass flow controller. The pressure was measured both upstream and downstream of the Ideal Vacuum 6" × 6" × 6" aluminum alloy vacuum chamber holding the MHCD using MKS Baratron 690A pressure transducers with a peak measurable pressure of 1,000 Torr and an accuracy of ±1.2 Torr. The average of the two measurements was taken as the total pressure in the chamber, which was varied from 50 to 1,000 Torr. The gas flow was from the top to bottom of the chamber, across the plate surface.

3.2 Tunable Diode Laser Absorption Spectroscopy Setup

The experiment setup used for the TDLAS measurements is shown in Figure 9. A New Focus Velocity 6314 tunable diode laser, with a line width less than 300 kHz, was driven by a function generator to scan over the $1s_5 \rightarrow 2p_8$ transition (801.6990 nm). The scan range was 47 GHz at a rate of 198 MHz/s. An RF dielectric barrier discharge (DBD) cell was kept at low pressures (< 2 Torr) and used as a reference for the center frequency location. Polarizing beam splitters (PBS) were used to separate the incident, I_0, and transmitted, I, beams for both the DBD and MHCD. For the MHCD the transmitted beam was through the hole. Dual frequency chopper wheels modulated each beam at 1.7 and 1.9 kHz, respectively. The intensities were tracked using two photodiodes (Thorlabs PDA10A), one for the reference cell I and I_0 and a second for the measurement cell I and I_0. The output voltages from the photodiodes were sent to a set of four lock-in amplifiers (SR850) with each one referenced to the appropriate chopping frequency for noise filtering. The parameters on the lock-ins were chosen to avoid the convolution of an instrument line shape to the measurements, which facilitates a simpler analysis. The lock-in integration time constant was set to

100 ms. The product of the time constant and scan rate give an effective instrument line width of 19.8 MHz. Because the lock-in instrument line width is much larger than the laser line width there is no convolution of the two. The convolution of the instrument line shape and atomic line shape is also avoided because the instrument line width is much smaller than the measured atomic line width (> 1 GHz).

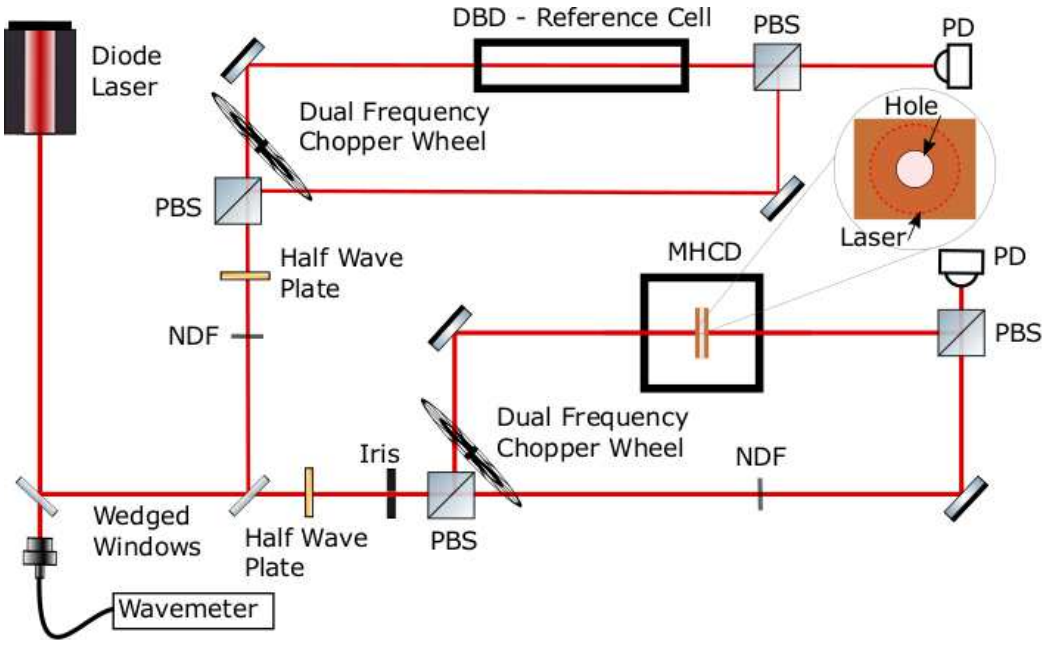

Figure 9. Experiment setup for laser absorption spectroscopy. Transmission is measured through the MHCD hole and the laser flood illuminates the holes as shown in the inset.

The laser, at a power of 70 μW and a spot-size of approximately 3 mm x 1 mm, flood illuminated the hole so that only a fraction (0.1 - 1.4 %) of the power was transmitted. This power was chosen such that the transmitted intensity was below the minimum possible saturation intensity of the transition of interest. The saturation intensity was determined from Equation (3) using the central peak frequency and the maximum cross section and lifetime. Assuming only radiative losses, the lifetime is the inverse of the sum of the Einstein A coefficients which is $\tau = 31$ ns for the $2p_8$ state [22]. The actual lifetime is shorter due to other losses such as collisional

quenching, which would increase the saturation intensity. The stimulated emission cross section is determined from Equation (7) with $A_{21} = 9.29 \times 10^6$ s^{-1} [22], and $\lambda_0 = 801.6990$ nm. The peak in the line shape function at 50 Torr was used to give the largest possible cross section of $\sigma = 1.5 \times 10^{-12}$ cm^2. Using Equation (3), the minimum saturation intensity is 5.2 W/cm^2, significantly larger than the incident laser intensity of 0.74 mW/cm^2.

A FLIR Grasshopper GS3-U3-32S4M-C camera with a $f/16$, 25 mm lens was used to take side-on and end-on images of the florescence. The side-on images (perpendicular to laser path) show the extent of the plasma away from the plate surface. These images help determine the path length for calculating the number density. To spatially calibrate the camera, images were taken of each plate in place to determine the plate location and the spatial calibration factor (μm/pixel). For the side-on images it was difficult to obtain exact alignment with the plates because the mount only fixed the corners, so the flexible substrate was free to bend. Due to this each plate's position and orientation varied slightly. The known thickness of the plates were used to get an average calibration factor of 12 ± 2 μm/pixel. For the end-on images the expected hole diameters were used to obtain a calibration factor of 15 ± 1 μm/pixel.

IV. Results and Analysis

4.1 Breakdown Voltages

The breakdown voltages for all the discharges are shown in Figure 10 with the 254 μm and 127 μm gaps represented by blue and red, respectively. The plates had lifetimes that varied from approximately 5 minutes to 2 hours. The plates appeared damaged after use, showing signs of burning and hole degradation, which will be discussed in section 4.2. Data was collected for as many cases as possible, and the various datasets are represented by different shapes in the figure. There is no data for the 100 μm and 200 μm hole plates at higher pd values because none of the available plates worked long enough to test at higher pressures. The solid line in the plots on the left in Figure 10 is a Paschen curve calculated from Equation (1) using the parameters $A = 12$ cm^{-1} Torr^{-1}, $B = 180$ V/(cm Torr), and $\gamma_{se} = 7 \times 10^{-3}$, found in literature from experimental determinations [1, 32]. The curve is meant as a reference to what the expected shape of the data might be, as it is not known how much micro-discharges follow the same behavior as macroscopic discharges. The parameters used for the Paschen curve also vary with the reduced electric field, E/p, where E is the electric field and p is the pressure [1]. The sharp decrease and subsequent rise in voltage as pd increases was not observed for most of the data collected. It could be that the minimum in the Paschen Curve occurs at a lower pd value than was tested. Discharge operation tests performed at pressures below 50 Torr all failed to achieve breakdown except for one case at 37 Torr. The data from plates with a 200 μm hole and 127 μm gap do have a similar shape to the Paschen curve, but with a shallower slope. The slope is determined by the gas constant B. The constants used had an applicable E/p range of 100-600 V/(cm Torr) [32, 1]. The reduced electric field from the experiments is shown on the right in Figure 10, with the applicable range for the

gas constants marked with horizontal lines. Note that only a small sample of the data is within the applicable E/p range for the gas constants used, which could explain why the data at higher pd values do not agree. It could also be that microdischarges do not follow the predicted Pachen curve for macroscopic discharges.

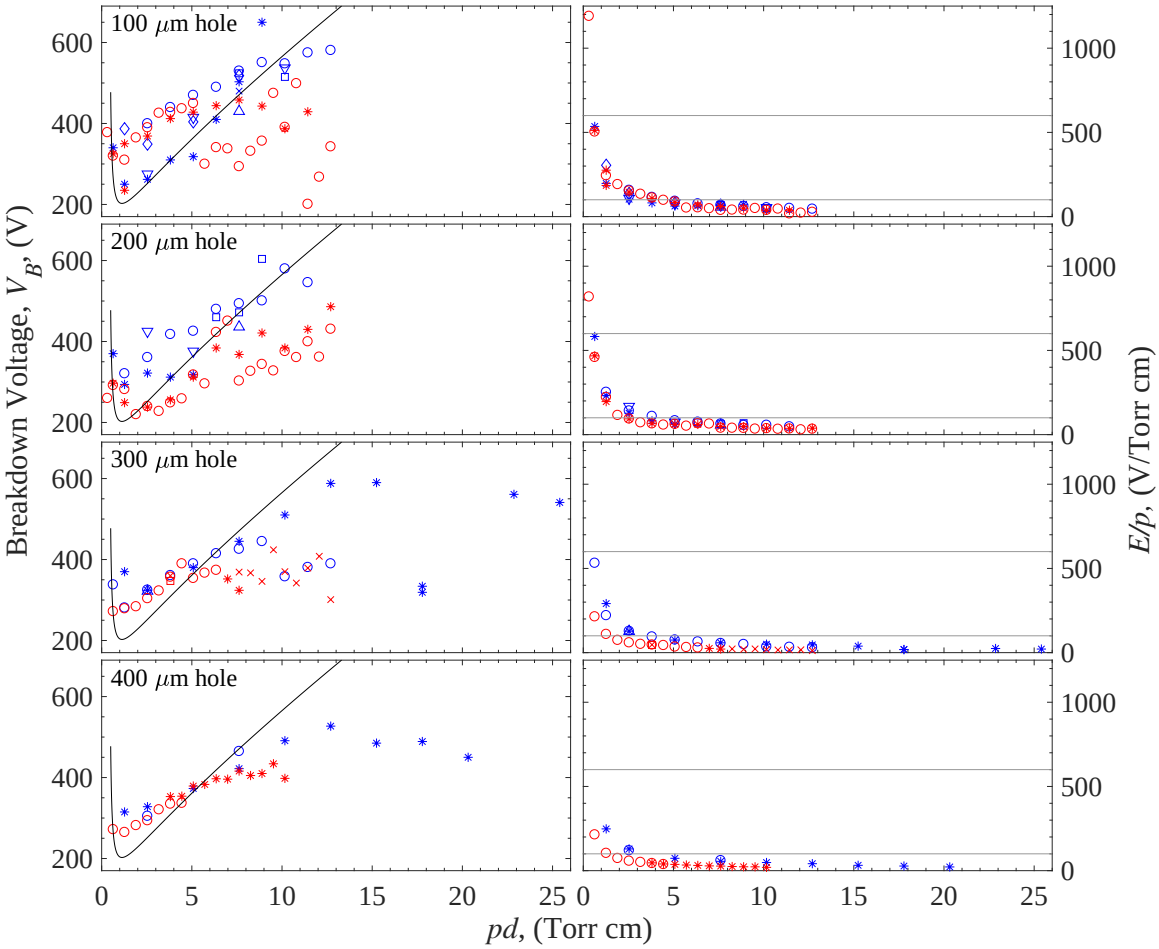

Figure 10. (Left) Plasma breakdown voltages as a function of the pressure times electrode separation distance. The red and blue data points represent 127 μm and 254 μm thick dielectrics respectively. The different marker shapes represent different plates that were used. The theoretical Paschen curve is also shown using gas constants and the secondary emission coefficient from literature [32, 1]. (Right) The reduced electric field E/p corresponding to the data on the left, with the applicable range for the gas constants marked by horizontal lines.

Many of the breakdown voltages for identical plates are not consistent, but do show an overall trend to increase as pd increases. The breakdown voltages for the

larger gap are all larger for the 200 μm hole plates, but this was not true for the other hole diameters. There was no discernible relationship between the hole diameters and required breakdown voltages. A relationship between hole diameters was not necessarily expected, but the large spread in breakdown voltages was surprising. The spread in the data does decrease as the hole diameter increases, but this is likely because fewer plates were used to collect the 300 μm and 400 μm data. The lifetime of the plates and the scatter in breakdown voltages are likely due to different manufacturing defects, as well as wear on the plates caused by repeated breakdown and operation, both of which will be discussed in the next section. The breakdown voltages at *pd* values higher than 15 Torr cm tend to decrease, but the data is scarce in that region and may not completely represent true MHCD behavior. Damage to the holes from operation could also cause different breakdown behavior. There is also a sudden drop in the breakdown voltage for the 300 μm hole 254 μm gap plate around 18 Torr cm. When the low breakdown voltage was initially observed the discharge was turned off, and tested again, but the breakdown voltage did not change drastically. When the pressure was increased, the breakdown voltage increased to approximately what it was before. Another likely explanation for the lack of consistency in breakdown voltages and strange behavior at higher *pd* values is due to changes to the hole structure during use, which will also be discussed in the next section.

Most of the sustaining voltages of the plasma for all plates were in the range of 150-190 V, with a few outliers as shown in Figure 11. A majority of the plates had sustaining voltages that were all within a 15-20 V range for all pressures tested. The range was as low as 10 V for a couple plates and greater than 30 V for others. There is no clear trend for the sustaining voltages with pressure, some cases increase, and others decrease. There does seem to be a slight decrease in the sustaining voltages as the hole diameter increases. The current flow was always less than 5 mA and

was dependent on the voltage drop across the ballast resistor according to Ohm's law. The sustaining voltage did not seem to change with the applied voltage so as the applied voltage increased the voltage drop across the resistor increased, and the current increased as expected.

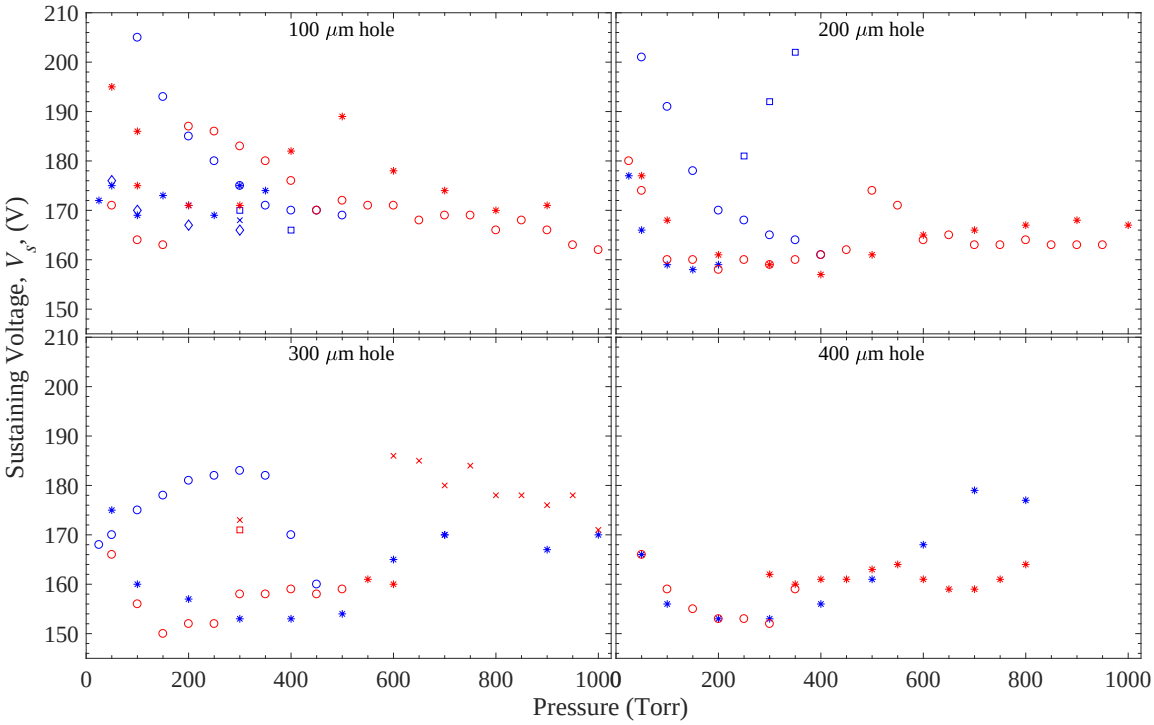

Figure 11. Plasma sustaining voltages for all plates with laser drilled holes. The red and blue data points represent 127 μm and 254 μm thick dielectrics respectively. The different marker shapes represent different plates that were used.

4.2 Material Failure

The inconsistencies in the plasma behavior and the observed electrical properties are most likely due to the manufacturing method in combination with decomposition due to use of the plates, and not the discharge design. The same process was used for all plates with the same thickness and hole diameter, yet after laser drilling, there were visual differences in holes that were supposed to be the same size. On some plates the hole was also noticeably smaller on one side of the plate than the other,

an expected result due to the kerf angle of the laser drilling process. The shape of the hole is known to greatly influence the discharge operation [29]. Figure 12 shows microscopic images of a 100 μm hole plate before (a and b) after (c and d) use. The images were taken at a magnification of 150$\times$ corresponding to a field of view of 1.5 mm and a resolution of 0.8 μm. Figure 12(a) shows the side of the plate where the laser drilling took place, which will be called the front side. The hole is slightly elliptical, and the measured hole diameter is approximately 116 μm. The hole on the opposite (back) side of the plate, shown in Figure 12(b), was measured to be approximately 95 μm in diameter. Figure 13 is a similar image for a 200 μm diameter hole. The diameter for the laser drilled side was 221 μm and the opposite side was 191 μm. Hole diameters were typically around 10% larger then expected on the laser drilled side and around 5% smaller then expected on the opposite side. There were also noticeable burn marks on the holes due to the laser drilling and jagged edges in the hole. Any of these difference could have a significant affect on the discharge operation and the ability to replicate experiment results.

The plasma itself may also be affecting the consistency and reliability of the plate operation. After use, most of the plates had significant burn marks around the holes and the diameters were clearly larger than before operation as can be seen in Figures 12 and 13 (c) and (d). This damage corresponds to a substantial local heating of the material either due directly to collisions between the walls and the plasma (sputtering) or due to the current flow. Sputtering is known to cause significant damage to both the cathode and dielectric materials [29]. The 100 μm hole was used continuously for over an hour. The hole diameters after use were 164 μm and 194 μm for the front and back side respectively. The hole diameters for the used 200 μm hole plate were 230 μm and 247 μm for (c) and (d) respectively. The 200 μm plate was not marked so it is not known whether (c) or (d) is the front. There is considerable

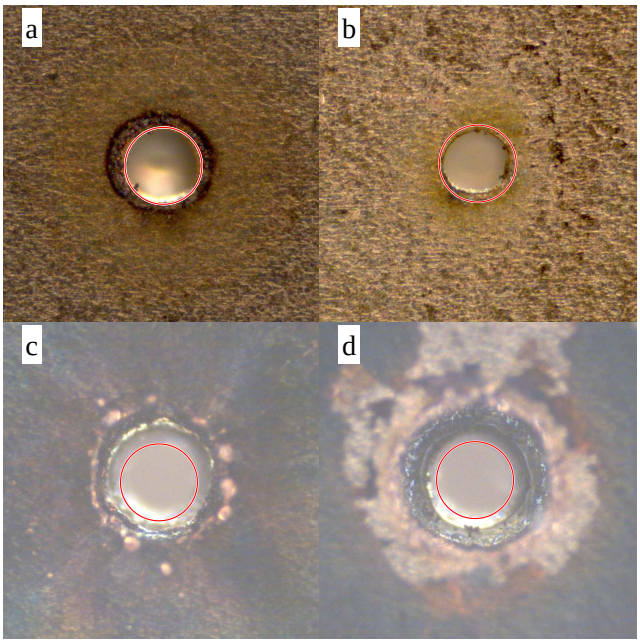

Figure 12. Images of both sides of a 100 μm hole before (a and b) and after (c and d) use. The hole was actually measured to be 116 μm (shown by the red circle) in (a) and 95 μm in (b). Images (a) and (c) are the side where the laser drilling occurred. In (a) burn marks from the laser can be seen around the hole. Jagged edges are seen in the hole in both (a) and (b). (c) and (d) both show severe burning from operation and the hole size has increased by approximately 50%. (c) also shows signs of sputtering, where copper mounds have formed around the hole.

damage in all images and sputtering is clearly evident in Figure 12(c), where there are mounds of copper on the plate surface around the hole. The height of the mounds were almost 30 μm from the plate surface. The $1s_5$ state is easily quenched and the significant rate of material loss may be greatly influencing its density.

The severity of the burn marks varies and some plates were used for hours, on and off, without any apparent problems. This could be the result of the laser drilling process, but it could also be an issue with the actual discharge materials, design or operating conditions. Figure 14 shows three 100 μm diameter hole plates that were all used for different experiments. The plate in (a/b) was used in TDLAS and breakdown voltage experiments so it was constantly turned on and off, and only operated for 1-5 min at a time. The damage caused in Figure 14 (c-f) was from continuous operation

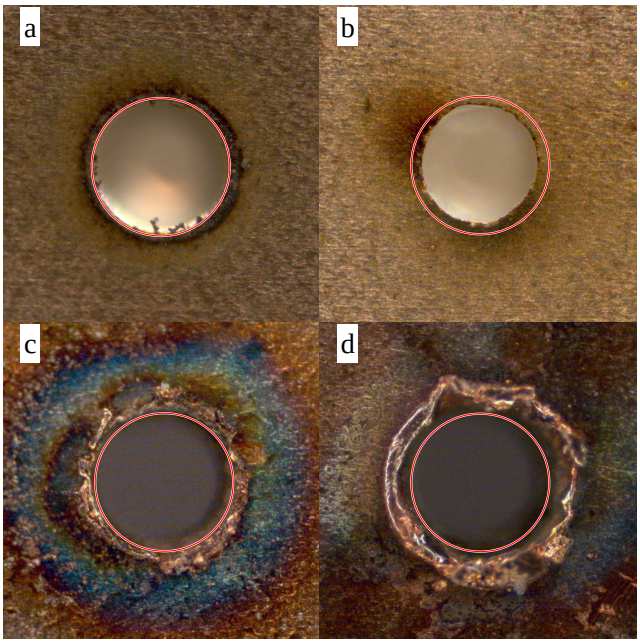

Figure 13. Images of both sides of a 200 μm hole plate before use (a and b) and a separate 200 μm hole plate after use (c and d). The hole was actually measured to be (a) 221 μm (shown with the red circles), (b) 191 μm, (c) 230 μm, and (d) 247 μm. Image (a) is the side where the laser drilling occurred and shows burn marks from the drilling process, and jagged edges inside the hole. (b) shows an imperfectly shaped hole with two localized burned regions. (c) and (d) show burning from operation and damage to the hole structures as the copper appears to be torn back or peeled away from the hole.

for over an hour. The third plate in Figure 14 is the best case that was observed after operation. There is burning on one side of the plate, but no significant observable damage to the hole. The hole diameters were not measured prior to use so it is not known if there was a change. After use the hole diameters were 123 μm and 89 μm for the front and back respectively, which means it couldn't have change by very much. Why there is such little damage compared to others plates is not known. The discharge was on for nearly two hours total. After running for around an hour and a half the discharge went out and was re-lit for another half hour. It was thought that turning the discharge on and off caused more damage than continuous operation, but Figure 14(c/d) does not support that, where significant damage can be seen. Obviously the desired result would be to have discharges with little to no damage

after use. To reduce damage and increase the lifetime, an electrode material with a lower sputtering rate than copper, such as tungsten, tantalum or molybdenum, could be used. Operating at lower currents, and using Ar/He mixtures should also decrease the effects of sputtering [29]. Note that microscopic images were taken of a handful of plates used and those not presented here are shown in Appendix A.

There were also some other strange behaviors that should be noted. For some plates plasma breakdown did not occur until the applied voltage was high enough (~600-700 V) to cause arcing in the hole. After arcing, the voltage would be decreased and in some cases plasma breakdown would occur. Other times the arcing would lead to the electrode material melting into the hole, leading to electrical continuity, and making it unusable. There were a few plates that operated well for multiple tests, and then suddenly stopped, without any arcing or breakdown. At times this was corrected by applying a much higher voltage as just mentioned to get the plate to arc, after which normal breakdown and operation was achieved. The jagged edges in the holes could be the cause of the strange behavior as they are likely to move during plasma operation, and could create an electrical connection between the electrodes.

4.3 Line Shape Fits

The incident intensity, I_0, and the signal, I, in the absence of absorption should be constant or vary only slightly as a function of frequency. It was observed that when the discharge was off there was an oscillation in I that was 5-6 times larger than the oscillation in I_0. The oscillation was determined to be due to etaloning in the vacuum chamber windows. The result was a large amplitude sinusoid in the measured absorbance baseline. Figure 15 shows the measured absorbance for a 127 μm gap plate with a 200 μm hole at six pressures. The pressure was increased from 37 Torr to 50 Torr and then to 250 Torr in 50 Torr increments, which corresponds

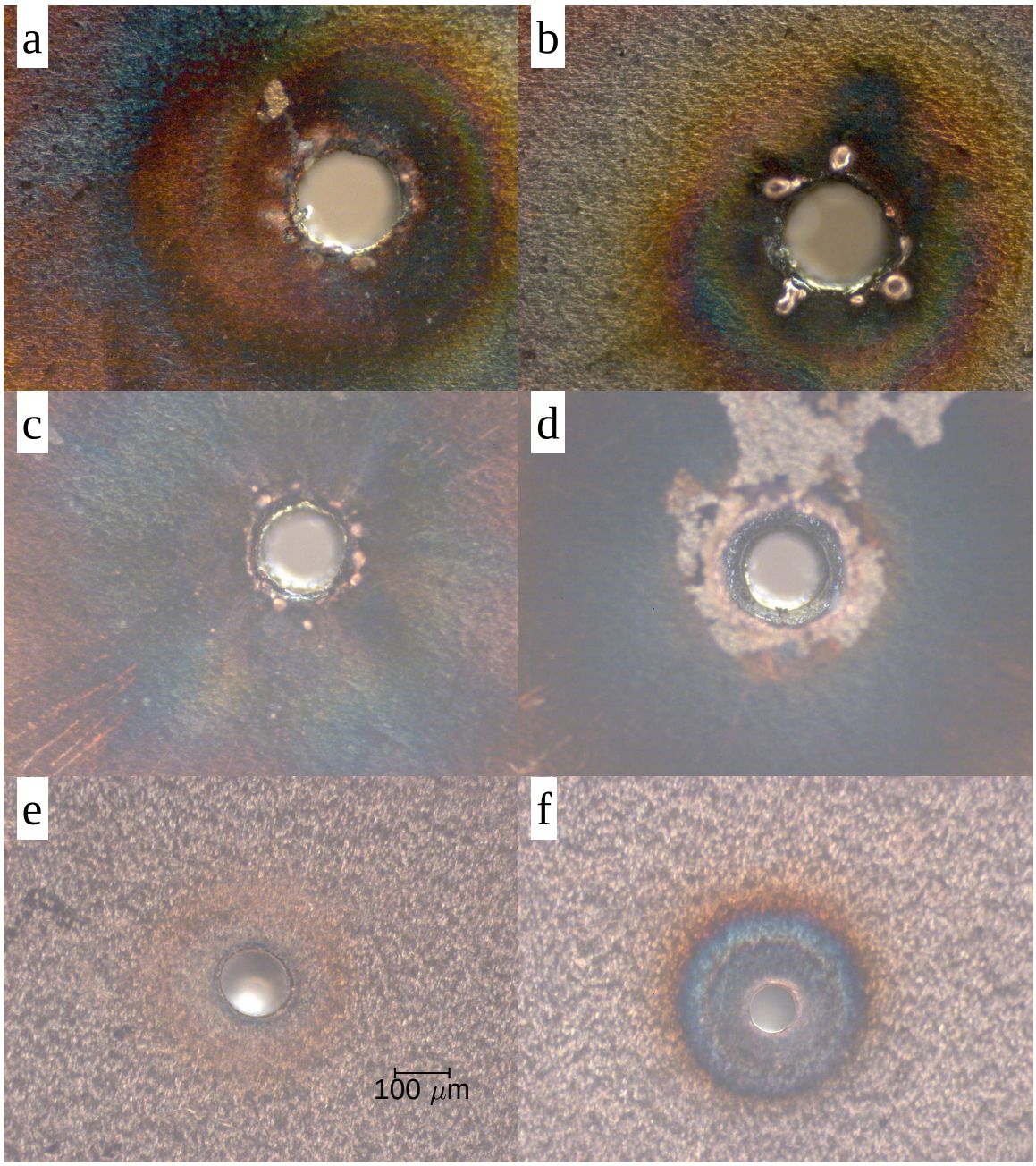

Figure 14. Images of both sides of 100 μm diameter hole plates after use. The plate in (a/b) was turned on and off multiple times and operated for 1-5 min at a time. The plates in (c/d) and (e/f) were used continuously for over an hour.

to the darkest to lightest lines respectively. With the exception of data taken at 37 Torr, the sinusoid in the data was very consistent for each pressure. It was typical for the sinusoid to be mostly consistent for other cases as well, although the positioning

relative to the absorbance peak shifted due to the variation in hole diameter from plate to plate, as well as the slightly different position of the hole in the center of the plate. Figure 16 shows a case were the absorbance peak is closer to the peak of the sine function. It also depicts a unique case where the phase of the sine function changed with each pressure. The data in Figure 16 is from a 127 μm gap, 400 μm diameter hole MHCD, at pressures of 50 to 200 Torr. Despite the large oscillation in the baseline, the red shift and broadening of the spectral line with pressure is clearly visible. The absorbance data and corresponding fits for all other discharge configurations are contained in Appendix B.

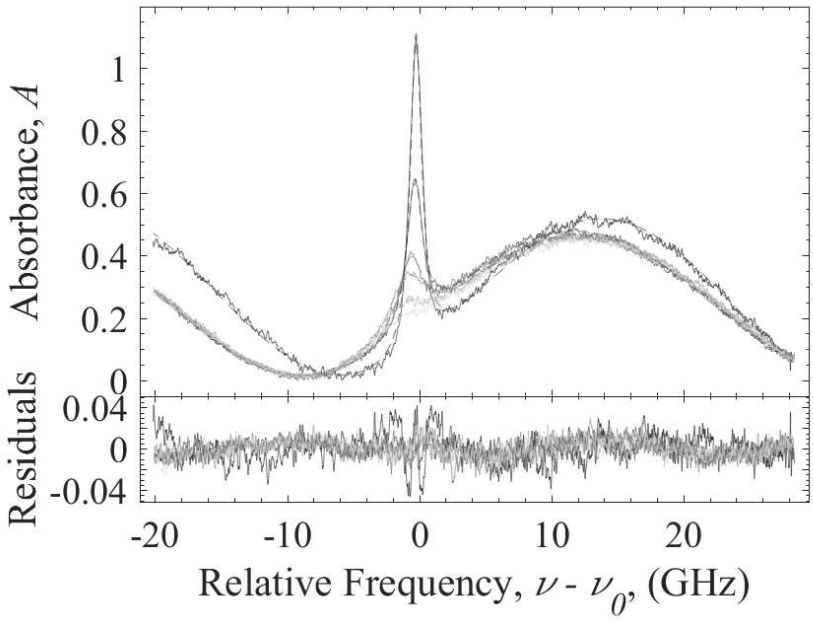

Figure 15. Absorbance data, fits, and residuals for a MHCD with a 127 μm thick dielectric and 200 μm hole diameter. The pressures used were 37 Torr and 50-250 Torr in 50 Torr increments, from darkest to lightest. A Lorentzian and sine function with a linear baseline were fit concurrently.

The measured absorbance is the frequency dependence of the absorbing atom's atomic line shape including homogeneous and inhomogeneous broadening. The main components for each are pressure broadening and Doppler broadening. Natural broad-

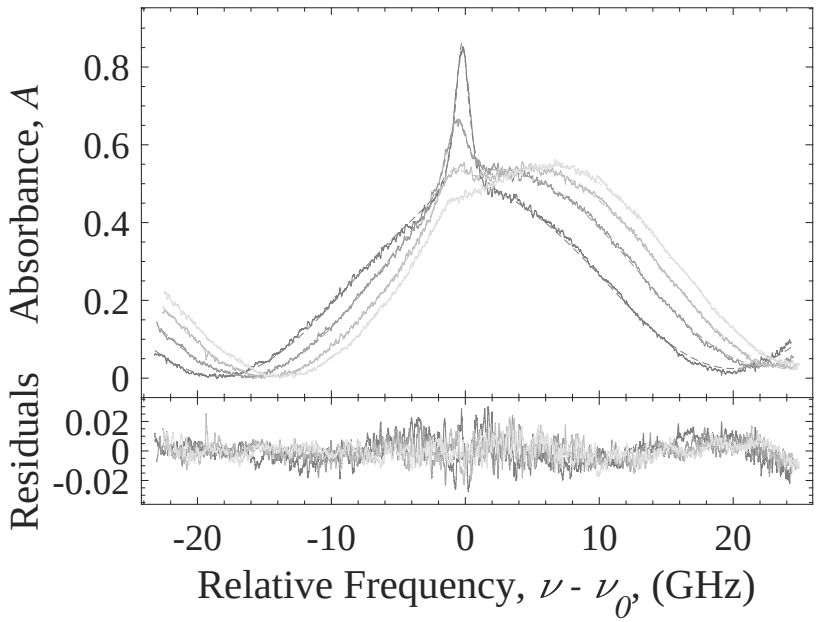

Figure 16. Absorbance data, fits, and residuals for a MHCD with a 127 μm thick dielectric and 400 μm hole diameter. The pressures ranges from 50-200 Torr in 50 Torr increments from darkest to lightest. A Lorentzian and sine function with a linear baseline were fit concurrently.

ening is given by

$$\Delta\nu_{Nat} = \frac{1}{2\pi\tau}. \tag{11}$$

For the $1s_5 \rightarrow 2p_8$ transition, $\tau = 31$ ns and $\Delta\nu_{Nat} = 5.1 \pm 0.9$ MHz. Homogeneous broadening is described by Lorentzian line shapes and inhomogeneous broadening by Gaussian line shapes [41]. The actual atomic line shape is the convolution of a Lorentzian and Gaussian or a Voigt. However, if one of the broadening mechanisms is much larger than the other, the Voigt profile will be dominated by the corresponding line shape [24].

The Doppler width is temperature dependent according to

$$\Delta\nu_D = \left(\frac{8kT\ln 2}{Mc^2}\right)^{1/2}\nu_0, \tag{12}$$

where k is Boltzmann constant, M is the atomic mass, ν_0 is the central frequency,

and T is the temperature [41]. At room temperature the Doppler width for the $1s_5 \rightarrow 2p_8$ transition is 728 MHz. To determined the temperature of the gas the measured absorbance for each case was fit to a Voigt profile. The Doppler width parameter was given a lower bound of 728 MHz and an upper bound of 1.895 GHz, corresponding to temperatures of 295 K and 2,000 K respectively. Most of the cases resulted in Doppler widths equal to either the upper or lower limit. At pressures greater than 100 Torr, the Lorentzian component dominates and a low signal-to-noise ratio (SNR) prevents an accurate determination of the Doppler width. Figure 17 shows the difference between fitting a Voigt (magenta) and Lorentzian (blue) function to the measured absorbance (red) at 37 Torr (left) and 100 Torr (right). As expected there is noticeable difference between the two at lower pressure where the Doppler and Lorentzian widths are comparable and the SNR is 70. At 100 Torr the SNR is less than half of what it was at 37 Torr, and the functions are nearly identical. In this work the highest SNR was 70 at 37 Torr and tended to decrease as pressure increased to below 10.

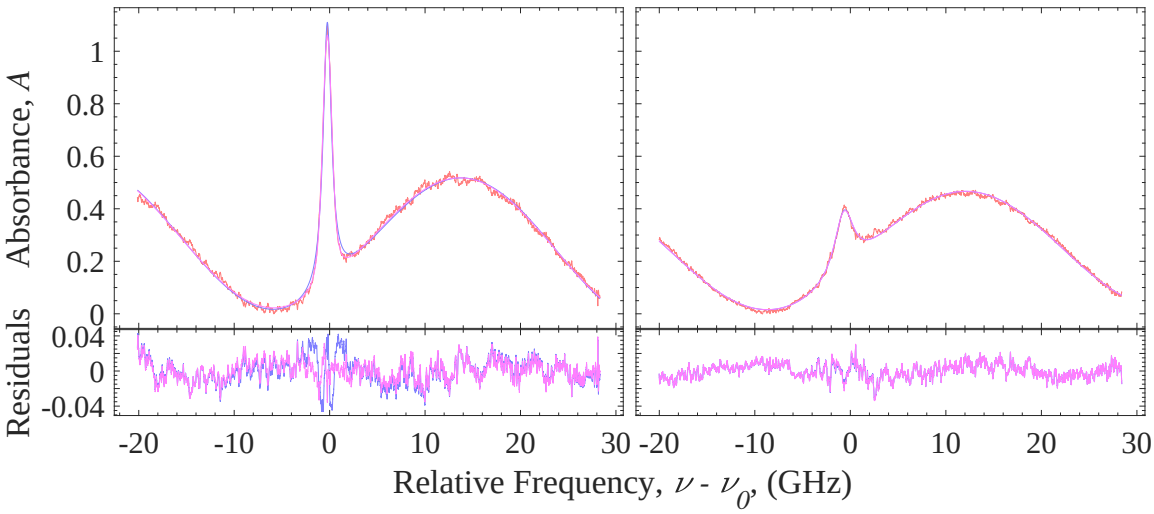

Figure 17. Voigt (magenta) and Lorentzian (blue) line shape fit comparison at 37 Torr (left) and 100 Torr (right). At 37 Torr there is a distinct difference between a Voigt and Lorentzian, but at 100 Torr the two are nearly identical.

Leiweke and Ganguly described a method to determine where the Doppler width

can accurately be determined [24] by finding the critical Voigt width in the case of an infinite SNR. An empirical equation for the Voigt width as a function of gas temperature and pressure is

$$\Delta\nu_V \approx 0.5346 \times \Delta\nu_L + \sqrt{0.2166 \times \Delta\nu_L^2 + \Delta\nu_D^2}, \tag{13}$$

where $\Delta\nu_D = 42.4\sqrt{T}$ for argon and $\Delta\nu_L$ is the pressure dependent Lorentzian width given by

$$\Delta\nu_L = \left(\frac{2\gamma}{P}\right)_0 P \left(\frac{T}{T_0}\right)^{0.3}, \tag{14}$$

where $(2\gamma/P)_0$ is the pressure broadening rate of 17.9 MHz/Torr referenced to $T_0 =$ 500 K (see section 4.4). The critical Voigt width is determined by minimizing Equation (13) with respect to T while holding the pressure P constant, giving

$$\Delta\nu_D^* = 66.9\sqrt{T}. \tag{15}$$

When the Voigt width is greater than the critical Voigt width the lineshape is predominately Lorentzian and the Doppler width can not be determined accurately. At 100 Torr the gas temperature would need to be over 900 K to be able to determine the Doppler width.

Due to the inability to accurately determine the Doppler width for most of the data range, a Lorentzian was fit to the measured absorbance. Another option is to fit a Voigt function and constrain the Doppler width based on an estimated temperature. The choice of fit does impact the Lorentzian widths, which will be discussed in section 4.4. However, the number density results were not significantly different for the cases tested. The area normalized Lorenztian function has the form

$$g_L(\nu) = \frac{\Delta\nu_L}{2\pi((\nu - \nu_0)^2 + (\Delta\nu_L/2)^2)}. \tag{16}$$

Because of the oscillation in the baseline of the measured absorbance, the Lorentzian was fit concurrently with a sine function and a linear offset. The fit parameters in Equation (16) are the Lorentzian width $\Delta\nu_L$ and the central peak frequency ν_0. The central frequency was measured relative to the reference cell peak, so that it is the pressure induced shift in the line shape. The fits and the corresponding residuals are also shown in Figures 15 and 16 with the absorbance data for the specified cases.

4.4 Pressure Broadening and Shift Rates

The pressure broadening and shift rates for the line shape are obtained from the Lorentzian widths and shifts as a function of pressure. The widths and shifts from all four hole diameters for both the 127 and 254 micron gaps are plotted in Figure 18. The widths and shifts are not dependent on discharge geometry so the values from each discharge should be in agreement. The pressure broadening and shift rates are the slopes of the data, found using a weighted linear fit. For the fit, each point was weighted by the inverse of its uncertainty squared. The pressure broadening rate from the Lorentzian fits was also compared to the rate by using a Voigt fit for pressures below 100 Torr as well as rates found in the literature.

The results from using the Lorentzian fits are a pressure broadening rate of 16.1 ± 1.4 MHz/Torr and a shift rate of -6.3 ± 0.3 MHz/Torr. In vacuum the Lorentzian width would be the natural line width, determined by Equation (11). From the fit, the width at vacuum is much higher at 503 ± 118 MHz. This is in part a result of fitting a Lorentzian, and excluding the Doppler component, to the low pressure data. The Voigt width is a complicated function of the Lorentzian and Doppler widths [27], and including the Doppler width would reduce the Lorentzian width compared to that from fitting a Lorentzian, as shown in Figure 19. For most cases, at pressures of 100 Torr and less there was a significant decrease in the Lorentzian width when a Voigt

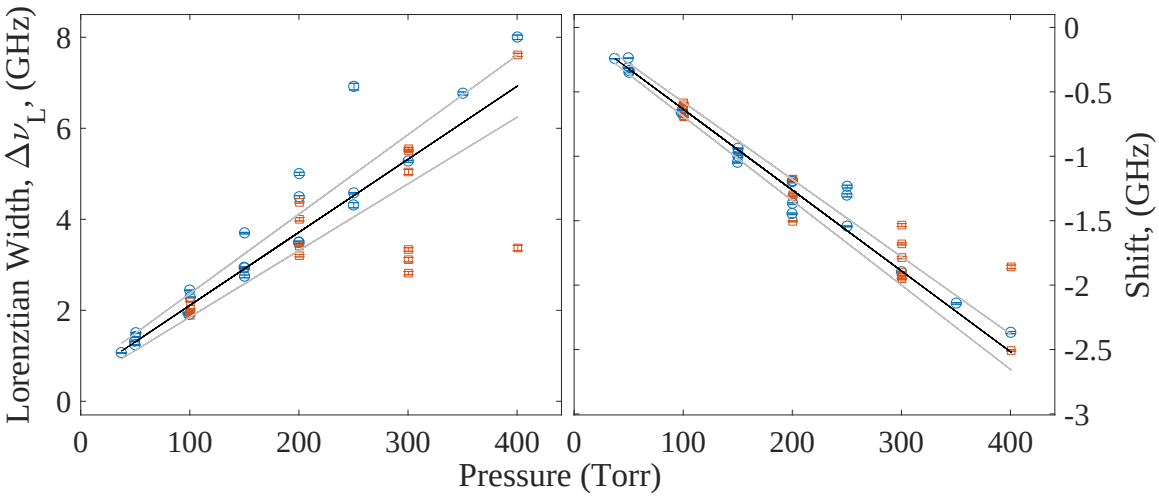

Figure 18. Lorentzian widths (left) and shifts (right) for both the 127 μm (blue circles) and 254 μm (orange squares) thick dielectric and all hole diameters. The solid dark lines are weighted linear fits which give the pressure broadening rate of 16.1 $\pm$ 1.4 MHz/Torr. and shift rate of -6.3 ± 0.3 MHz/Torr. The outliers are a result of very low SNR.

function was used. With a few exceptions the difference decreased as the pressure increased. The few exceptions were cases where the Doppler width was at the upper bound, which is due to the SNR issue described in section 4.3. As mentioned earlier, the Doppler width could not be accurately determined above 100 Torr due to low SNR. The broadening rate was recalculated using the Lorentzian widths from the Voigt fits at pressures below 100 Torr and the widths from Lorentzian fits above 100 Torr. The lower widths at low pressures increased the broadening rate to 17.9 ± 1.8 MHz/Torr and moved the intercept to 22 ± 275 MHz which is closer to the natural line width. Figure 20 shows the change in the widths and the broadening rate when the Voigt profile is used. The outliers at 250, 300, and 400 Torr in Figures 18 and 20 are cases where the SNR is very low (~10) and the fits are not as accurate.

The previous work for the 801.6990 nm line in pure argon was performed at various temperatures. To compare to the current work the data must be scaled to the same temperature. The temperature can be calculated using Equation (12)

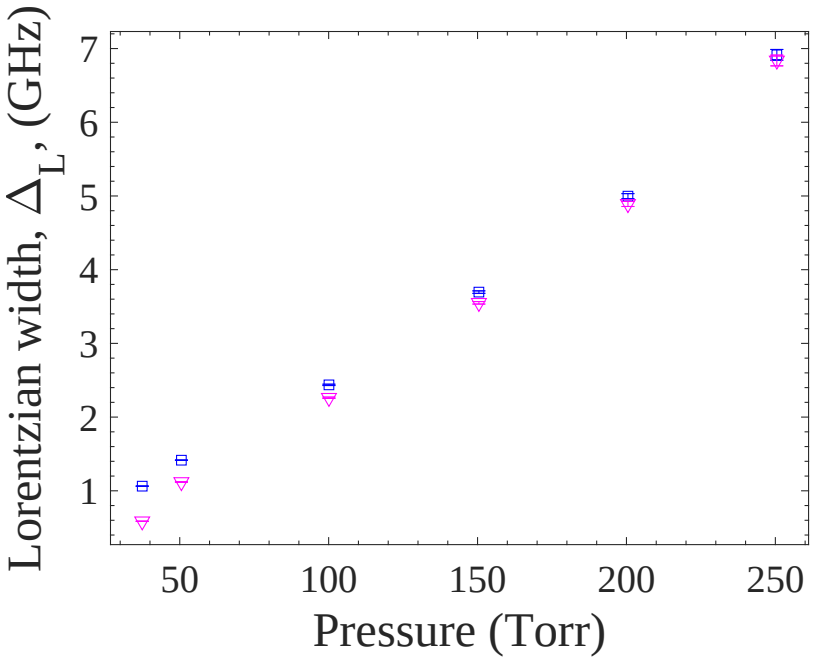

Figure 19. Lorentzian widths from a 127 μm thick dielectric, 200 μm diameter hole determined using a Lorentzian (blue squares) and Voigt (inverted magenta triangles) function. The difference in the Lorentzian width decreases as the pressure is increased.

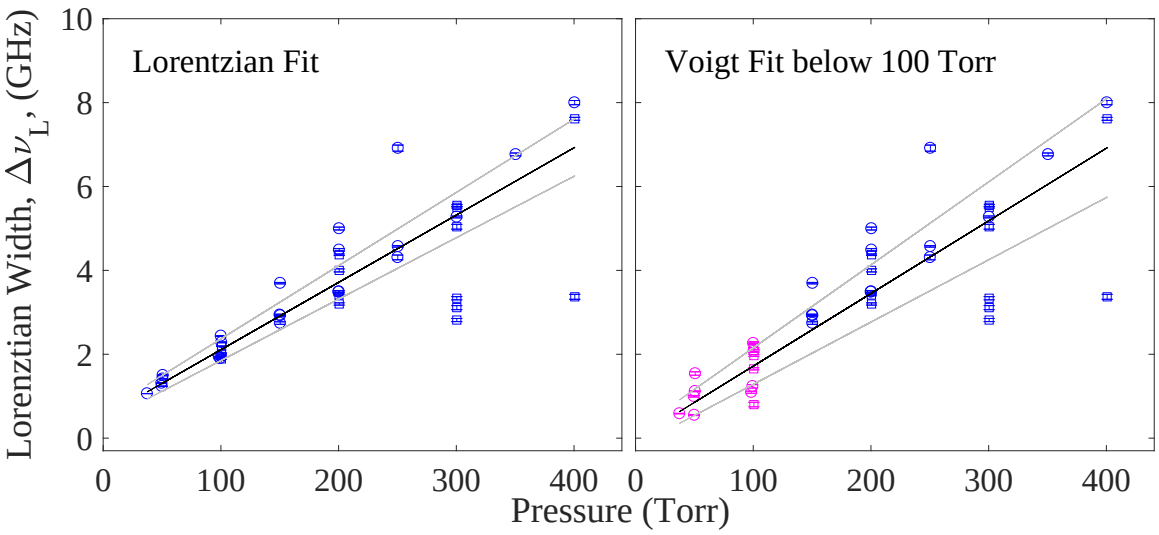

Figure 20. Broadening rates using widths from (left) Lorentzian fits (blue) at all pressures and from (right) substituting widths from Voigt fits (magenta) at pressures of 100 Torr and lower. Using a Voigt fit at low pressure increases the broadening rate from 16.1 ± 1.4 MHz/Torr to 17.9 ± 1.8 MHz/Torr.

and the Doppler widths found from the fits. Because of the inability to accurately determine the Doppler width, not all the data could be used to determine an average temperature. There were only two cases where the SNR was greater than 40, the pressure was below 100 Torr and the Doppler width was not at an upper or lower limit. From these two cases the average line of sight temperature was calculated to be 500 ± 90 K. When scaled to 500 K using the Lindholm-Foley $T^{-0.7}$ dependence the previous pressure broadening rates are 13.2 ± 1.4 [4], 13.2 ± 5.0 [26], and 8.8 ± 9.9 MHz/Torr [40]. While the broadening rate in the present work is higher, it does fall within the range of the uncertainties of two of the three reported rates.

4.5 Path Length

The path length was determined using florescence images that were not collected concurrently with absorbance data. It was initially assumed that the plasma would be sufficiently consistent for plates with similar specifications but this was later recognized as a poor assumption. The plasma extension was on the cathode side of the MHCD. Only in a few cases was any florescence observed on the anode side and it was minimal. As a result end on images were only taken on the cathode side. Figure 21 shows the side images taken of a plate with a 127 μm gap and 200 μm hole at pressures of 50-1,000 Torr. The approximate location of the plate and hole is marked by the white lines. It was expected that the plasma would be mostly symmetric around the hole and that it would constrict towards the hole as the pressure increased [28]. However, at 50 Torr there is a slight asymmetry in the plasma which increases with pressure. The plasma does tend to constrict as expected but its location also varies. End on images, such as those shown in Figure 22, also show asymmetry in the plasma and inconsistency in its location. In all cases tested (see Appendix C for complete set of images) the plasma is generally well behaved at 50 Torr but there is a lack of

consistency and repeatability at higher pressures. It is thought that defects in the plate surface and variations in manufacturing are the cause for the plasma to extend in different sections of the plate surface.

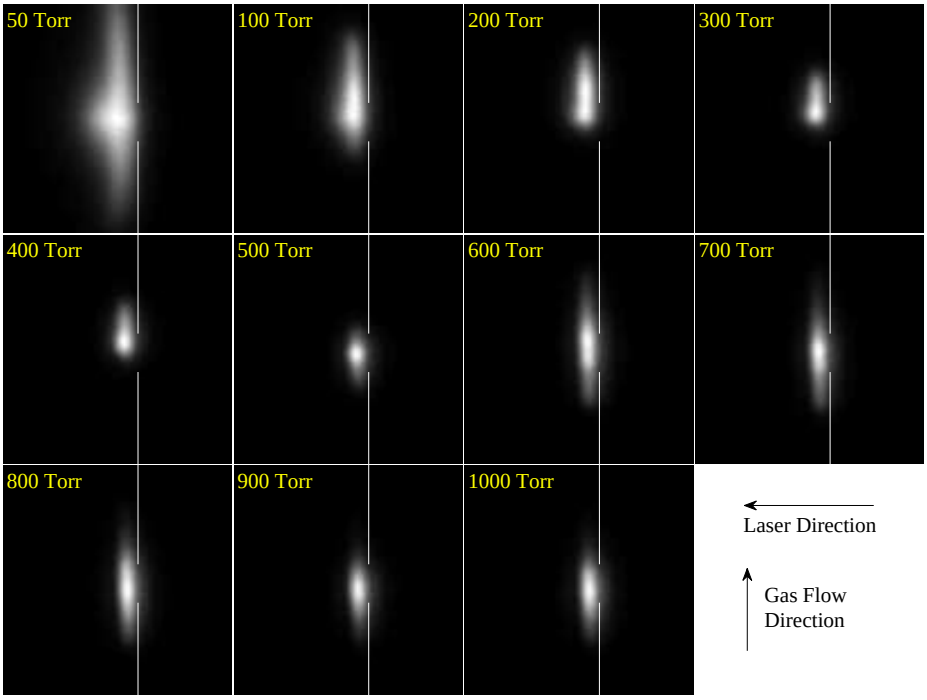

Figure 21. Side florescence from a 127 μm thick dielectric, 200 μm diameter hole MHCD. The white lines show the approximate left plate edge and hole location. The fluorescence constricts toward the plate surface as expected when pressure is increased. The asymmetry in the plasma is not expected and could be the result of plate defects such as scratches in the surface.

A major concern drawn from the images is the ability to determine the path length. From the side on images alone there is no way of knowing if the plasma is in line with the hole or to the side of it. The side on and end on images were not taken concurrently and due to a lack of consistency in the spatial behavior, correlations cannot be made between the two. Because of the uncertainty in determining the path length, a maximum and minimum path length were chosen. Even if the plasma is in line with the hole it is difficult to accurately determine the path length for absorption because there is not a well-defined edge to the region containing the metastable atoms.

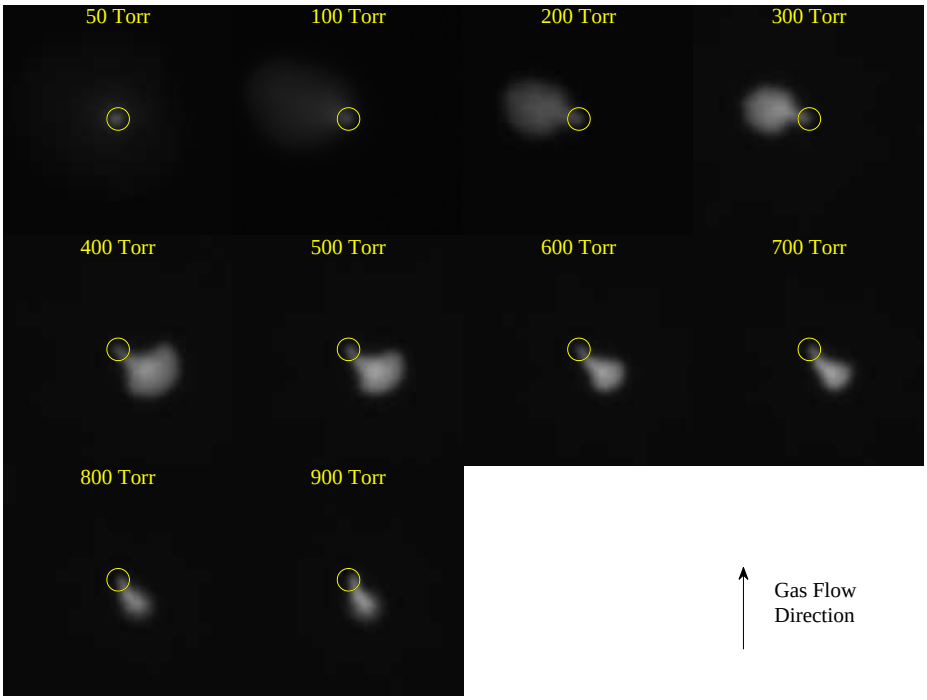

Figure 22. End-on images of a 127 μm thick dielectric, 200 μm diameter MHCD. The circle shows the approximate location of the hole. The plasma is symmetric at 50 Torr, but becomes asymmetric as pressure is increased. It is unknown what causes the location of the plasma to change, but could be a result of changes to the hole and plate during operation.

In previous work the maximum path length was taken to be the length of the hole plus the distance to the point where the florescence intensity was 10% of the maximum [28]. To compare results, the same method was used in this work. After determining the hole location, the pixel intensities in each column were added together over the range in line with the hole. The column intensities were then used to find the 10% edge. The distance from that position to the plate in addition to the thickness of the plate was used as the maximum path length. An example of the region is shown in Figure 23, marked with yellow lines. The minimum length was taken to be the width of the plate, assuming no plasma extension in line with the laser path. The resulting path lengths for the 127 μm gap and 200 μm hole are shown in Figure 24. Each point is the average of the minimum and maximum path lengths, which are shown with the error bars.

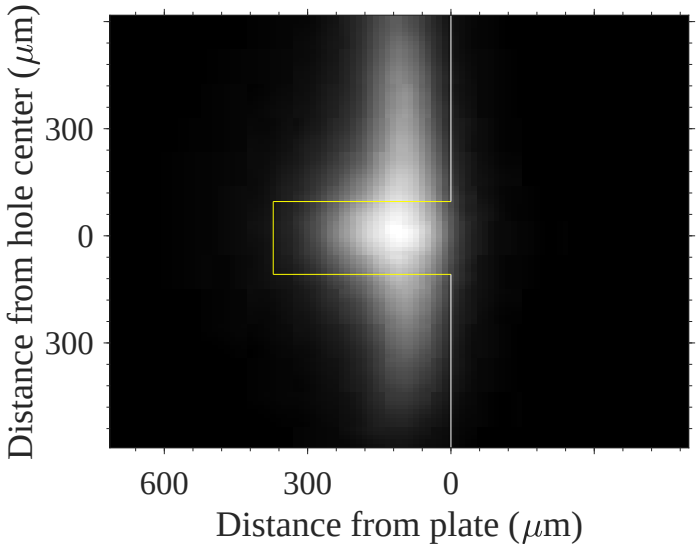

Figure 23. Side florescence from a 127 μm thick dielectric, 200 μm diameter MHCD at 50 Torr. The white lines show the approximate plate and hole location. The yellow lines show the region used to determine the maximum path length.

The plasma extension away from the plate surface was fairly consistent for all plates tested, as shown in Figure 25. The data shown only accounts for what is assumed to be in line with the hole from the side images. For two cases the plasma

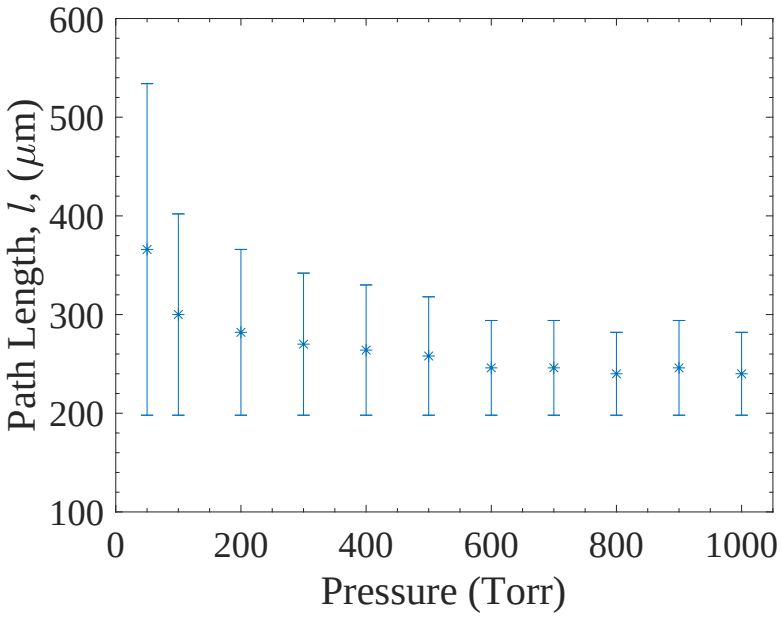

Figure 24. The absorbance path length for the 127 μm thick dielectric and 200 μm diameter MHCD. The minimum path length is set to the full thickness of the MHCD (198 μm) because it is unknown if the plasma is in line with the laser path. The maximum path length from each pressure is assuming the plasma viewed from the side images is in line with the laser path.

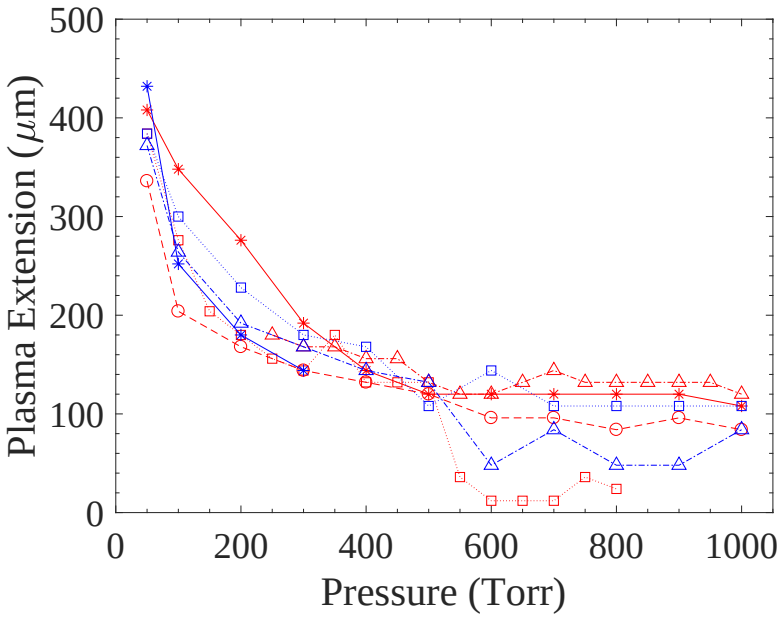

Figure 25. The plasma extension in line with the hole, as viewed from side images, for both 127 μm thick dielectric (red) and 254 μm thick dielectric (blue) plates. The hole diameters are ($*$) 100 μm, ($\circ$) 200 μm, ($\triangle$) 300 μm, and ($\square$) 400 μm.

formed almost entirely above or below the hole which is the cause for the significant drop around 600 Torr. Hole diameters and electrode separation seem to have no affect on the plasma extension. The electrode separation still affects the total absorption path length though due to changing the plate thickness.

4.6 Number Density

The Ar $1s_5$ number density for each pressure was calculated using Equation (10). The maximum possible metastable concentrations, based on using the minimum path lengths are shown in Figure 26 for both the 127 μm gap and 254 μm gap. The highest concentration was 4.0×10^{13} cm^{-3}, which was from the 127 μm gap, 100 μm hole at 400 Torr. The maximum results from all discharges tested were above 5.5×10^{12} cm^{-3}. There was no clear trend with pressure, some cases increased, some decreased and others varied back and forth. The gap thickness also did not make a significant difference. The 400 μm diameter hole number densities were the lowest, but only slightly, and there were no trends for the other hole diameters. The large drop in the 254 μm, 200 μm number density at 300-400 is likely due to a poor fit to the absorbance data because the SNR was too low.

The actual number densities could be up to three times lower than the maximum as a result of the large uncertainty in the actual path length. The average number densities are mostly around $1.0-1.5\times10^{13}$ cm^{-3} which should be sufficient for DPRGL operation. Appendix D contains the minimum, maximum and average number densities for all discharges tested. The literature for MHCD generated Ar $1s_5$ densities is scarce, but values reported by Penache [29] and Penache et al. [28] are shown in Figure 27 with black squares and diamonds respectively. The other data in the figure is from three cases in the present work; a ($*$) 100 μm and ($\circ$) 200 μm hole with a 127 μm gap, and a ($\triangle$) 300 μm hole with a 254 μm gap. The error bars mark the max-

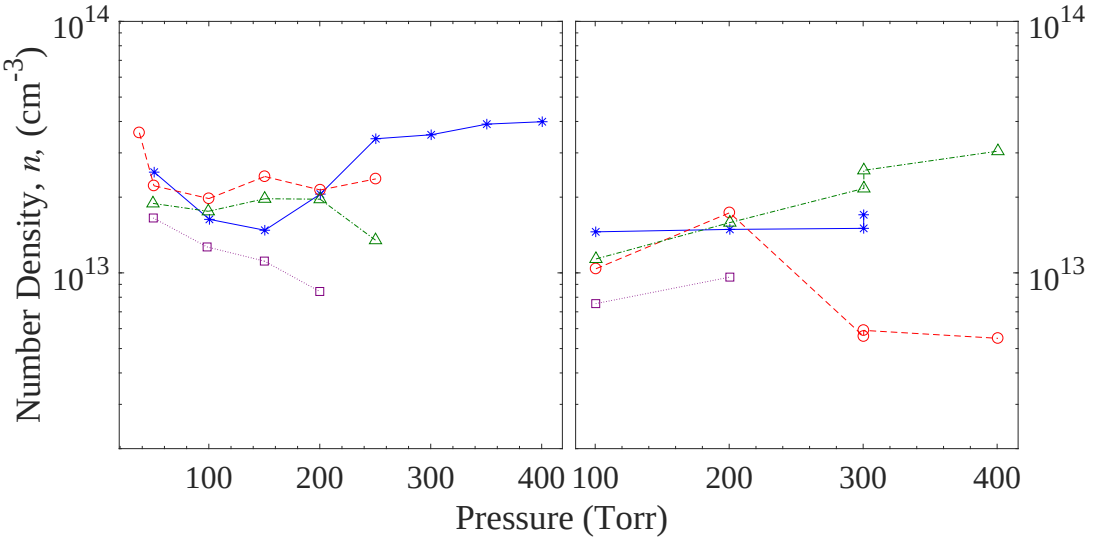

Figure 26. Maximum number densities from MHCDs with a 127 μm thick dielectric (left) and 254 μm thick dielectric (right). Hole diameters are: 100 μm ($*$), 200 μm ($\circ$), 300 μm ($\triangle$), and 400 μm ($\square$).

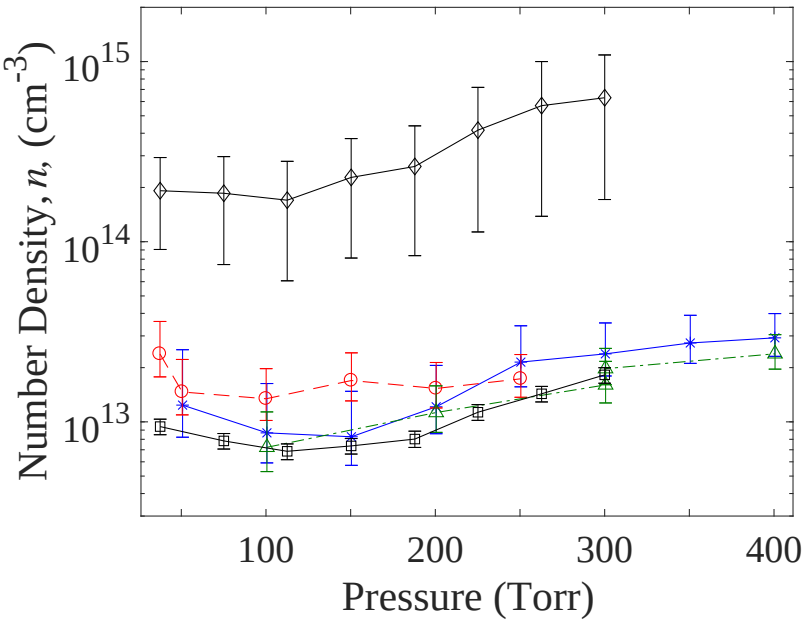

Figure 27. Calculated number density from a ($*$) 100 μm and ($\circ$) 200 μm diameter MHCD, both with a 127 μm thick dielectric and a ($\triangle$) 300 μm hole, 254 μm thick dielectric MHCD. The data in black are the number densities determined by Penache et al. using a 50 μm thick dielectric and 300 μm hole diameter [28, 29].

imum and minimum number densities relating to the minimum and maximum path lengths respectively. The marker is the number density calculated using the average path length. The three cases shown show similarities in magnitude and tendencies to the work first reported by Penache (□), which increases with pressure after an initial slight decrease. The discharge used in the previous work consisted of a 300 μm diameter hole with 130 μm thick copper electrodes separated by 50 μm of Kapton [29]. Number densities reported later (◊) are even more favorable, as they are an order of magnitude higher, ranging from 1.7×10^{14} to 6.3×10^{14} cm^{-3} [28]. The discharges were manufactured using photolithographic patterning and chemical etching on both sides. The chemical etching process produces precise cylindrical holes without the jagged edges or burning that the laser drilling process produces. It is believed that improvements to the discharge manufacturing process from laser drilling to chemical etching will produce more consistent and precise holes with greater reliability and longevity, that will also significantly increase the metastable density.

V. Optical Emission Spectroscopy and Rare Gas Model

5.1 Introduction

Models are beneficial to laser development due to the ability to determine and characterize laser performance quicker than by experiments alone. For rare gas lasers, models have been developed for both the discharge [6, 20, 21, 18] and laser [5, 7, 34, 42] operation along with experiments to validate the results. Here, a previously developed [8] five-level model, adapted from an established three-level DPAL model [12, 13], is used to determine the laser performance of a MHCD with a 254 μm gap and 100 μm diameter hole. The model combines results from experimental data to determine electron density and temperature, longitudinally averaged pump intensity, and the gain. This chapter will give an overview of the model, the experiment and analysis to collect the required data, and the model results using the experimental data.

5.2 Model Description

The five levels used in the model are the $1s_5$, $1s_4$, $2p_{10}$, $2p_9$, and $2p_8$. The kinetic processes considered in the model are electron impact production, electron impact spin-orbit mixing, argon spin-orbit mixing, argon quenching, quenching by impurities, radiative decay, pump excitation, and stimulated emission. Figure 28 shows the Ar energy level diagram and the transitions where each process occurs. For use in the model the states are numbered 1-5 from lowest to highest energy ($1s_5$-$2p_8$) and the ground state is numbered 0. The populations of the states are then represented by n_i, with i being the numbered state. Variables for transitions use a subscript ij, which represents the transition from state i to state j.

The electron impact production is the excitation of argon atoms from the ground state due to electron impact. Electron impact spin-orbit mixing is the collisions

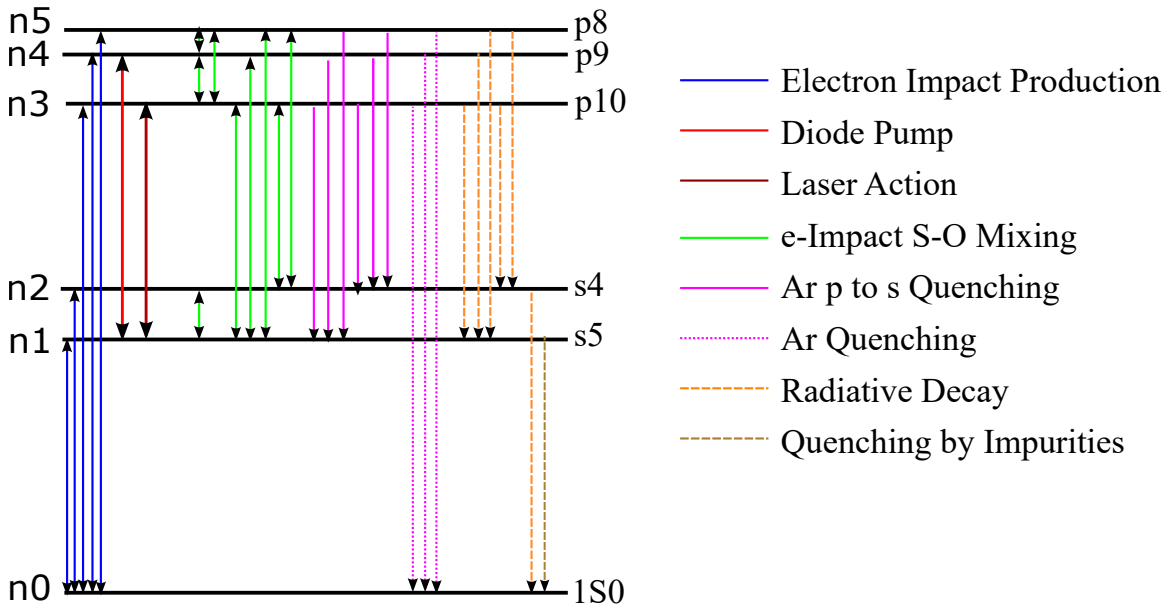

Figure 28. Energy levels and the kinetic processes for each transition used in the model [7].

between electrons and excited Ar atoms transferring energy either to or from the atoms, causing a change in energy state. The rate coefficients, γ, for the electron impact processes are shown in Table 1. The reverse process rate coefficients for spin-orbit mixing are calculated using the principle of detailed balancing,

$$\gamma_{ji} = \gamma_{ij} \frac{g_i}{g_j} \exp\left(-\frac{\Delta E}{k_B T_e}\right), \tag{17}$$

where $g_{i,j}$ is the degeneracy of the respective state, ΔE is the energy of the transition and T_e is the electron temperature.

The rate coefficients for neutral collision spin-orbit mixing and quenching are given in Table 2. The quenching rate of the 1s states is unknown and it is assumed that the $1s_5$ quenching rate is equal to the maximum rate of the 2p levels. The $1s_4$ quenching rate is incorporated into an adjusted radiative rate of 5.7×10^5 s^{-1} that primarily accounts for radiation trapping [8]. The other radiative rates used in the model are all taken from NIST and are listed in Table 3.

Table 1. Rate coefficients for electron impact production and spin-orbit mixing.

Process	Rate Coefficient (10^{-9} cm^3/s)	Ref.
$Ar(1S_0) + e^- \rightarrow Ar(1s_5) + e^-$	$2.7\exp(-11.9/T_e)$	[43]
$Ar(1S_0) + e^- \rightarrow Ar(1s_4) + e^-$	$3.5\exp(-12.3/T_e)$	[43]
$Ar(1S_0) + e^- \rightarrow Ar(2p_{10}) + e^-$	$2.0\exp(-13.0/T_e)$	[43]
$Ar(1S_0) + e^- \rightarrow Ar(2p_9) + e^-$	$1.9\exp(-13.5/T_e)$	[43]
$Ar(1S_0) + e^- \rightarrow Ar(2p_8) + e^-$	$2.2\exp(-13.6/T_e)$	[43]
$Ar(1s_5) + e^- \rightarrow Ar(2p_{10}) + e^-$	$300\exp(-2/T_e)$	[43]
$Ar(1s_4) + e^- \rightarrow Ar(2p_{10}) + e^-$	$150\exp(-2/T_e)$	[43]
$Ar(1s_5) + e^- \rightarrow Ar(2p_9) + e^-$	$600\exp(-2/T_e)$	[43]
$Ar(1s_5) + e^- \rightarrow Ar(2p_8) + e^-$	$100\exp(-2/T_e)$	[43]
$Ar(1s_4) + e^- \rightarrow Ar(2p_8) + e^-$	$400\exp(-2/T_e)$	[43]
$Ar(2p_8) + e^- \rightarrow Ar(2p_9) + e^-$	$400T_e^{-0.6}$	[43]
$Ar(2p_8) + e^- \rightarrow Ar(2p_{10}) + e^-$	$400T_e^{-0.6}$	[43]
$Ar(2p_9) + e^- \rightarrow Ar(2p_{10}) + e^-$	$400T_e^{-0.6}$	[43]
$Ar(1s_5) + e^- \rightarrow Ar(1s_4) + e^-$	$100T_e^{-0.6}$	[43]

Table 2. Rate coefficients for Ar-Ar spin-orbit mixing and quenching.

Process	Rate Coefficient (10^{-11} cm^3/s)	Ref.
$Ar(2p_{10}) + Ar \rightarrow Ar(1s_5) + Ar$	$0.375\,(T/300)^{0.5}$	[43]
$Ar(2p_{10}) + Ar \rightarrow Ar(1s_4) + Ar$	$0.375\,(T/300)^{0.5}$	[43]
$Ar(2p_9) + Ar \rightarrow Ar(1s_5) + Ar$	$0.75\,(T/300)^{0.5}$	[43]
$Ar(2p_9) + Ar \rightarrow Ar(1s_4) + Ar$	$0.75\,(T/300)^{0.5}$	[43]
$Ar(2p_8) + Ar \rightarrow Ar(1s_5) + Ar$	$1.0\,(T/300)^{0.5}$	[43]
$Ar(2p_8) + Ar \rightarrow Ar(1s_4) + Ar$	$1.0\,(T/300)^{0.5}$	[43]
$Ar(2p_8) + Ar \rightarrow Ar(2p_9) + Ar$	$1.1\,(T/300)^{0.5}$	[17]
$Ar(2p_8) + Ar \rightarrow Ar(2p_{10}) + Ar$	$1.1\,(T/300)^{0.5}$	[17]
$Ar(2p_9) + Ar \rightarrow Ar(2p_{10}) + Ar$	$2.6\,(T/300)^{0.5}$	[17]
$Ar(2p_8) + Ar \rightarrow Ar(1S_0) + Ar$	$1.5\,(T/300)^{0.5}$	[17]
$Ar(2p_9) + Ar \rightarrow Ar(1S_0) + Ar$	$2.5\,(T/300)^{0.5}$	[17]
$Ar(2p_{10}) + Ar \rightarrow Ar(1S_0) + Ar$	$0.59\,(T/300)^{0.5}$	[17]

Table 3. Einstein A coefficients used in the Rg model [22].

Process	Einstein A coefficient (10^7 s^{-1})
$Ar(2p_8) \rightarrow Ar(1s_4)$	2.15
$Ar(2p_8) \rightarrow Ar(1s_5)$	0.928
$Ar(2p_9) \rightarrow Ar(1s_5)$	3.31
$Ar(2p_{10}) \rightarrow Ar(1s_4)$	0.543
$Ar(2p_{10}) \rightarrow Ar(1s_5)$	1.89

The population rate equations solved by the model are

$$\begin{aligned}
\frac{dn_1}{dt} = 0 = {} & k_{01}^e n_{Ar} + \frac{\Omega\sigma_{41}(\nu)}{h\nu}\left(n_4 - \frac{g_4}{g_1}n_1\right) + k_{21}^{Ar} n_2 + \left(\Gamma_{31} + k_{31}^{Ar}\right) n_3 \\
& + \left(\Gamma_{41} + k_{41}^{Ar}\right) n_4 + \left(\Gamma_{51} + k_{51}^{Ar}\right) n_5 \\
& - \left(k_{10}^e + k_{12}^{Ar} + k_{13}^{Ar} + k_{14}^{Ar} + k_{15}^{Ar} + k_{q,1}\right) n_1 \qquad (18) \\
\frac{dn_2}{dt} = 0 = {} & k_{02}^e n_{Ar} + k_{12}^{Ar} n_1 + \left(\Gamma_{32} + k_{32}^{Ar}\right) n_3 + k_{42}^{Ar} n_4 + \left(\Gamma_{52} + k_{52}^{Ar}\right) n_5 \\
& - \left(k_{20}^e + \Gamma_{20} + k_{21}^{Ar} + k_{23}^{Ar} + k_{24}^{Ar} + k_{25}^{Ar}\right) n_2 \qquad (19) \\
\frac{dn_3}{dt} = 0 = {} & k_{03}^e n_{Ar} + k_{13}^{Ar} n_1 + k_{23}^{Ar} n_2 + k_{43}^{Ar} n_4 + k_{53}^{Ar} n_5 - \left(k_{30}^e + \Gamma_{31} + \Gamma_{32}\right) n_3 \\
& - \left(k_{31}^{Ar} + k_{32}^{Ar} + k_{34}^{Ar} + k_{35}^{Ar} + k_{q,3}\right) n_3 \qquad (20) \\
\frac{dn_4}{dt} = 0 = {} & k_{04}^e n_{Ar} - \frac{\Omega\sigma_{41}(\nu)}{h\nu}\left(n_4 - \frac{g_4}{g_1}n_1\right) + k_{14}^{Ar} n_1 + k_{24}^{Ar} n_2 + k_{34}^{Ar} n_3 + k_{54}^{Ar} n_5 \\
& - \left(k_{40}^e + \Gamma_{41}\right) n_4 - \left(k_{41}^{Ar} + k_{42}^{Ar} + k_{43}^{Ar} + k_{45}^{Ar} + k_{q,4}\right) n_4 \qquad (21) \\
\frac{dn_5}{dt} = 0 = {} & k_{05}^e n_{Ar} + k_{15}^{Ar} n_1 + k_{25}^{Ar} n_2 + k_{35}^{Ar} n_3 + k_{45}^{Ar} n_4 - \left(k_{50}^e + \Gamma_{51} + \Gamma_{52}\right) n_5 \\
& - \left(k_{51}^{Ar} + k_{52}^{Ar} + k_{53}^{Ar} + k_{54}^{Ar} + k_{q,5}\right) n_5, \qquad (22)
\end{aligned}$$

where $k_{ij}^M = \gamma_{ij}^M n_M$ is the frequency of energy transfer from state i to j by collisions with species M, which is either e or Ar, Γ_{ji} is the radiative rate from j to i, $k_{q,i}$ is the quenching of the ith state, and Ω is the longitudinally averaged pump intensity. The pump makes two passes through the cavity as in Hager et al [13]. The longitudinally

averaged pump intensity is described by the transcendental equation

$$\Omega = \frac{I_p}{l_g}\left(\int_{-\infty}^{\infty} f_p(\nu)\exp\left(\sigma_{41}(\nu)\left(n_4(\Omega) - \frac{g_4}{g_1}n_1(\Omega)\right)2l_g\right)\,\mathrm{d}\nu - 1\right), \tag{23}$$

where I_p is the input pump intensity, l_g is the gain length, $f_p(\nu)$ is the pump laser line shape (Gaussian), and σ_{41} is the stimulated emission cross section of the pump transition.

By solving Equations (18-22) the state populations are determined as functions of the electron density, electron temperature, gas temperature, and longitudinally averaged pump intensity. Experimental results of the $1s_5$ population, gas temperature, and population ratios are used to estimate the electron density and temperature and then Equation (23) can be solved numerically to relate the longitudinally averaged pump intensity Ω to the input pump intensity I_p. The results are used to predict the gain of the system.

5.3 Experiment

The gas temperature and $1s_5$ population were determined by TDLAS as mentioned in sections 4.4 and 4.6, respectively. The population ratios were determined using optical emission spectroscopy (OES), as will be described below.

Setup and Collection.

The argon spectra was collected using a Pi-Max 4 1024×1024 ICCD on the end of a McPherson 1.3 m Monochromator with a 1800 gr/mm, 500 nm blaze holographic grating. The fiber coupler was placed just outside the vacuum chamber window approximately 3.5 in from the discharge, viewing it end on. Images were taken of four spectral regions of interest, three of which contained two spectral lines. Multiple spec-

tral lines allow for simple calibration of the dispersion, and therefore, the wavelength of the x-axis by using the known wavelengths of each of the lines. The wavelengths and the corresponding transitions are shown in Table 4, with horizontal lines separating the regions corresponding to the four monochromator positions used. Integration times of 1, 5, 10, 25, 50, and 100 ms were used and 10 images were taken with each integration time and position.

The discharge used for the spectra data collection was a 254 μm gap and 100 μm diameter hole. The pure argon gas pressure was varied from 100-400 Torr, in 100 Torr increments. Data for 100-300 Torr was collected while the discharge operated continuously with an applied voltage of 320 V, a sustaining voltage between 155-160 V and a current of 1.7 mA. The discharge went out while collecting data at 400 Torr, and after relighting the plasma the applied voltage was set to 400 V for stable operation. The sustaining voltage remained at 159 V which meant the current increased to 2.5 mA. Data at 400 Torr was collected with the higher current but the discharge went out before collecting images at 25-100 ms integration times for the last position (912 nm line). The detector is less sensitive in this region so longer integration times are desirable to increase the SNR. Because the integration time was 10 times shorter than at other pressures, the SNR is significantly lower.

Table 4. Argon spectral lines used for OES.

Wavelength (nm)	Transition	A_{ji} (s^{-1})	E_i (cm^{-1})	E_j (cm^{-1})	g_i	g_j
800.8359	$1s_4 \rightarrow 2p_6$	4.90×10^6	93,750.5978	106,237.5518	3	5
801.6990	$1s_5 \rightarrow 2p_8$	9.28×10^6	93,143.7600	105,617.2700	5	5
810.5921	$1s_4 \rightarrow 2p_7$	2.50×10^7	93,750.5978	106,087.2598	3	3
811.7542	$1s_5 \rightarrow 2p_9$	3.31×10^7	93,143.7600	105,462.7596	5	7
841.0521	$1s_2 \rightarrow 2p_3$	2.23×10^7	95,399.8276	107,289.7001	3	5
842.6963	$1s_4 \rightarrow 2p_8$	2.15×10^7	93,750.5978	105,617.2700	3	5
912.5471	$1s_5 \rightarrow 2p_{10}$	1.89×10^7	93,143.7600	104,102.0990	5	3

Analysis.

The longest integration time without saturating was used for each respective region, and the 10 images taken with that time were averaged together and the background was subtracted. For the 912 nm line at 400 Torr only five of the ten images were used because the discharge went out. The pixel pitch for the first three regions were determined from the known distance between spectral lines. The pixel pitch decreased from 3.31 to 3.09 pm/pixel as the wavelength region increased from around 801 to 841 nm. The decrease is expected because angular dispersion is greater for shorter wavelengths. It was assumed that the decrease in pixel pitch would continue linearly, and the pixel pitch around 912 nm was extrapolated to be 2.63 pm/pixel.

Calibrating the intensity was done by taking images of an Oriel tungsten lamp with a known emission profile. The know emission was compared to the measured emission, taking into account the collection aperture, to obtain the conversion for the raw data into a power measurement. The integration times used for the tungsten lamp were the same as the MHCD so adjustments for integration time were not required. Once both axes were calibrated the spectral lines were fit using the same method as in section 4.3.

Unlike the absorbance data from TDLAS, the emission spectra must be fit to a Voigt function even at higher pressures because the instrument line width is significant and has the form of a Gaussian. The instrument line width was determined by using Ar, Hg-Ar, and Kr pen lamps to measure spectral lines in the same four regions data was collected. The pixel pitch for each region was consistent with the MHCD discharge data. The pixel pitch was used to convert the line width from pixels to nm which was then converted to frequency. On average the instrument line width was 7.3 GHz. The instrument line width was set as the lower bound for the Doppler width parameter for the Voigt fits. Figure 29 shows the 801.6990 nm spectral line data (red

points), the Voigt fit (blue line) and the residuals. There was no baseline problem like in section 4.3, but there was difficulty in obtaining a good fit due to under sampling of the data in the line core. Figure 30 shows all four pressures for the 841.0521 nm line increasing in pressures from darkest to lightest. All other lines are provided in Appendix E. As expected the line broadens, but at 400 Torr the magnitude increases. The increase was consistent for all spectral lines and is likely due to the increase in current after the discharge was relit.

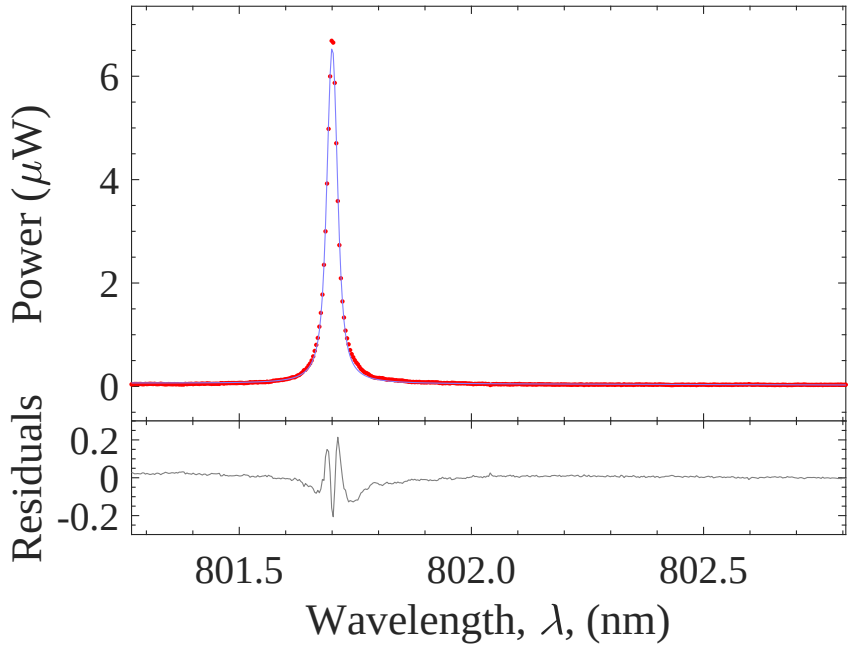

Figure 29. Argon 801.6990 nm spectral line data collected using OES at 400 Torr. Data (red points) is fit with a Voigt function (blue line), and residuals are shown underneath.

The area of the line shapes is used to calculate the population ratios. Because an area normalized Voigt function was used for the fit, the area of the line shape is equal to the amplitude from the fit. Figure 31 shows the relative populations of the 2p states measured ($2p_{10}$, $2p_9$, $2p_8$, $2p_7$, $2p_6$, and $2p_3$) at 100-400 Torr. The plots are known as Boltzmann plots and the lack of any linear relationship indicate the plasma was not in local thermodynamic equilibrium. The relative populations used in the

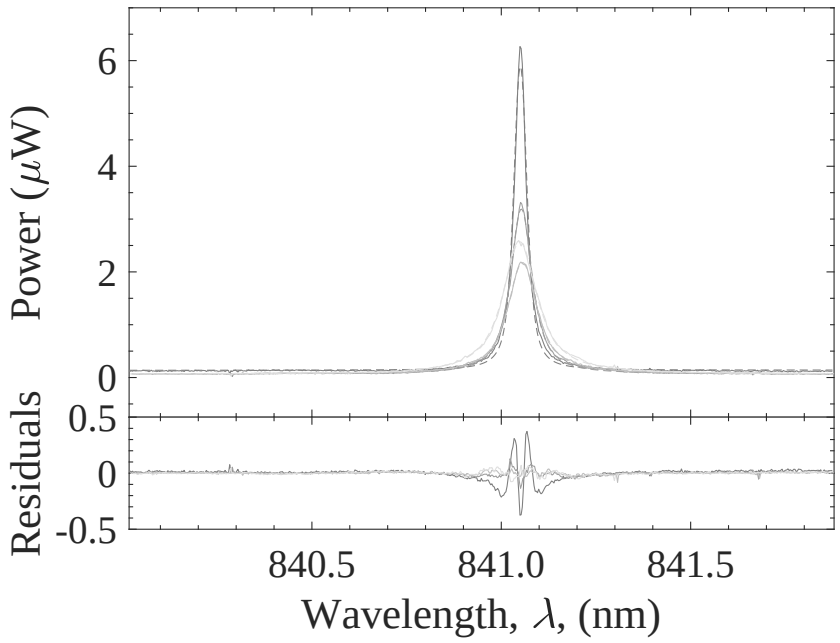

Figure 30. Argon 841.0521 nm spectral line data collected using OES. Data(–), Voigt fits(- -) and residuals are shown for pressures of 100-400 Torr from darkest to lightest.

model are given by the argument of the natural log function from the Boltzmann plot,

$$\text{Relative Population} = \frac{Area\ \lambda_{ji}}{A_{ji}\ g_j}. \tag{24}$$

The uncertainty in the populations is mostly due to the large uncertainty ($\pm 25\%$) in the A coefficients.

5.4 Results

The population ratios p_{10}/p_9 and p_{10}/p_8 were calculated using the respective relative populations given by Equation 24. The measured ratios are then compared to the ratios predicted by the model, and a recursive process is used to determine the electron density and temperature. Using an initial estimate for the electron temperature, the measured gas temperature (500 K), and assuming no pump, the ratios can be plotted as functions of the electron density. Figure 32 shows the model pre-

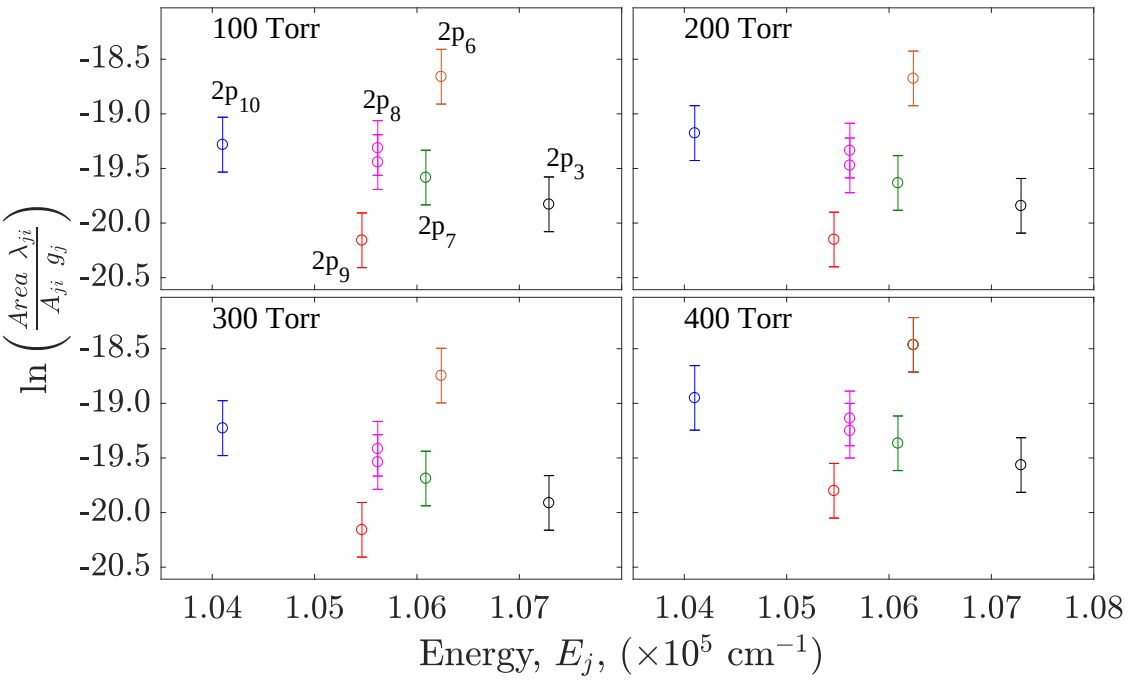

Figure 31. Boltzmann plots for Ar plasma obtained from Ar I lines. The scatter in the data indicates the plasma was not in local thermodynamic equilibrium.

dicted population ratios for p_{10}/p_9 (red) and p_{10}/p_8 (blue), and the measured values (dashed lines) with uncertainty (dotted lines) at 100 Torr. The left and right vertical gray lines mark the approximate intersections of the predicted and measured ratios. Ideally the intersections would be near the same electron density, and that would indicate what the electron density was. Unfortunately the p_{10}/p_8 ratio is lower than the p_{10}/p_9 which is opposite of what the model predicts. Most of the rates used in the model were determined experimentally at electron energies much higher (1-2 orders of magnitude) than in this work. The rates may not be accurate at lower energies and could be the cause of the discrepancy in the data. As a result of the discrepancy, the intersections of the predicted and measured ratios occur at electron densities that are over an order of magnitude apart. Even when the uncertainties are considered there is not a common electron density for the ratios. As a result the electron density

is estimated to be approximately half way between the intersections of the respective upper or lower uncertainties and the predicted curves, marked by the center gray line in Figure 32.

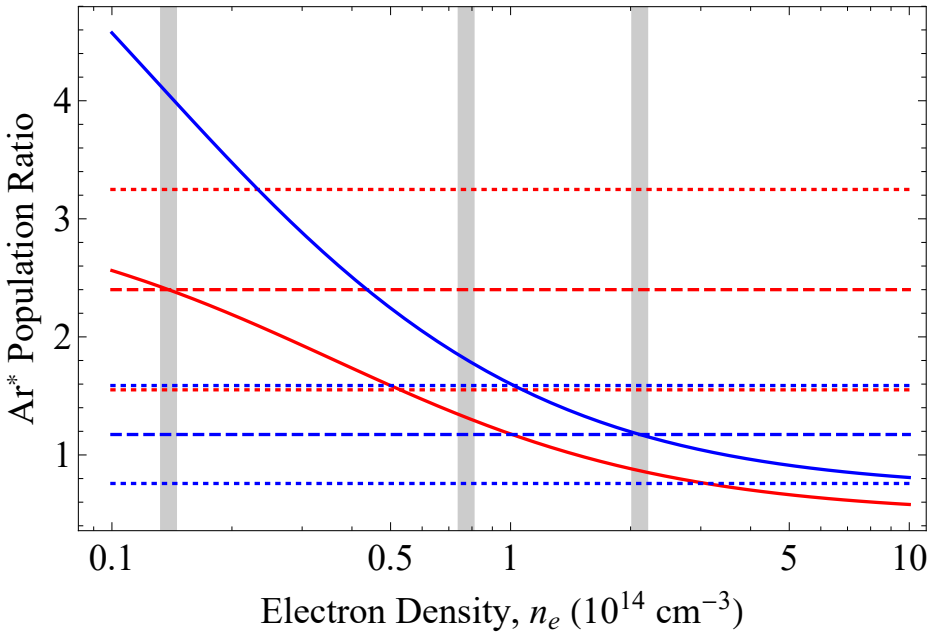

Figure 32. Predicted p_{10}/p_9 (red line) and p_{10}/p_8 (blue line) population ratios at 100 Torr. Measured values are indicated by dashed lines with the uncertainty marked by dotted lines. The left and right vertical gray lines mark the approximate intersections of the measured and predicted values. Because the intersections correspond to different electron densities the center gray line marks the estimated electron density used for calculations.

The initial estimate for the electron temperature was checked by comparing the measured Ar $1s_5$ density and predicted density calculated using the estimated electron density. The predicted Ar $1s_5$ density can then be plotted as a function of the electron temperature as shown in Figure 33. The measured density is shown with the dashed line and the gray line is the electron temperature found by where the measured and predicted densities are equal. The new electron temperature was then used to calculate the electron density again. Usually two iterations were all that was required. The results for the electron density and temperature for all pressures is shown in Table 5. The electron density increased steadily with pressure, and was nearly four

times higher at 400 Torr than 100 Torr.

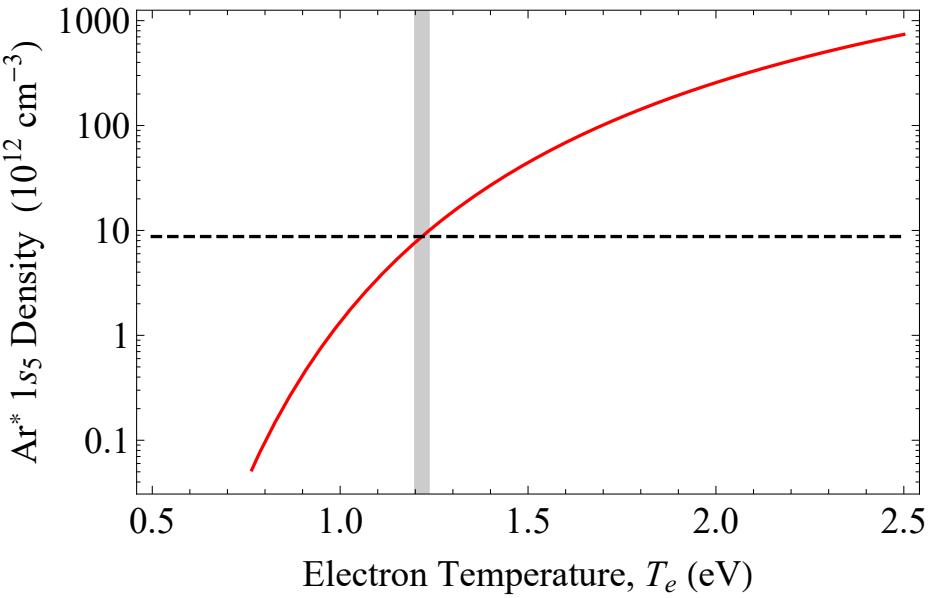

Figure 33. Predicted (solid red line) and measured (dashed black line) $1s_5$ number density at 100 Torr. The intersection, marked by the vertical gray line indicates the estimated electron temperature.

With the electron density, electron temperature, and gas temperature known, the state populations in the model become functions of the longitudinally averaged pump intensity only. Equation (23) was then solved numerically for the longitudinally averaged pump intensity as a function of the input pump intensity. The gain, G, is also calculated from

$$G(\Omega) = \sigma_{31}\left(n_3(\Omega) - \frac{g_3}{g_1}n_1(\Omega)\right), \tag{25}$$

Table 5. Predicted electron density and electron temperature for a MHCD with a gas temperature of 500 K.

Pressure (Torr)	Electron Density n_e (10^{14} cm^{-3})	Electron Temperature T_e (eV)
100	0.74	1.22
200	1.2	1.17
300	1.9	1.14
400	2.9	1.11

and the results for all pressures are shown in Figure 34. The dashed line is the gain threshold described by

$$G_{th} = -\frac{\ln(rt^4)}{2l_g}, \tag{26}$$

where r is the output coupler reflectivity and t is the transmission through the cell windows. For the model $r = 0.9$, $t = 0.99$ and $l_g = 327$ μm. The gain decreases as the pressure increases and for the laser cavity parameters used, threshold isn't achieved at any pressure. In order to reach threshold with the current cavity parameters a $1s_5$ density of around 7×10^{13} cm^{-3} would be required. The gain for this density is shown in Figure 34 with the red dashed line.

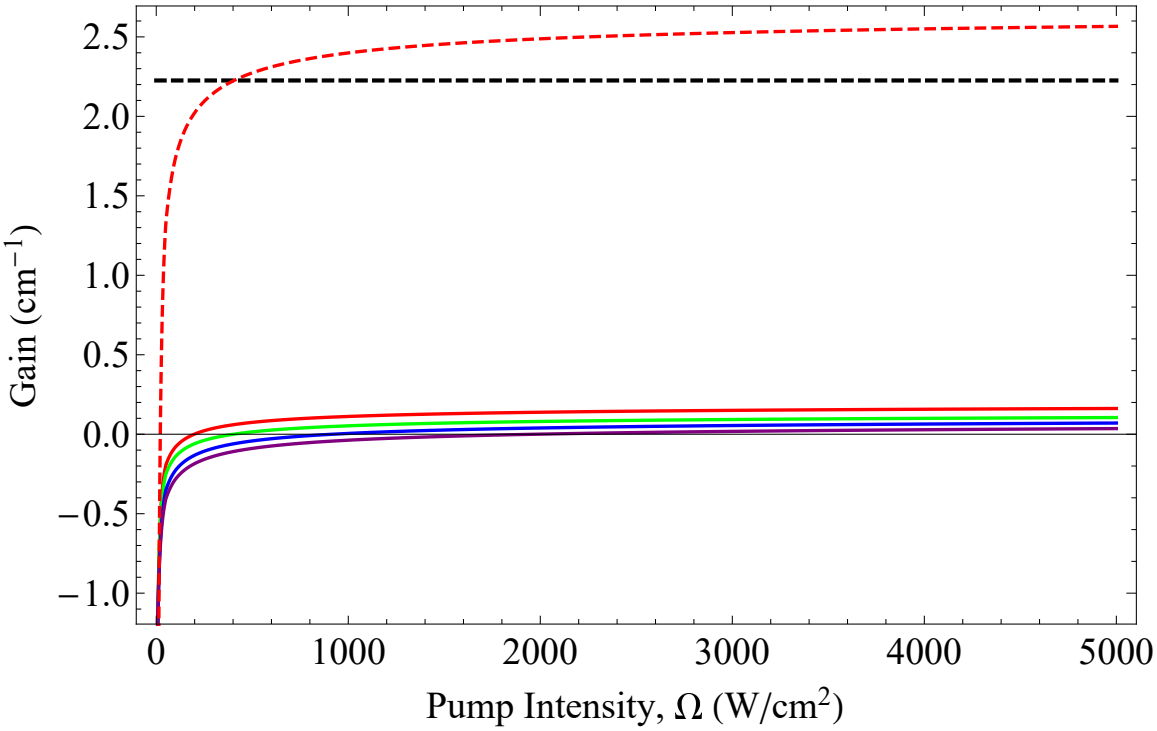

Figure 34. Predicted gain at 100 (red), 200 (green), 300 (blue), and 400 (purple) Torr as a function of the longitudinally averaged pump intensity for a 254 μm thick dielectric and 100 μm hole diameter plate. The corresponding measured Ar $1s_5$ number densities were 0.87×10^{13}, 1.07×10^{13}, 1.28×10^{13}, and 1.33×10^{13} cm^{-3}. Threshold is marked by the black dashed line. The red dashed line shows what the gain to reach threshold, which would require a number density of 7×10^{13} cm^{-3} at 100 Torr.

VI. Conclusions

6.1 Tunable Diode Laser Absorption Spectroscopy

The number density of the argon $1s_5$ state was measured in microhollow cathode discharges with hole diameters ranging from 100-400 μm and electrode gaps of 127 and 254 μm. The number densities were found to be in the range of $0.5 - 2.0 \times 10^{13}$. There were no clear trends with pressure or gap distance. The 400 μm diameter holes were consistently lower than other diameters, but no other relationship could be made between the other hole diameters. There are large uncertainties in the number densities resulting from the inability to accurately determine the absorbance path length due to instabilities in the plasma formation and imaging method. The instabilities are likely due to imperfections on the electrode plate surface and damage to the hole as the discharge is operated. Similar discharge configurations were also found to be inconsistent with each other, and there was a large variation in the lifetime of the discharges. Although the excited number densities are sufficient for laser operation, the current reliability and consistency issues will prevent the MHCD from being used in rare gas lasers.

6.2 Optical Emission Spectroscopy and Rare Gas Model

OES was used to measure the relative populations of the $2p_{10}$, $2p_9$, $2p_8$, $2p_7$, $2p_6$, and $2p_3$ states from 100-400 Torr. The results indicated the plasma was not in local thermodynamic equilibrium. The population ratios $2p_{10}/2p_9$ and $2p_{10}/2p_8$ were used in a five level laser model to predict an electron density that increased with pressure from $0.74 - 2.9 \times 10^{14}$ cm^{-3} and an electron temperature that decreased with pressure from 1.22-1.11 eV. The gain was predicted to decrease with pressure and was over an order of magnitude lower than threshold. At 100 Torr, a number density

of approximately 7×10^{13} cm^{-3} is required to reach threshold due to the short gain length.

6.3 Future Work

In future work, improvements should be made in manufacturing the discharges. Using a wet etching process would allow for more precise control of hole sizes, without leaving jagged edges or burn marks. Having more precise holes that are identical from plate to plate should provide more consistent results which would assist in determining the reliability of MHCD operation for Rg lasers. Research into the optimal electrode and insulator materials should also be performed. Copper is very susceptible to sputtering and a less susceptible material, such as tungsten, tantalum or molybdenum would increase the plate lifetime. Ceramic materials such as alumina or macor as the insulator would also be more resistive against damage.

Because DPRGLs require volumes around six orders of magnitude larger than the ~10^{-5} cm^3 produced in a single 100 μm to 400 μm hole, single hole microcathode structured discharges (MCSD) and microcathode structured discharge arrays (MCSDA) should be studied. A single MCSD with the extra anode placed 0.5 cm from the MHCD would increase the volume by approximately three orders of magnitude. Combining multiple holes in a MCSDA would provide means to scale to 10 cm^3 for high energy Rg lasers.

Appendix A. Microscope Images

Based on unaided eye observations, it was believed that the laser drilled holes were not all the same size, and that the holes were smaller when on one side of the plate. After operation the holes appeared to be larger and there was obvious burn marks around the hole. As a result of these observations it was desirous to get a better view of the discharge hole. Microscope images were taken of a small sample of plates to view the hole structure before and after use. Images of arrays (Figures 35-37) revealed that the hole diameters varied by up to 10 μm. The 300 μm hole imaged (Figure 38) was consisted with those discussed in section 4.2, where the front (laser drilled side) was around 10% bigger than expected and the back was around 5% smaller. The 400 μm hole (Figure 39) was unique in that the back side was also larger (by 7 μm) than expected.

Figure 40 compares the damage to two 200 μm plates. The plate in (a/b) was used for multiple (5) short interval (5-10 min) tests and the other (c/d) operated continuously for nearly two hours.

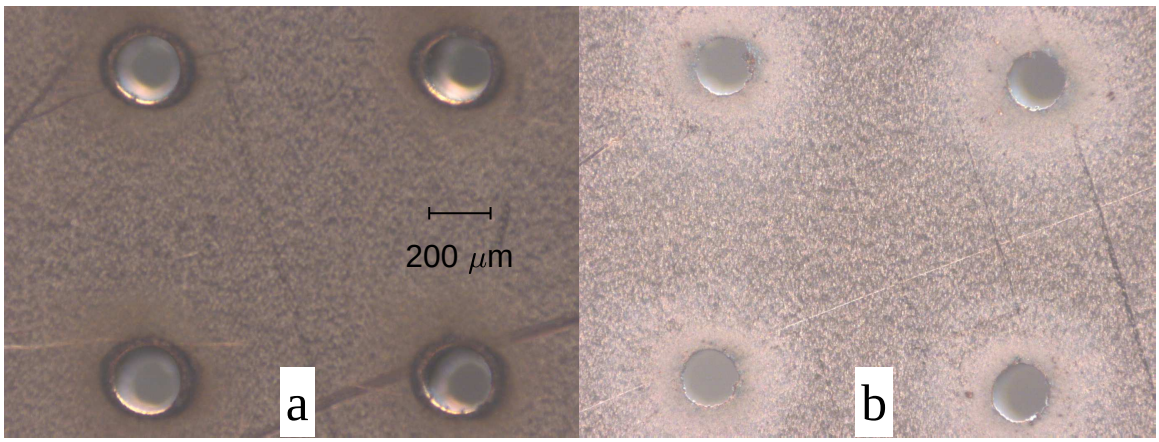

Figure 35. Images of part of an array of 200 μm diameter holes. Image (a) is the side where the laser drilling occurred. The plate was flipped so that the holes on the left of image (b) are the back of the holes on the right of image (a). The holes are noticeably non-circular in parts, and have jagged edges in the hole. Scratches in the copper surface can also be seen on both sides of the plate.

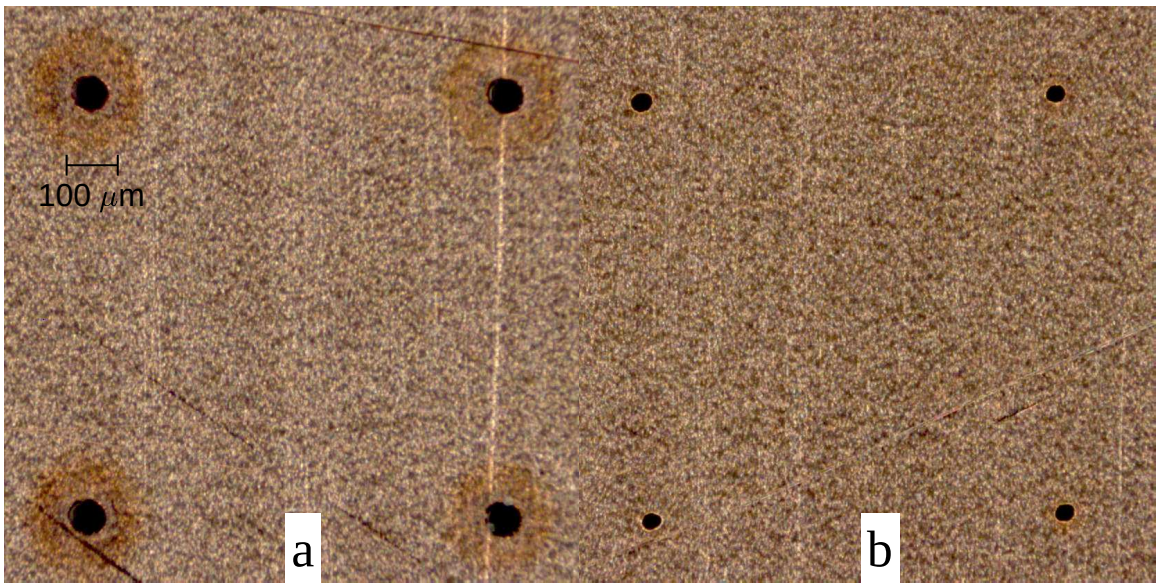

Figure 36. Images of both sides of a 50 μm 2 $\times$ 2 array before use. Image (a) is the side where the laser drilling occurred. The discoloration around the plates indicates heating during the drilling process. There are multiple scratches on both sides of the plate surface which could impact operation. The hole on the lower left in (b) is clearly non-circular. Despite the same laser drilling settings, the burn marks and hole shapes are noticeably different.

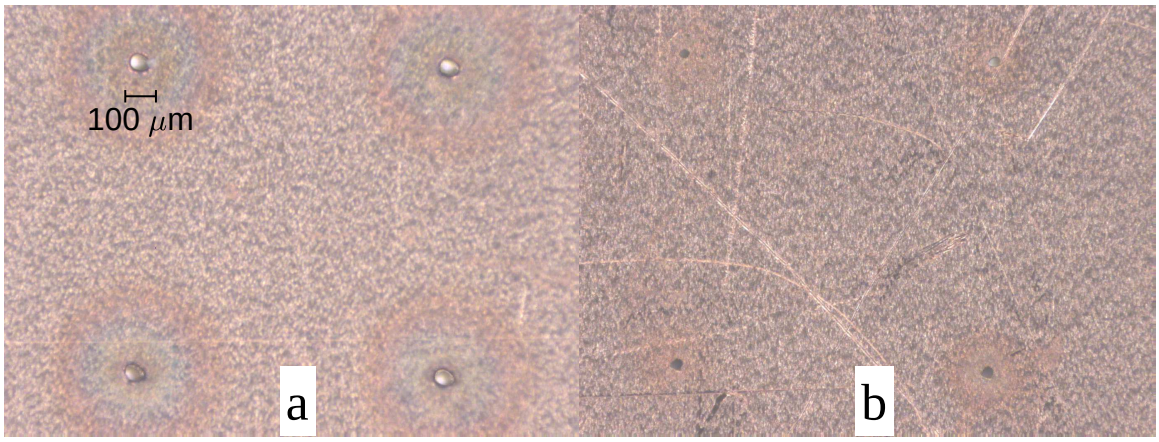

Figure 37. Images of both sides of a 50 μm array before use. Image (a) is the side where the laser drilling occurred. The discoloration around the plates indicates heating during the drilling process. The lines in the images are scratches in the copper. The plate was flipped so that the holes on the left of image (b) are the back of the holes on the right of image (a). Despite the same laser drilling settings, the burn marks and hole shapes are noticeably different.

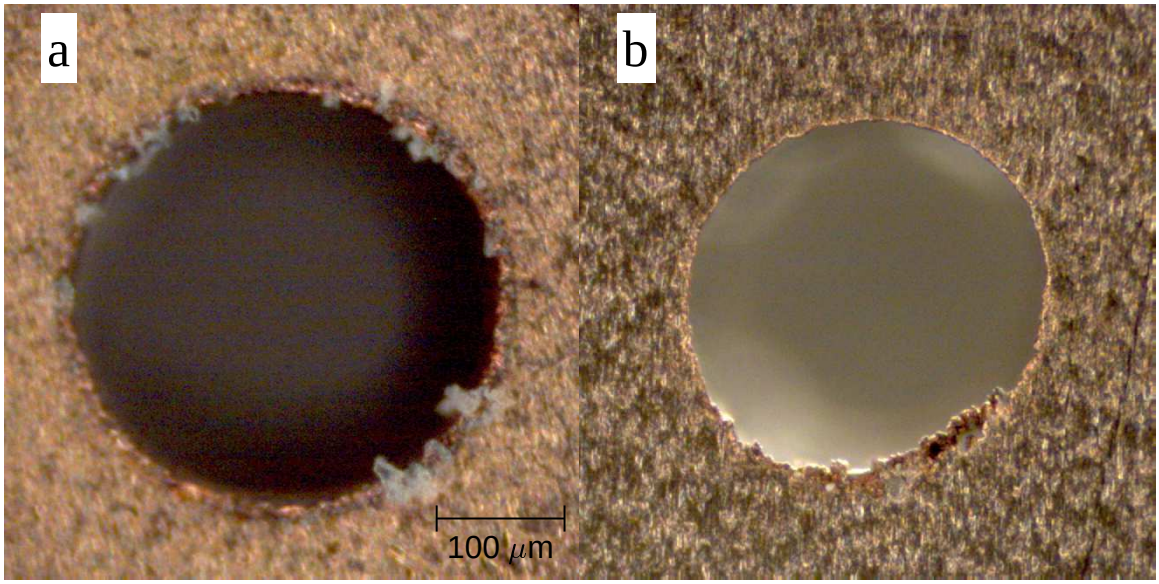

Figure 38. Images of both sides of a 300 μm diameter hole before use. Actual measured diameters were (a) 334 μm and (b) 286 μm. Image (a) is the side where the laser drilling occurred. The whitish material in (a) is the dielectric material. In the lower right of the hole in (b) there is copper that is not completely removed from the hole. Both the dielectric and copper in the hole would change the electric field and as a result have an impact on discharge operation.

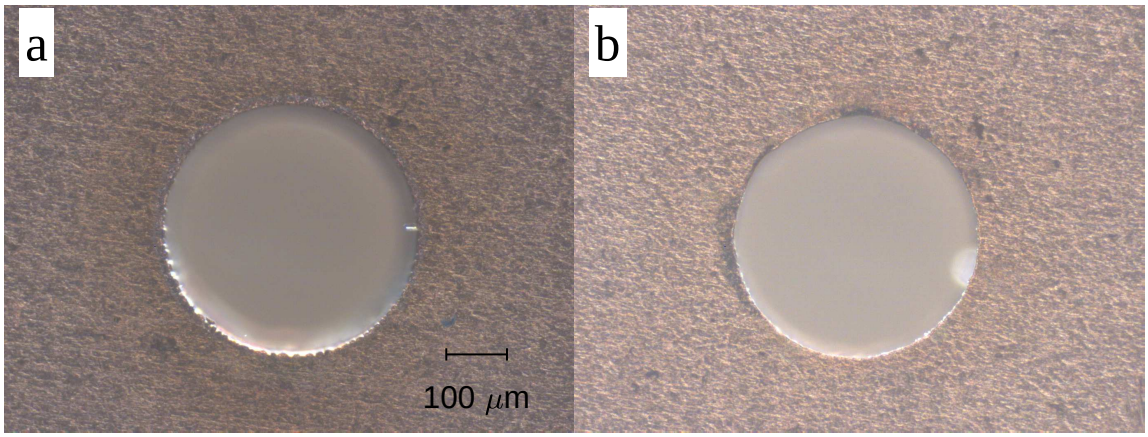

Figure 39. Images of both sides of a 400 μm hole before use. Actual measured diameters were (a) 423 μm and (b) 407 μm. Image (a) is the side where the laser drilling occurred. (a) There are no large jagged edges but the hole edge does appear to be rough, especially in the lower half. (b) The are few dark regions on the edge of the hole which appear burned.

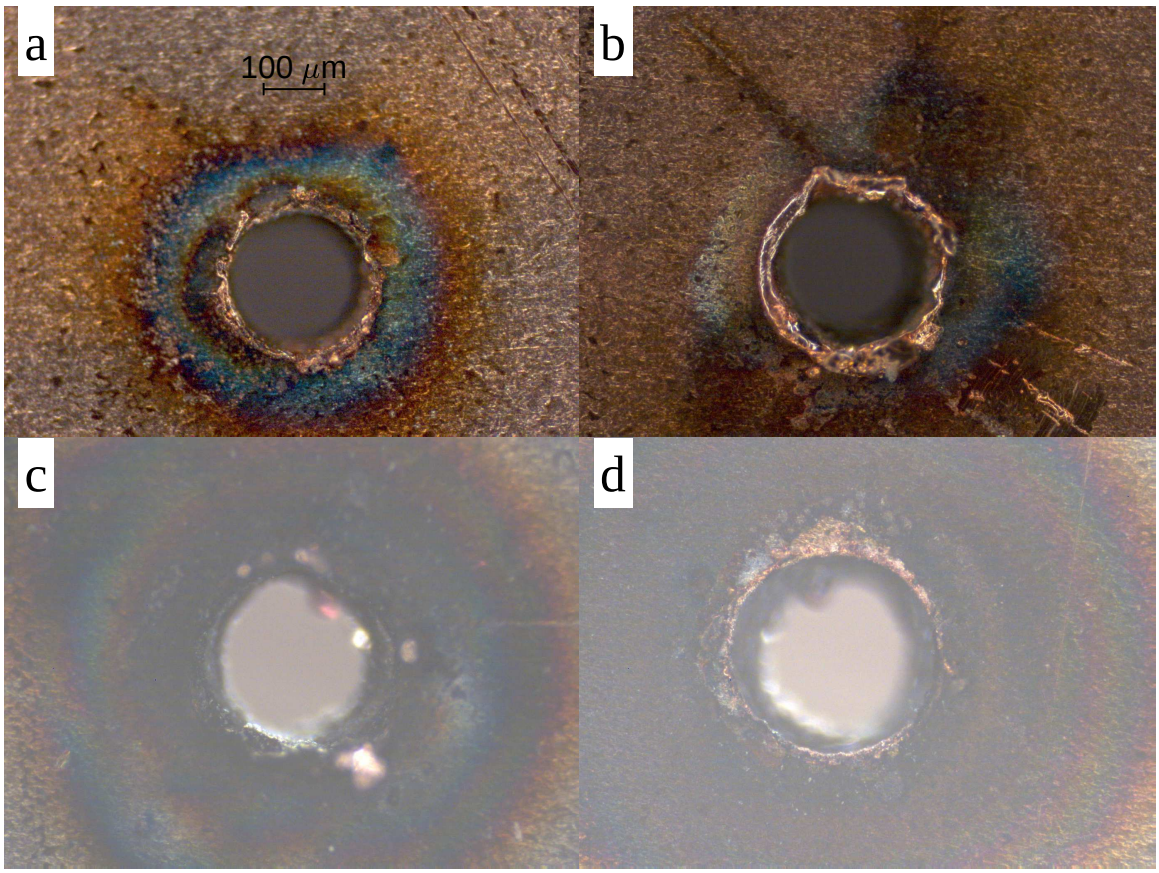

Figure 40. Images of both sides of 200 μm diameter hole plates. The plate in (a/b) was used in laser absorption and breakdown voltage measurements where the discharge was turned off between each measurement. The plate in (c/d) was used continuously for close to two hours.

Appendix B. TDLAS Line Shape Fits

The absorbance data from all MHCDs, measured with TDLAS. Each figure contains the absorbance, a fit to the data, and the residuals. The fit consists of a Lorentzian and sine function with a linear polynomial baseline. There are multiple data sets on each figure corresponding to the different pressures measured. The pressures vary for each figure based on where the discharge was able to operate and absorption could be detected. All pressures are with the range of 37-400 Torr. For the 254 μm gap plates with holes of 100 and 200 μm there are two figures because two different discharges were used to try and collect data from at least 100-400 Torr. The discharge each figure corresponds to is:

Figure 41 : 127 μm gap, 100 μm diameter hole,

Figure 42 : 127 μm gap, 300 μm diameter hole,

Figure 44 : 254 μm gap, 100 μm diameter hole, first discharge

Figure 43 : 254 μm gap, 100 μm diameter hole, second discharge

Figure 45 : 254 μm gap, 200 μm diameter hole, first discharge

Figure 46 : 254 μm gap, 200 μm diameter hole, second discharge

Figure 47 : 254 μm gap, 300 μm diameter hole,

Figure 48 : 254 μm gap, 400 μm diameter hole.

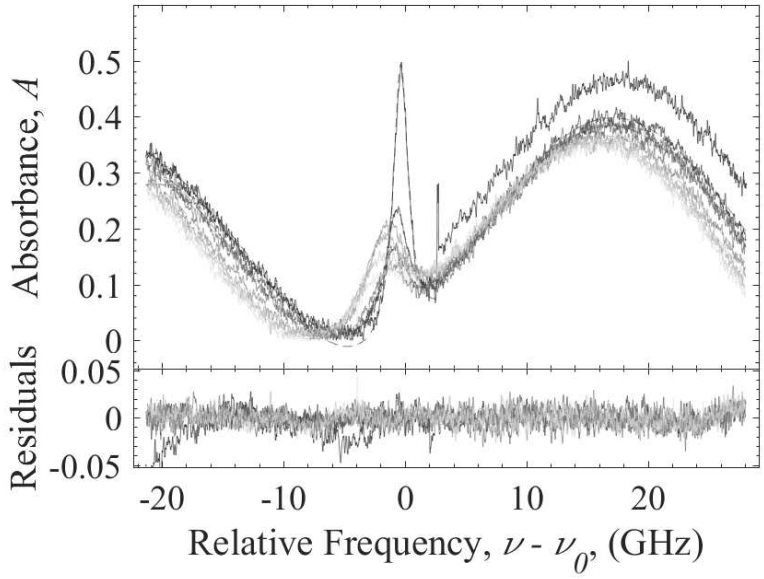

Figure 41. Absorbance data, fits, and residuals for a MHCD with a 127 μm thick dielectric and 100 μm hole diameter. The pressures ranges from 50-400 Torr in 50 Torr increments from darkest to lightest. A Lorentzian and sine function with a linear baseline were fit concurrently.

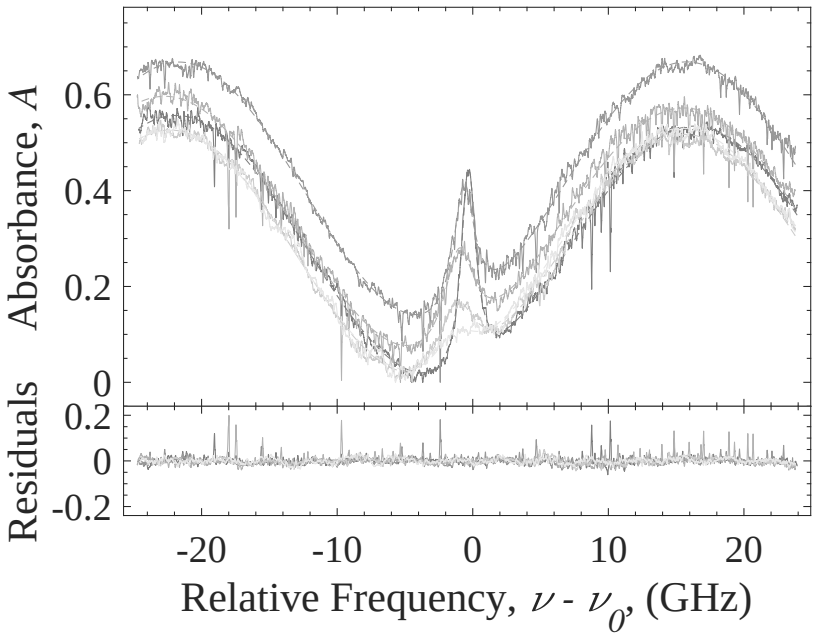

Figure 42. Absorbance data, fits, and residuals for a MHCD with a 127 μm thick dielectric and 300 μm hole diameter. The pressures ranges from 50-250 Torr in 50 Torr increments from darkest to lightest. A Lorentzian and sine function with a linear baseline were fit concurrently. It is not know what caused the random spikes in the data, which were not present for any other scans.

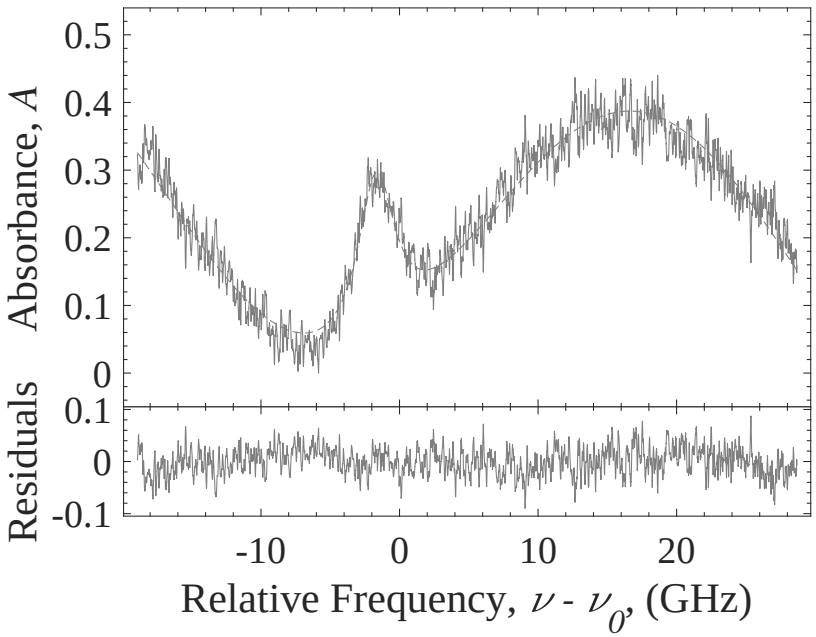

Figure 43. Absorbance data, fit, and residuals for a MHCD with a 254 μm thick dielectric and 100 μm hole diameter. The pressure was 300 Torr. A Lorentzian and sine function with a linear baseline were fit concurrently.

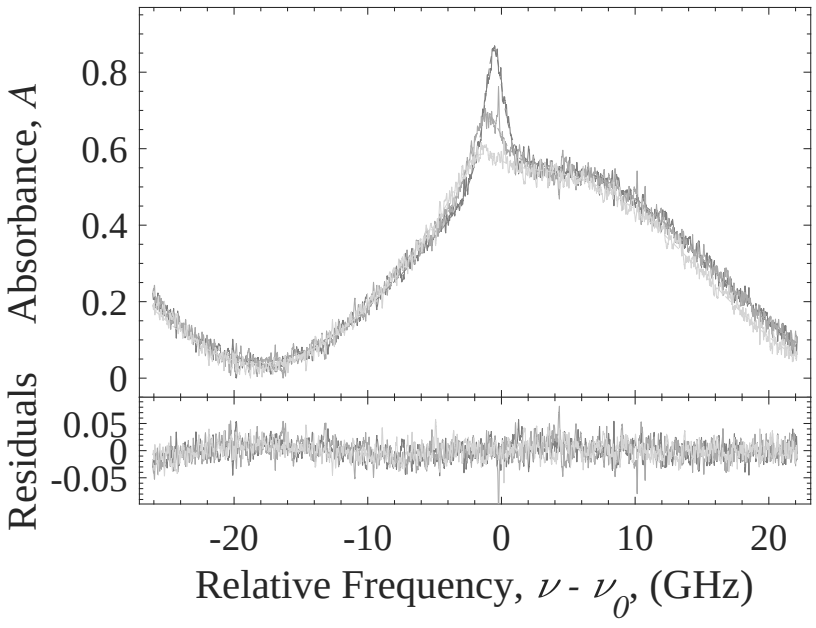

Figure 44. Absorbance data, fits, and residuals for a MHCD with a 254 μm thick dielectric and 100 μm hole diameter. The pressures ranges from 100-300 Torr in 100 Torr increments from darkest to lightest. A Lorentzian and sine function with a linear baseline were fit concurrently.

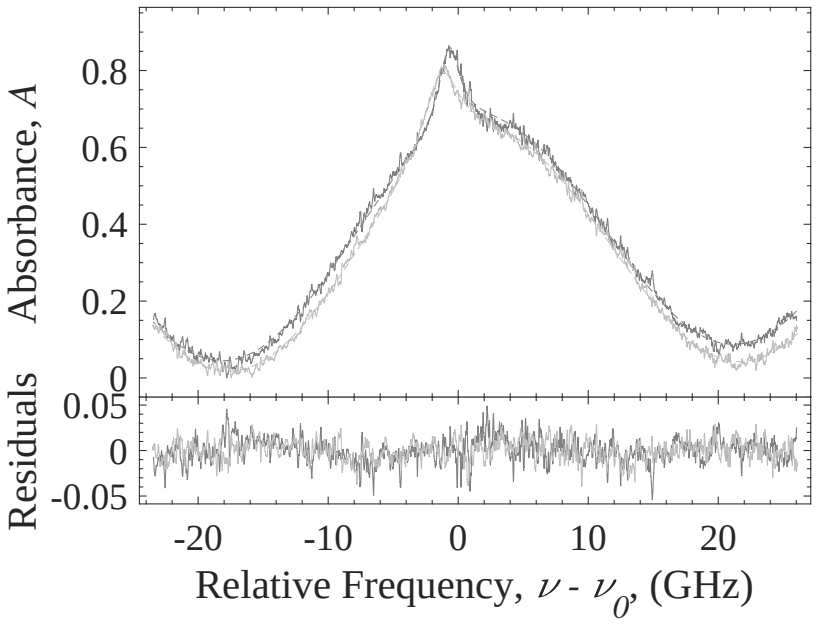

Figure 45. Absorbance data, fits, and residuals for a MHCD with a 254 μm thick dielectric and 200 μm hole diameter. The darker line is the data at 100 Torr and the lighter line is at 200 Torr. A Lorentzian and sine function with a linear baseline were fit concurrently.

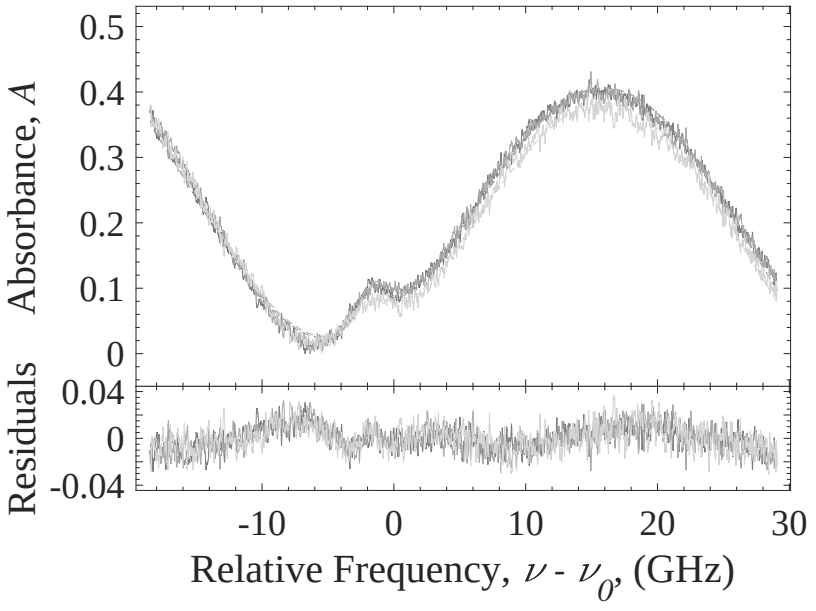

Figure 46. Absorbance data, fits, and residuals for a MHCD with a 254 μm thick dielectric and 200 μm hole diameter. The darker line is the data at 300 Torr and the lighter line is at 400 Torr. A Lorentzian and sine function with a linear baseline were fit concurrently.

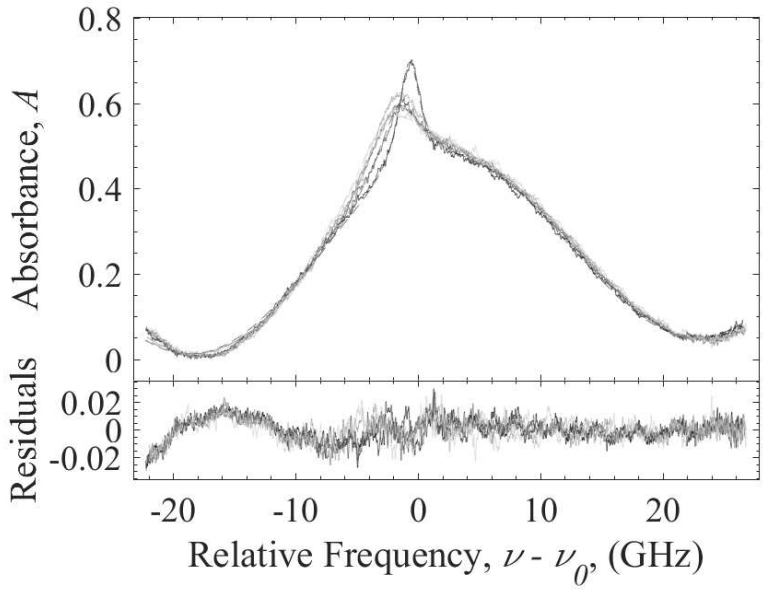

Figure 47. Absorbance data, fits, and residuals for a MHCD with a 254 μm thick dielectric and 300 μm hole diameter. The pressures ranges from 100-400 Torr in 100 Torr increments from darkest to lightest. A Lorentzian and sine function with a linear baseline were fit concurrently.

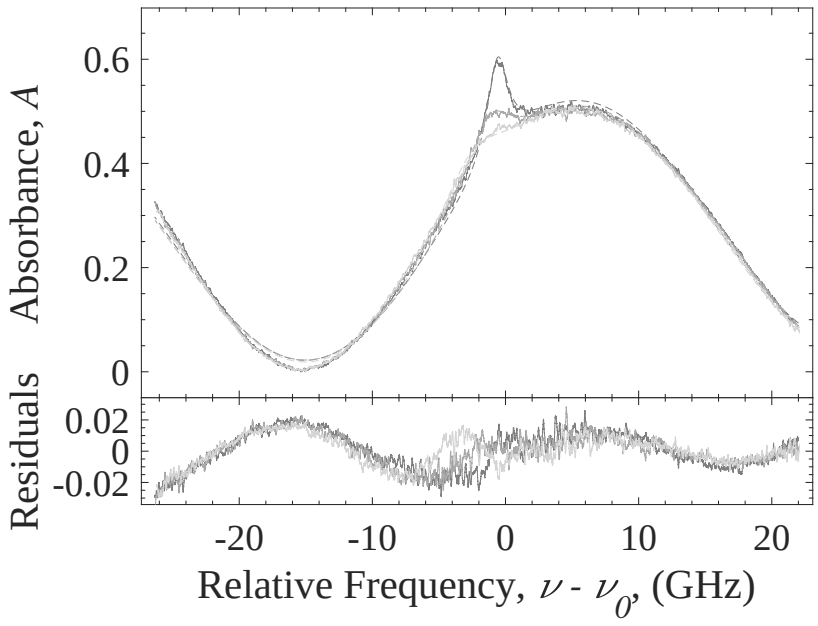

Figure 48. Absorbance data, fits, and residuals for a MHCD with a 254 μm thick dielectric and 400 μm hole diameter. The pressures ranges from 100-300 Torr in 100 Torr increments from darkest to lightest. A Lorentzian and sine function with a linear baseline were fit concurrently.

Appendix C. Florescence Images

Florescence images were taken both perpendicular to the plate and viewing the hole end on. The figures below are the images taken of all cases not already shown or discussed in section 4.5. The perpendicular images (Figures 49-54) were used to determine the maximum path lengths. The end-on images (Figures 55-57) made it clear that the plasma often not in line with the laser path, even though it might appear to be from side-on images. For each figure the images were adjusted for exposure time so the intensities can be compared.

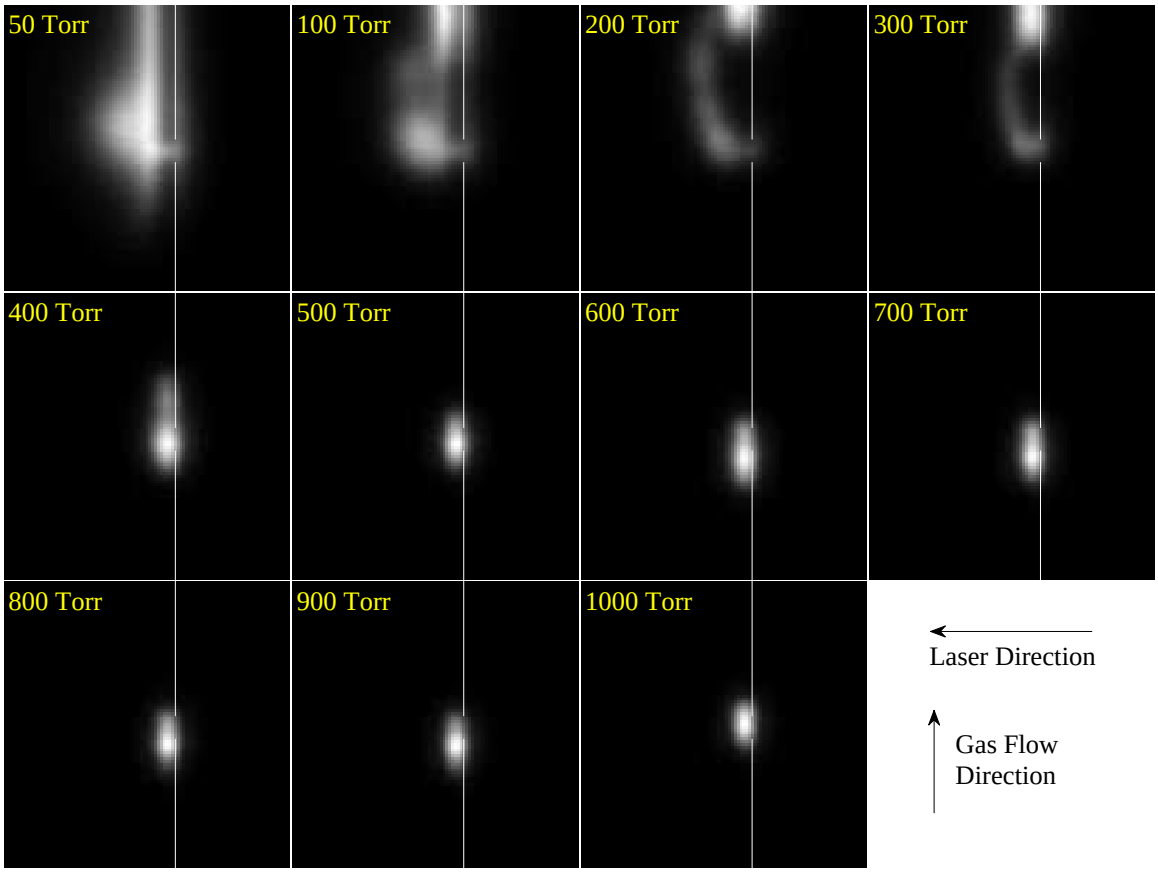

Figure 49. Side florescence from a 127 μm thick dielectric and 100 μm hole. The approximate location of the left plate edge is shown with the white line, with the gap representing the hole location. There is an asymmetry in the plasma formation even at 50 Torr, and from 100-300 Torr the main plasma formation is well above the hole.

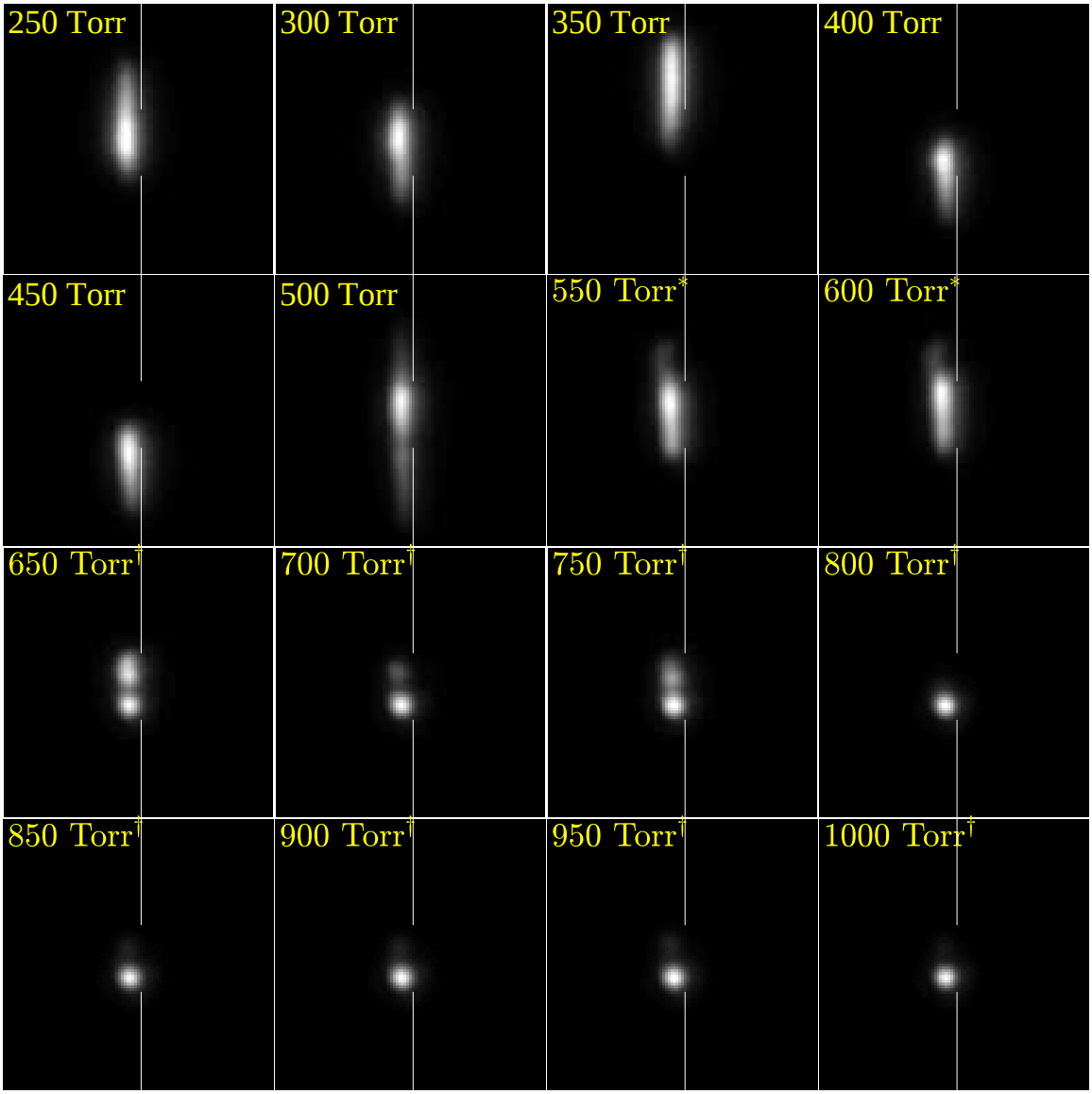

Figure 50. Side florescence from 127 μm thick dielectric and 300 μm hole diameter plates. The * (550 and 600 Torr) and † (650-1,000 Torr) indicate when different plates were used. The approximate location of the left plate edge is shown with the white line, with the gap representing the hole location. The plasma formation for each of the three plates used is slightly different. With the first plate (250-500 Torr) the plasma formation jumps up and down, the cause of which is unknown. With the second plate there is a small tail like structure on the upper side. With the third plate there are one or two smaller circular regions instead of one larger elongated region.

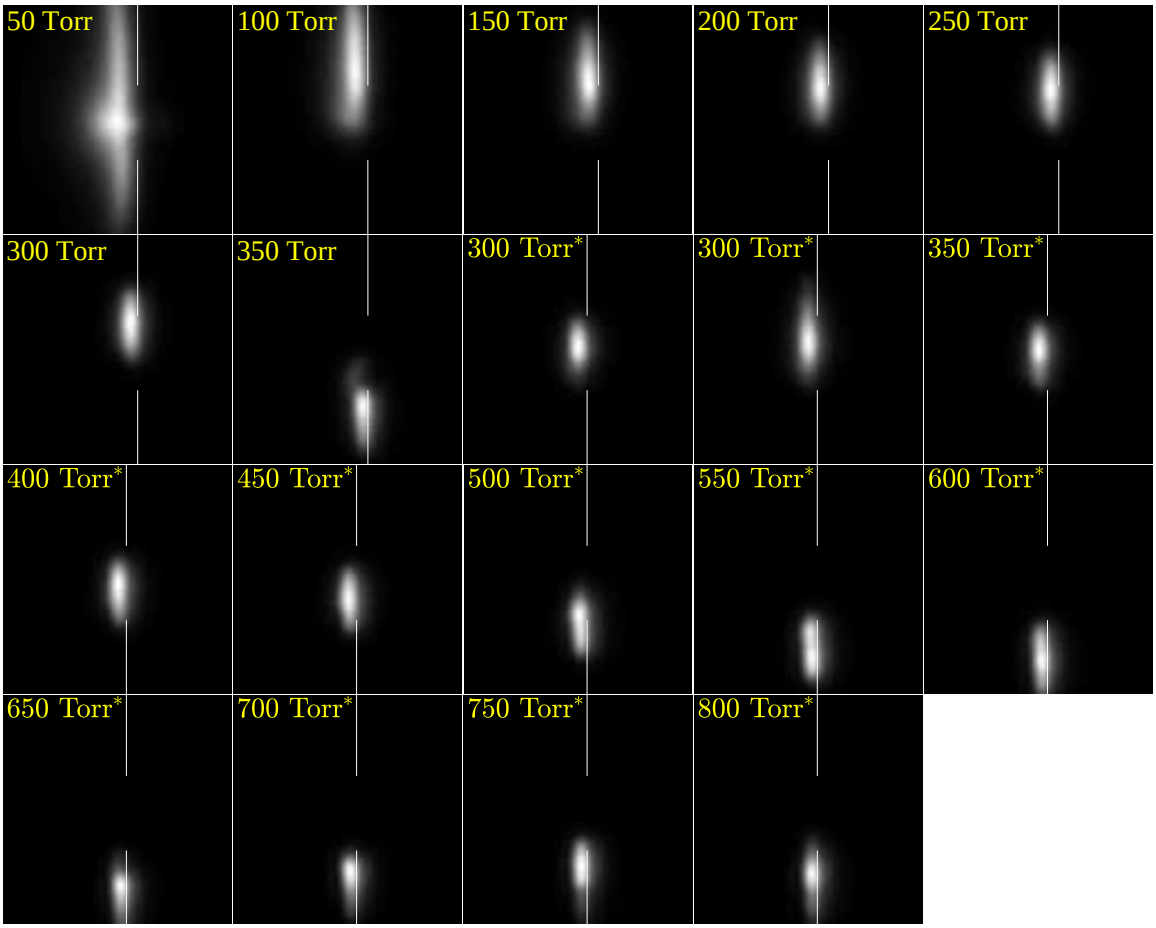

Figure 51. Side florescence from 127 μm thick dielectric and 400 μm hole plates. The * indicates when a different plate was used. The approximate location of the left plate edge is shown with the white line, with the gap representing the hole location. A symmetric plasma formation similar to the one at 50 Torr is desirable. With the first plate the plasma tended to form mostly above the hole, except for at 350 Torr where it was almost completely below it. With the second plate the plasma was initially centered on the hole and then moved below the hole. The difference in the plasma location is likely due to difference in the plate surface.

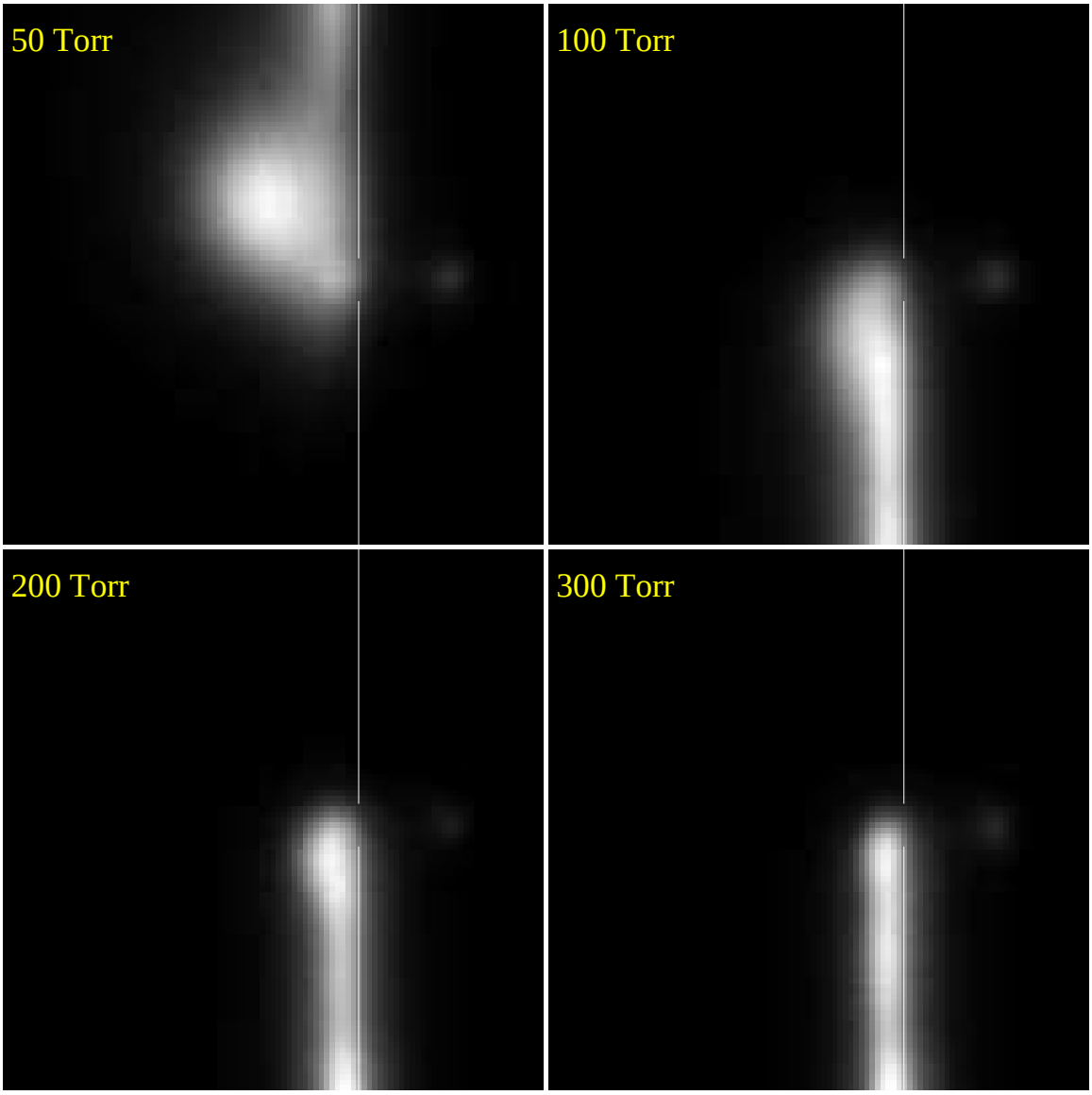

Figure 52. Side florescence from a 254 μm thick dielectric and 100 μm diameter hole. The approximate location of the left plate edge is shown with the white line, with the gap representing the hole location. There is a small circular florescence spot on the right in each image and is the florescence on the right side of the plate (the right edge of the plate is not marked). The plasma extends along the plate surface up away from the hole at 50 Torr, and down from the hole at 100-300 Torr. It is not known why there is a change in direction.

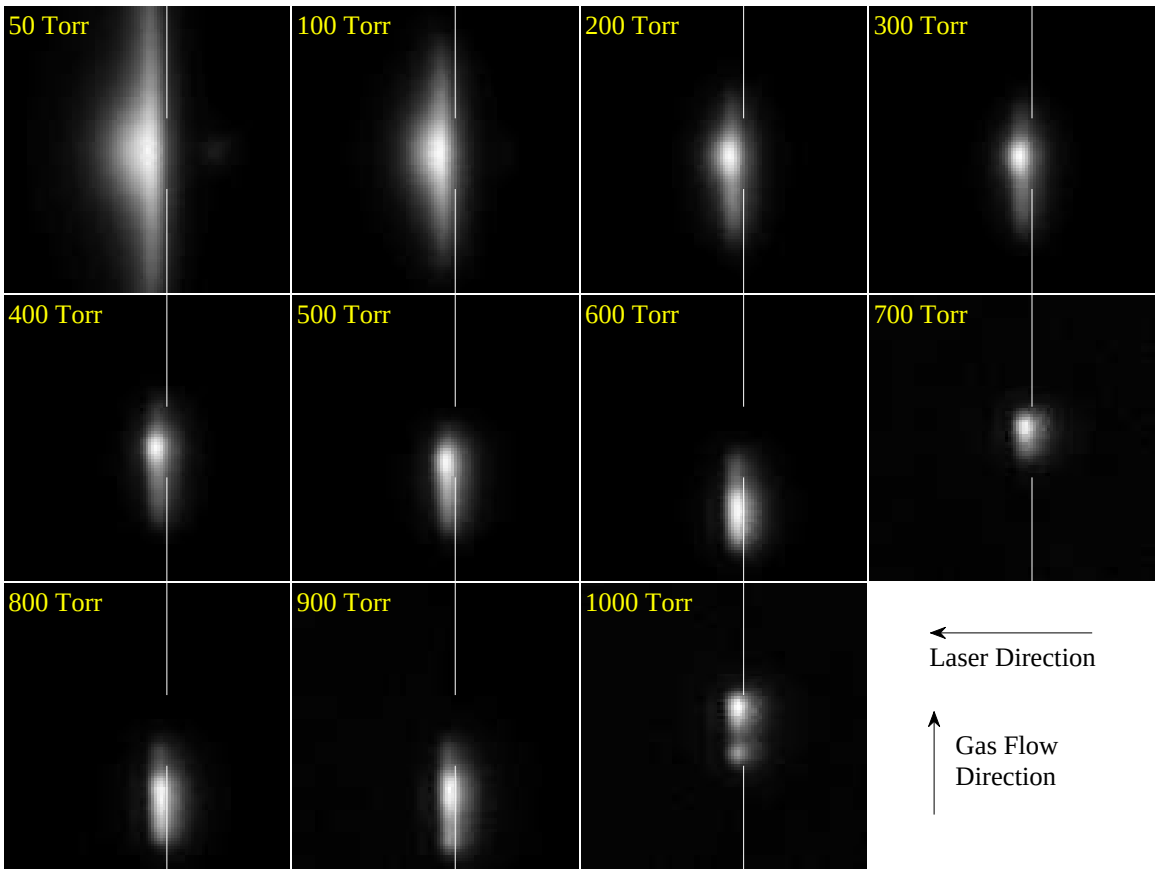

Figure 53. Side florescence from a 254 μm thick dielectric and 300 μm diameter hole. The approximate location of the left plate edge is shown with the white line, with the gap representing the hole location. At 50 and 100 Torr the plasma is symmetric and a slight bit of florescence can be seen on the opposite side of the plate (right of the white lines). At 200 Torr and above the plasma is asymmetric and forms in line with or below the hole.

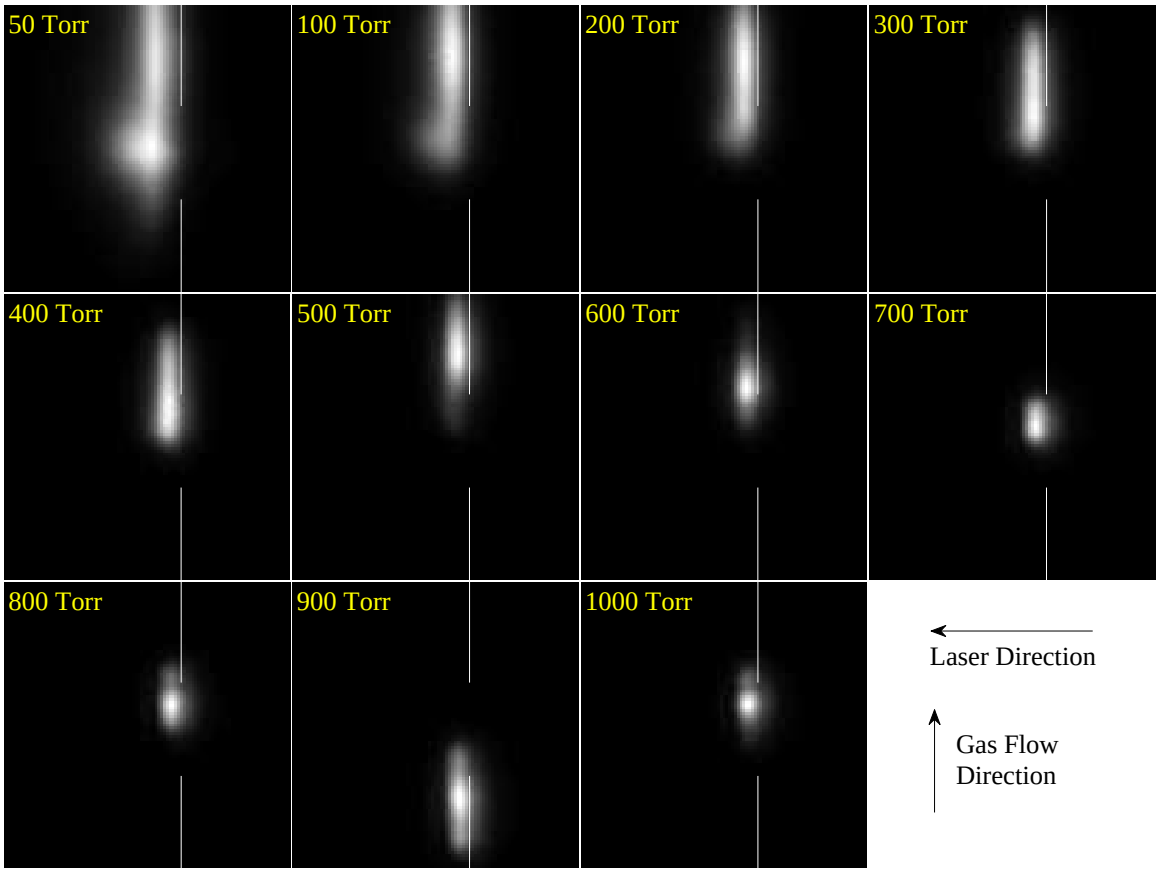

Figure 54. Side florescence from a 254 μm thick dielectric and 400 μm diameter hole. The approximate location of the left plate edge is shown with the white line, with the gap representing the hole location. The plasma formation is always asymmetric but its location varies. While it mostly forms near the upper edge of the hole and extends upward, at 500 and 900 Torr the plasma is mostly above and below the hole respectively. Excluding 900 Torr the plasma constricts to the upper hole region as the pressure increases. It is not known why the upper region of the hole was the favored location for this plate.

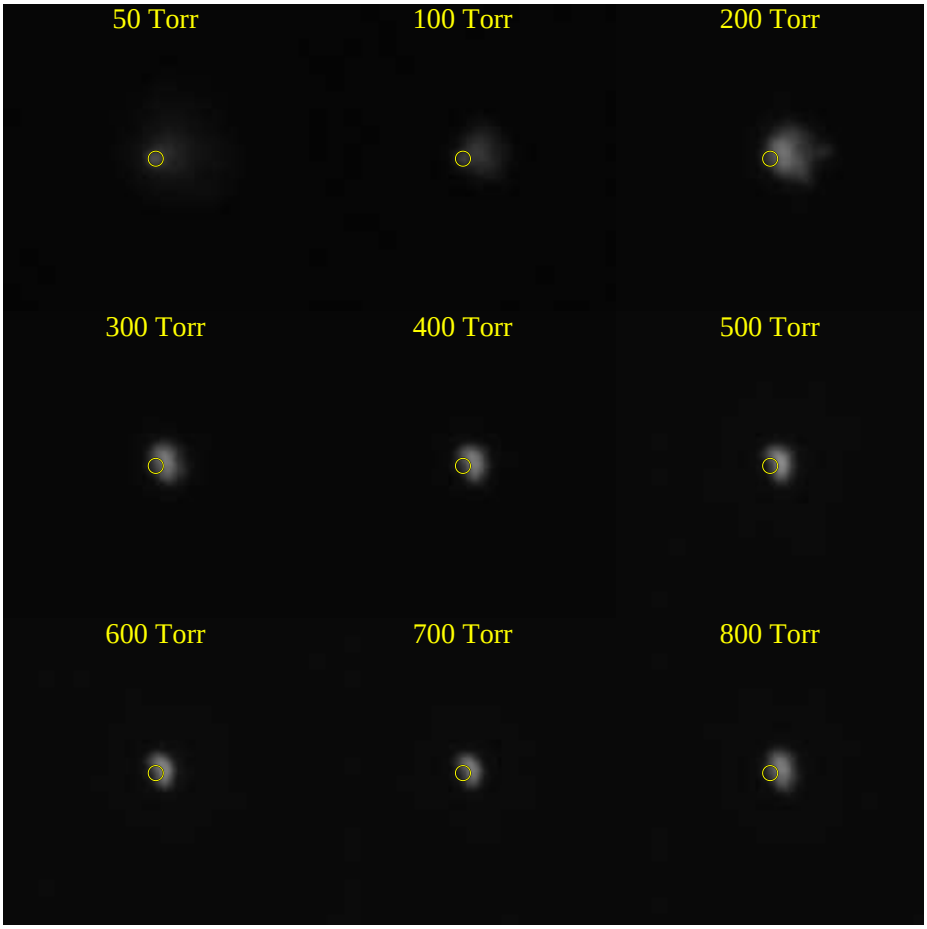

Figure 55. End-on images of a 127 μm thick dielectric, 100 μm diameter MHCD. The circle shows the approximate location of the hole. The gas flow is from the bottom to the top. At 50 Torr there is a slight asymmetry, which becomes more prominent as the pressure increases. It is unknown what caused the asymmetry, but it could be the hole structure or defects in the plate surface.

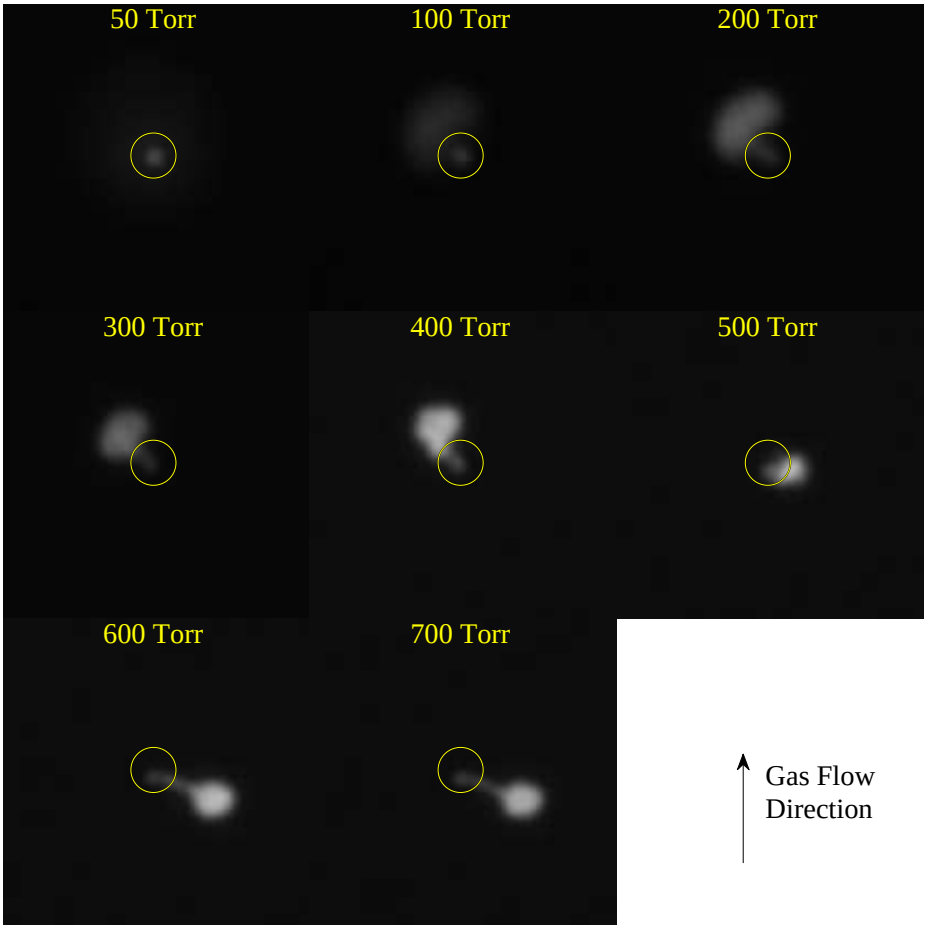

Figure 56. End-on images of a 127 μm thick dielectric, 300 μm diameter MHCD. The circle shows the approximate location of the hole. The plasma is symmetric at 50 Torr, but becomes asymmetric as pressure is increased. It is unknown what causes the location of the plasma to change, but could be a result of changes to the hole and plate during operation.

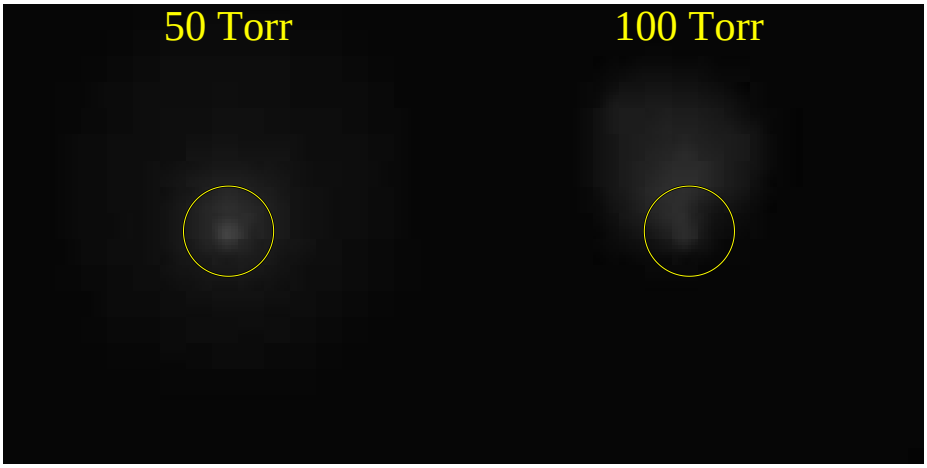

Figure 57. End-on images of a 127 μm thick dielectric, 400 μm diameter MHCD. The circle shows the approximate location of the hole. The gas flow is from the bottom to the top. The plate stopped working after 100 Torr and no other 400 μm plates were available. The plasma is symmetric at 50 Torr, but becomes antisymmetric at 100 Torr.

Appendix D. Number Densities

The number densities were measured for discharges with gaps of 127 μm and 254 μm with hole diameters from 100-400 μm at pressures of 37-400 Torr. Figure 58 shows the number densities for all discharges tested. The large uncertainty in the number densities comes from the uncertainty in the absorbance path length. The upper error bar corresponds to assuming the path length is only the width of the plate. The lower bound is the number density corresponding to the maximum path length, assuming the plasma is in line with the hole.

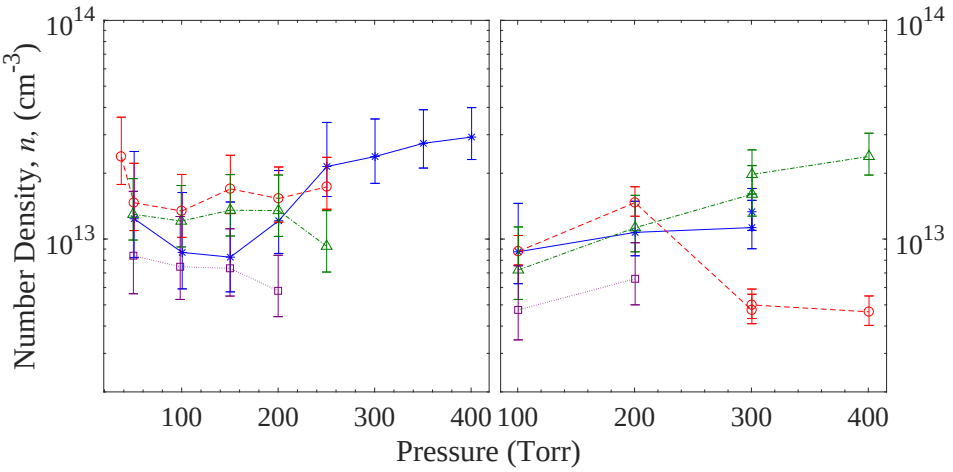

Figure 58. Number densities from MHCDs with a 127 μm thick dielectric (left) and 254 μm thick dielectric (right). Hole diameters are: 100 μm ($*$), 200 μm ($\circ$), 300 μm ($\triangle$), and 400 μm ($\square$).

Appendix E. OES Line Shape Fits

The line shape fits from the OES experiments mentioned in section 4.3, but not shown are presented here. The spectral lines were measured at four pressures ranging from 100-400 Torr. The wavelengths for the lines not shown previously, and the corresponding figure numbers are:

Figure 59 : 800.8358 nm,

Figure 60 : 801.6990 nm,

Figure 61 : 810.5920 nm,

Figure 62 : 811.7542 nm,

Figure 63 : 842.6962 nm,

Figure 64 : 912.5471 nm.

The spectral lines were fit to a Voigt profile and the data, fit and residuals are shown together. The darkest lines correspond to the lowest pressure.

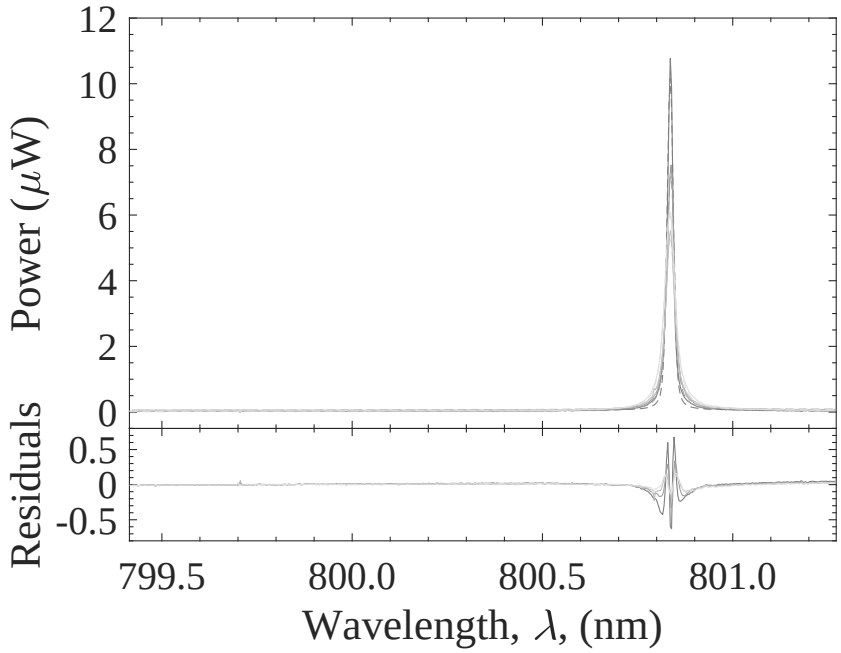

Figure 59. Argon 800.8359 nm spectral line data collected using OES. Data(–), Voigt fits(- -) and residuals are shown for pressures of 100-400 Torr from darkest to lightest.

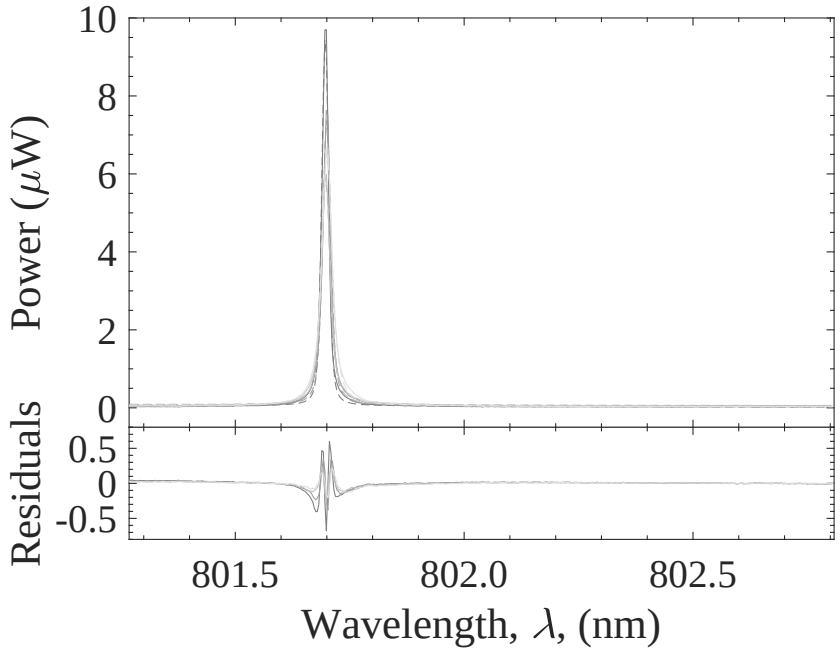

Figure 60. Argon 801.6990 nm spectral line data collected using OES. Data(–), Voigt fits(- -) and residuals are shown for pressures of 100-400 Torr from darkest to lightest.

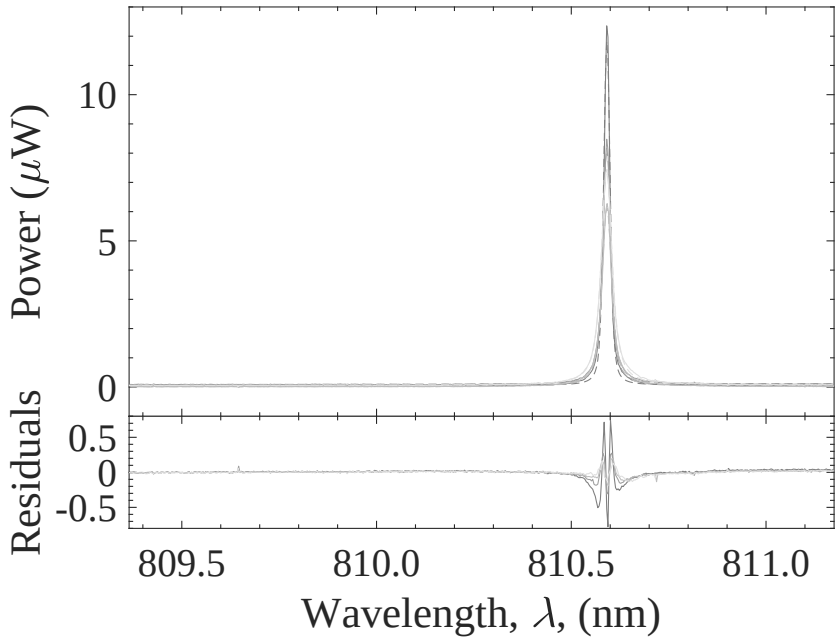

Figure 61. Argon 810.5921 nm spectral line data collected using OES. Data(–), Voigt fits(- -) and residuals are shown for pressures of 100-400 Torr from darkest to lightest.

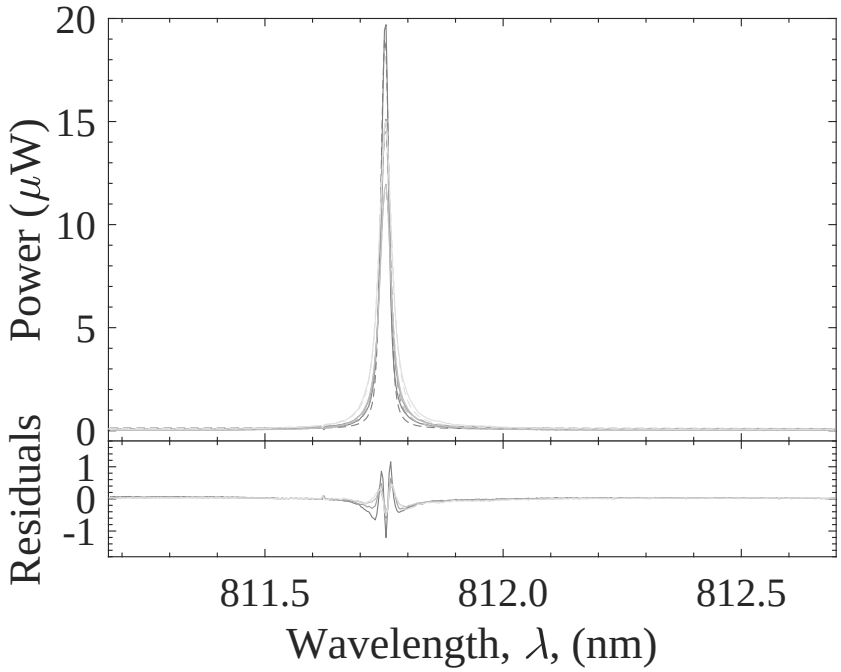

Figure 62. Argon 811.7542 nm spectral line data collected using OES. Data(–), Voigt fits(- -) and residuals are shown for pressures of 100-400 Torr from darkest to lightest.

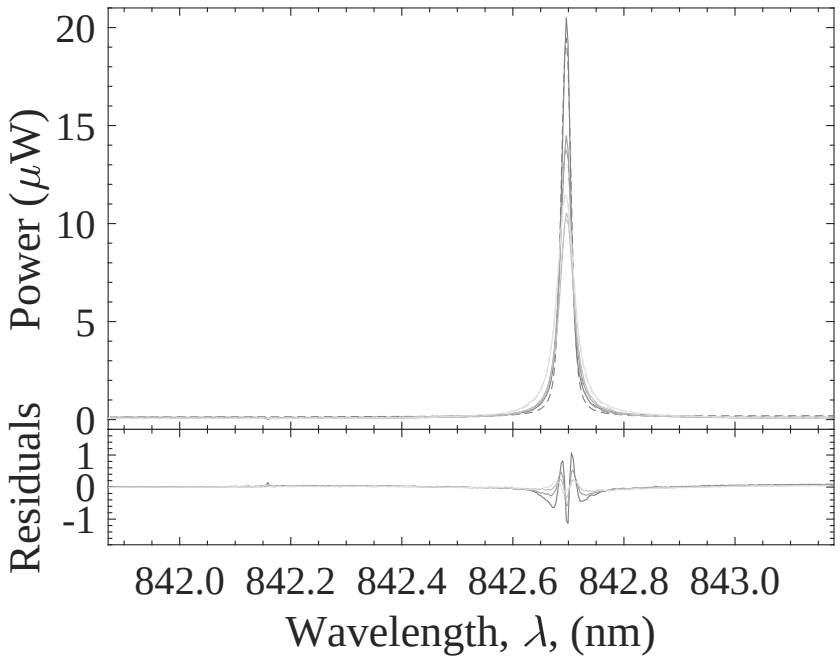

Figure 63. Argon 842.6962 nm spectral line data collected using OES. Data(–), Voigt fits(- -) and residuals are shown for pressures of 100-400 Torr from darkest to lightest.

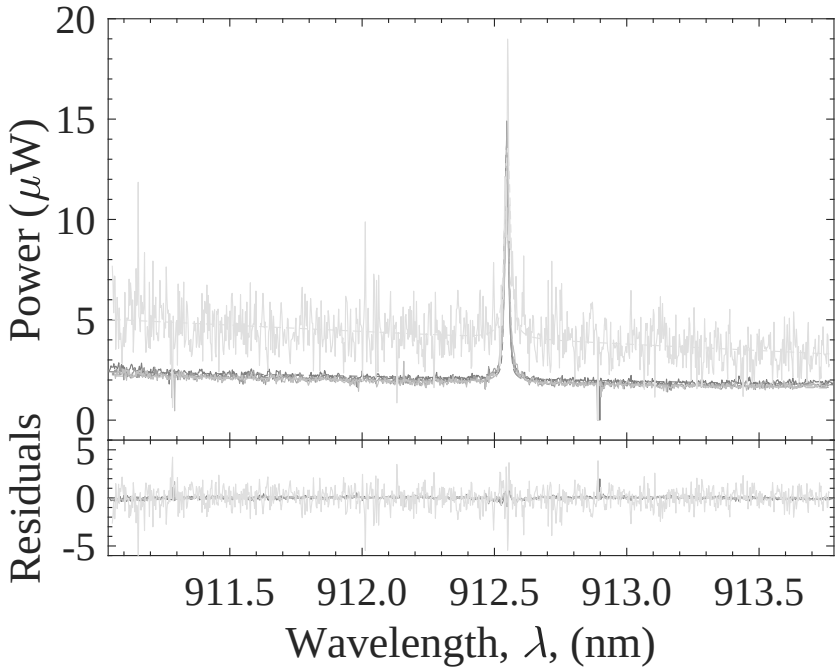

Figure 64. Argon 912.5471 nm spectral line data collected using OES. Data(–), Voigt fits(- -) and residuals are shown for pressures of 100-400 Torr from darkest to lightest.

Bibliography

1. G. Auday, Ph. Guillot, J. Galy, and H. Brunet. Experimental study of the effective secondary emission coefficient for rare gases and copper electrodes. *Journal of Applied Physics*, 83:5917, Oct 1998.

2. L. Bárdos and H. Baránková. Cold atmospheric plasma: Sources, processes, and applications. *Thin Solid Films*, 518(23):6705–6713, Sep 2010.

3. K. H. Becker, H. Kersten, J. Hopwood, and J. L. Lopez. Microplasmas: scientific challenges & technological opportunities. *The European Physical Journal D*, 60(3):437–439, Dec 2010.

4. G.H. Copley and D.M. Camm. Pressure broadening and shift of argon emission lines. *Journal of Quantitative Spectroscopy and Radiative Transfer*, 14(9):899 – 907, 1974.

5. A. V. Demyanov, I. V. Kochetov, and P. A. Mikheyev. Kinetic study of a cw optically pumped laser with metastable rare gas atoms produced in an electric discharge. *Journal of Physics D: Applied Physics*, 46(37):375202, Sep 2013.

6. D. J. Emmons and D. E. Weeks. Kinetics of high pressure argon-helium pulsed gas discharge. *Journal of Applied Physics*, 121(20):203301, 2017.

7. Ben Eshel. *Linear and non-linear spectroscopy of optically-thick argon and argon-helium plasmas in radio-frequency dielectric-barrier-discharges*. PhD thesis, Air Force Institute of Technology, 2017.

8. Ben Eshel and Glen P. Perram. Five-level argon-helium discharge model for characterization of a diode-pumped rare-gas laser. *J. Opt. Soc. Am. B*, 35(1):164–173, Jan 2018.

9. Ben Eshel, Christopher A. Rice, and Glen P. Perram. Pressure broadening and shift rates for Ar (s-p) transitions observed in an Ar-He discharge. *Journal of Quantitative Spectroscopy and Radiative Transfer*, 179:40–50, 2016.

10. R. Foest, M. Schmidt, and K. Becker. Microplasmas, an emerging field of low-temperature plasma science and technology. *International Journal of Mass Spectrometry*, 248(3):87–102, 2006.

11. J.W. Gewartowski and H.A. Watson. *Principles of electron tubes, including grid-controlled tubes, microwave tubes, and gas tubes.* Princeton, NJ: Van Nostrand, 1965. pg. 561-562.

12. G. D. Hager and G. P. Perram. A three-level analytic model for alkali metal vapor lasers: Part I. Narrowband optical pumping. *Applied Physics B: Lasers and Optics*, 101(1/2):45–56, 2010.

13. Gordon D. Hager and Glen P. Perram. A three-level model for alkali metal vapor lasers. Part II: Broadband optical pumping. *Applied Physics B: Lasers and Optics*, 112(4):507–520, 2013.

14. J. Han, M. C. Heaven, P. J. Moran, G. A. Pitz, E. M. Guild, C. R. Sanderson, and B. Hokr. Demonstration of a CW diode-pumped Ar metastable laser operating at 4 W. *Opt. Lett.*, 42(22):4627–4630, Nov 2017.

15. Jiande Han, Leonid Glebov, George Venus, and Michael C Heaven. Demonstration of a diode-pumped metastable Ar laser. *Optics Letters*, 38(24):5458–5461, Dec 2013.

16. Jiande Han and Michael C. Heaven. Gain and lasing of optically pumped metastable rare gas atoms. *Proc. of SPIE*, 8547(11):2157, 2012.

17. Jiande Han and Michael C. Heaven. Kinetics of optically pumped ar metastables. *Opt. Lett.*, 39(22):6541–6544, Nov 2014.

18. Jiande Han, Michael C. Heaven, Daniel Emmons, Glen P. Perram, David E. Weeks, and William F. Bailey. Pulsed discharge production Ar* metastables. *Proc. of SPIE*, 9729, 2016.

19. M. C. Heaven. Pulsed discharge - diode pumped Ar* laser. Presented at the Directed Energy Professioal Society 19th Annual Symposium. Feb 2017.

20. Alan R. Hoskinson, José Gregorío, Jeffrey Hopwood, Kristin Galbally-Kinney, Steven J. Davis, and Wilson T. Rawlins. Argon metastable production in argon-helium microplasmas. *Journal of Applied Physics*, 119(23):233301, Jun 2016.

21. Alan R. Hoskinson, José Gregório, Jeffrey Hopwood, Kristin L. Galbally-Kinney, Steven J. Davis, and Wilson T. Rawlins. Spatially resolved modeling and measurements of metastable argon atoms in argon-helium microplasmas. *Journal of Applied Physics*, 121(15):153302, Apr 2017.

22. A. Kramida, Yu. Ralchenko, J. Reader, and NIST ASD Team. NIST Atomic Spectra Database (ver. 5.3), [Online]. Available: `http://physics.nist.gov/asd` [2017, May 22]. National Institute of Standards and Technology, Gaithersburg, MD., 2015.

23. William F. Krupke, Raymond J. Beach, V. Keith Kanz, and Stephen A. Payne. Resonance transition 795-nm rubidium laser. *Opt. Lett.*, 28(23):2336–2338, Dec 2003.

24. R. J. Leiweke and B. N. Ganguly. Diode laser spectroscopic measurements of gas temperature in a pulsed dielectric barrier discharge using collisional broadening

and shift of $1s_3 \rightarrow 2p_2$ and $1s_5 \rightarrow 2p_7$ argon transitions. *Journal of Applied Physics*, 113:143302, 2013.

25. Pavel A. Mikheyev, Jiande Han, Amanda Clark, Carl Sanderson, and Michael C. Heaven. Production of Ar metastables in a dielectric barrier discharge. *Proc. SPIE*, 10254, 2017.

26. P. S. Moussounda and P. Ranson. Pressure broadening of argon lines emitted by a high-pressure microwave discharge (surfatron). *Journal of Physics B: Atomic and Molecular Physics*, 20(5):949, 1987.

27. J.J. Olivero and R.L. Longbothum. Empirical fits to the voigt line width: A brief review. *Journal of Quantitative Spectroscopy and Radiative Transfer*, 17(2):233 – 236, 1977.

28. C. Penache, M. Miclea, A. Bräuning-Demian, O. Hohn, S. Schössler, T. Jahnke, K. Niemax, and H. Schmidt-Böcking. Characterization of a high-pressure microdischarge using diode laser atomic absorption spectroscopy. *Plasma Sources Science and Technology*, 11(4):476–483, 2002.

29. Maria Christina Penache. *Study of high-pressure glow discharges generated by micro-structured electrode (MSE) arrays*. PhD thesis, Goethe University Frankfurt, 2002.

30. Greg A. Pitz and Monte D. Anderson. Recent advances in optically pumped alkali lasers. *Applied Physics Reviews*, 4(4):041101, 2017.

31. Greg A. Pitz, Donald M. Stalnaker, Eric M. Guild, Benjamin Q. Oliker, Paul J. Moran, Steven W. Townsend, and David A. Hostutler. Advancements in flowing diode pumped alkali lasers. *Proc. SPIE*, 9729, 2016.

32. Yu. P. Raizer. *Gas Discharge Physics*. Springer, 1997.

33. W. T. Rawlins, K. L. Galbally-Kinney, S. J. Davis, A. R. Hoskinson, and J. A. Hopwood. Laser excitation dynamics of argon metastables generated in atmospheric pressure flows by microwave frequency microplasma arrays. *Proc. SPIE*, 8962:896203–18, 2014.

34. W. T. Rawlins, K. L. Galbally-Kinney, S. J. Davis, A. R. Hoskinson, J. A. Hopwood, and M. C. Heaven. Optically pumped microplasma rare gas laser. *Optics Express*, 23(4):4804, 2015.

35. Karl H. Schoenbach and Kurt Becker. 20 years of microplasma research: a status report. *Eur. Phys. J. D*, 70(29), 2016.

36. Karl H. Schoenbach, Ahmed El-Habachi, Wenhui Shi, and Marco Ciocca. High-pressure hollow cathode discharges. *Plasma Sources Science and Technology*, 6(4):468–477, 1997.

37. Jong W. Shon and Mark J. Kushner. Excitation mechanisms and gain modeling of the highpressure atomic Ar laser in He/Ar mixtures. *Journal of Applied Physics*, 75(4):1883–1890, Feb 1994.

38. Robert H. Stark and Karl H. Schoenbach. Direct current high-pressure glow discharges. *Journal of Applied Physics*, 85(4):2075–2080, Feb 1999.

39. Claire Tendero, Christelle Tixier, Pascal Tristant, Jean Desmaison, and Philippe Leprince. Atmospheric pressure plasmas: A review. *Spectrochimica Acta Part B: Atomic Spectroscopy*, 61(1):2–30, Jan 2006.

40. O. Vallee, P. Ranson, and J. Chapelle. Measurements of broadening of argon lines and oscillator strengths of resonance lines. *Journal of Quantitative Spectroscopy and Radiative Transfer*, 18(3):327 – 336, 1977.

41. Joseph T. Verdeyen. *Laser Electronics*. Prentice Hall, 3rd edition, 1995.

42. Zining Yang, Guangqi Yu, Hongyan Wang, Qisheng Lu, and Xiaojun Xu. Modeling of diode pumped metastable rare gas lasers. *Opt. Express*, 23(11):13823–13832, Jun 2015.

43. Xi-Ming Zhu and Yi-Kang Pu. A simple collisional radiative model for low-temperature argon discharges with pressure ranging from 1Pa to atmospheric pressure: kinetics of Paschen 1s and 2p levels. *Journal of Physics D: Applied Physics*, 43(1):015204, Jan 2010.

REPORT DOCUMENTATION PAGE

Form Approved
OMB No. 0704–0188

1. REPORT DATE *(DD–MM–YYYY)*	2. REPORT TYPE	3. DATES COVERED *(From — To)*
22-03-2018	Master's Thesis	Sept 2016 — Mar 2018

4. TITLE AND SUBTITLE

Excited Argon $1s_5$ Production in Microhollow Cathode Discharges

5a. CONTRACT NUMBER

5b. GRANT NUMBER

5c. PROGRAM ELEMENT NUMBER

6. AUTHOR(S)

Peterson, Richard D, 2d Lt

5d. PROJECT NUMBER

5e. TASK NUMBER

5f. WORK UNIT NUMBER

7. PERFORMING ORGANIZATION NAME(S) AND ADDRESS(ES)

Air Force Institute of Technology
Graduate School of Engineering and Management (AFIT/EN)
2950 Hobson Way
WPAFB OH 45433-7765

8. PERFORMING ORGANIZATION REPORT NUMBER

AFIT-ENP-MS-18-M-095

9. SPONSORING / MONITORING AGENCY NAME(S) AND ADDRESS(ES)

Harro Ackerman
High-Energy Laser Joint Technology Office
801 University Blvd Se, Ste 209
Albuquerque, NM 87106
505-248-8208
Harro.Ackerman@jto.hpc.mil

10. SPONSOR/MONITOR'S ACRONYM(S)

HEL JTO

11. SPONSOR/MONITOR'S REPORT NUMBER(S)

12. DISTRIBUTION / AVAILABILITY STATEMENT

Distribution Statement A:
Approved for Public Release; Distribution unlimited.

13. SUPPLEMENTARY NOTES

14. ABSTRACT

Diode-pumped rare gas lasers (DPRGL) have been in development for their potential to become high energy lasers with excellent beam quality that is typical of gas lasers. DPRGL require metastable densities on the order of 10^{13} cm^{-3} at pressures around one atmosphere for efficient operation. Argon $1s_5$ number densities have been measured in microhollow cathode discharges (MHCD) using tunable diode laser absorption spectroscopy. The MHCDs had gaps of 127 and 254 μm and hole diameters from 100-400 μm. Absorbance was measured at pressures of 37 Torr up to 400 Torr, where absorbance could no longer be detected. Fluorescence images revealed the plasma formation was inconsistent and often not in line with the hole, making path length determinations difficult. Assuming a path length equal to the total plate thickness of either 198 or 325 μm resulted in the maximum possible Ar 1s5 number densities, ranging from 0.55-4.0 $\times$ 10^{13} cm^{-3}. The actual number densities could be three times lower depending on the actual path length. There were no consistent trends with hole diameter, gas pressure, or gap distance.

15. SUBJECT TERMS

Rare gas laser, microhollow cathode discharge, metastable argon density, micro-discharge, argon plasma, laser absorption spectroscopy

16. SECURITY CLASSIFICATION OF:			17. LIMITATION OF ABSTRACT	18. NUMBER OF PAGES	19a. NAME OF RESPONSIBLE PERSON
a. REPORT	b. ABSTRACT	c. THIS PAGE			Dr. Glen P. Perram, AFIT/ENP
U	U	U	UU	104	19b. TELEPHONE NUMBER *(include area code)* (937)255-3636 x4504 glen.perram@afit.edu